CONDUCTIVITY BASED PHOTOTHERMAL ABSORBANCE DETECTION FOR MICROFLUIDIC DEVICES

Erin Rebecca Ferguson Welch

A dissertation submitted to the faculty of the University of North Carolina at Chapel Hill in partial fulfillment of the requirements for the degree of Doctor of Philosophy in the Department of Chemistry.

Chapel Hill
2009

Approved By:

Professor James W. Jorgenson

Professor J. Michael Ramsey

Professor Mark H. Schoenfisch

Professor Gary J. Pielak

Professor Linda L. Spremulli

ABSTRACT

Erin Rebecca Ferguson Welch

CONDUCTIVITY BASED PHOTOTHERMAL ABSORBANCE DETECTION FOR MICROFLUIDIC DEVICES
(Under the direction of James W. Jorgenson)

The research presented describes the development of microfluidic devices for conductivity detection and its application for high-sensitivity photothermal detection. The process of photothermal absorbance detection combines the universality of standard absorption detection with the path length-independence of conductivity detection. Due to limitations in fabricating capillary-based contactless conductivity detectors, the laser excitation region is extremely small in comparison to total sensing region, which reduces the detected signal. This problem can be circumvented by applying the technique to a microfabricated system.

A microfabricated contact conductivity detector using metal film electrodes was incorporated into a device with a simple cross channel. Several inorganic salts were detected with varying excitation voltages, frequencies, and electrode geometries. Using the data from these conductivity studies, the device was modified to include a three-electrode design for use in photothermal detection. Two types of electrodes were investigated, metal thin film electrodes and polyelectrolyte salt bridge electrodes (PSBE). Studies were performed in order to characterize both types of electrodes. Conditions investigated include alteration of fabrication and bonding techniques, electrode and channel dimensions, laser settings, and

conductivity excitation parameters. Initial studies were carried out using DABSYL-tagged analytes excited by 488 nm laser light. Successful separation and detection of several DABSYL-tagged amino acids was achieved.

One advantage of conventional optical absorbance detection techniques is the ability to detect native analytes, but the visible wavelength used in the previous studies restricted analytes to those that could be tagged with DABSYL chloride. In order to study the photothermal response of several native biological analytes, further characterization of the device's behavior was performed using 266 nm laser excitation. A number of analytes including fluorescent dyes, native amino acids and peptides, and nucleotide bases and oligonucleotides were detected with the system. Measurements indicated comparable behavior to that observed in the visible spectrum with respect to both signal and noise responses. A similar detection device was fabricated for use with high performance liquid chromatography (HPLC). Conductivity based photothermal detection was tested with both an end-column detector and an integrated packed bed/conductivity detector device.

To Chris
for his love and support,
and to my Parents and Sisters
for all they have done for me

ACKNOWLEDGEMENTS

I cannot completely express my gratitude to all of those who have helped me along the path to reaching where I am today. First and foremost, I thank Chris, my love, my best friend, my husband. After five years of friendship, four years of courtship, and only a few short weeks of marriage, he has come to mean more to me than I could ever have imagined. Starting from undergraduate calculus class at Clemson, we have always helped and supported each other in all aspects of our lives. He has been an indefinable help during the preparation of this dissertation, and I would not have made it through without him.

To start at the beginning, I thank my family, my parents, Michael and Kathleen Ferguson, and my sisters, Meghan and Kaitlin. My parents have provided me with all of the love and support that I could possibly imagine growing up, and continue to do so now. They provided me with a strong foundation in my faith and my approach to life and achievement. I would have not made it to this point in my life without them. My sisters have taught me so much in that, despite our differences, we have always stood by each other.

I must thank Dr. James Jorgenson and Dr. Mike Ramsey for their intellectual support over the last several years. With their aid, I have developed far beyond the timid first year graduate student I once was. I'd also like to thank both the Jorgenson and Ramsey research groups for their help along the way and for all of our interesting discussions, both research-related and not. I especially thank Patty Dennis for her help in the beginning stages of the development of this project and her input along the way. I would also like to thank the staff

and faculty of the Clemson Chemistry Department, especially my undergraduate advisor, Dr. Shiou-Jyh Hwu. From the beginning as a high school summer research student and throughout my undergraduate career, Dr. Hwu and others in the department took me under wing and encouraged me as a scientist.

I would like to thank all of my friends that have loved and supported me over the last several years. My church family and especially my Small Group family have continually offered their support and prayers through the last several stressful months. They have been such an encouragement in a trying time. I'd also like to thank the community from Karate International of Durham, especially all the black belt ladies for their friendship and support.

Finally, I thank the One without whom I would not be at all, my Lord and Savior, my Friend and Comforter, the only One who truly gives me strength to make it through the day, thank You.

TABLE OF CONTENTS

LIST OF TABLES

LIST OF FIGURES

LIST OF ABBREVIATIONS

Abbreviation	Definition
°C	degree Celsius
A	ampere
AC	alternating current
BSA	bovine serum albumin
C_4D	capacitively coupled contactless conductivity detection
C18	octadecylsilane
CE	capillary electrophoresis
CEC	capillary electrochromatography
CITP	capillary isotachophoresis
cm	centimeter
Cr, chrome	chromium
CZE	capillary zone electrophoresis
d	depth
DABSYL	(dimethylamino) azobenzenesulfonyl
DAQ	data acquisition
dB	decibel
DC	direct current
EK	electrokinetic
EOF	electroosmotic flow
EOP	electroosmotic pumping
g	gram

Gly	glycine
h	height
H_2SO_4	sulfuric acid
HCl	hydrochloric acid
His	Histidine
HPLC	high performance liquid chromatography
hr	hour
Hz	Hertz
i.d.	inner diameter
in	inch
ITP	isotachophoresis
K	Kelvin
KCl	potassium chloride
kHz	kiloHertz
kV	kilovolt
kΩ	kiloohm
l	length
LC	liquid chromatography
Leu-Enk	leucine enkephalin
LiCl	lithium chloride
LIF	laser induced fluorescence
M	molar
MES	2-morpholinoethansulfonic acid

MHz	megahertz
m	meter
min	minute
mL	milliliter
mm	millimeter
MS	mass spectroscopy
ms	millisecond
mV	millivolt
mV_{pp}	peak-to-peak millivolt
mW	milliWatt
MΩ	megaohm
nA	nanoamp
NaCl	sodium chloride
NaOH	sodium hydroxide
nL	nanoliter
nM	nonomolar
nm	nanometer
nV	nanovolt
o.d.	outer diameter
OPA	operational amplifier
PCB	printed circuit board
PDMS	poly-dimethylsiloxane
PEEK	polyetheretherketone

pF	picoFarad
pg	picogram
pL	picoliter
PMMA	poly-methyl methacrylate
pmol	picomole
ppb	parts per billion
PPM	porous polymer monoliths
ppm	parts per million
Pro	proline
PSBE	polyelectrolyte salt bridge electrode
psi	pounds per square inch
Pt	platinum
RP	reverse phase
rpm	revolutions per minute
RSD	relative standard deviations
s	second
S/N	signal to noise ratio
Ti	titanium
TLS	thermal lens spectroscopy
Trp	tryptophan
UV	ultraviolet
V	Volts
V_{pp}	peak-to-peak voltage

V_{rms}	root-mean-square voltage
vis	visible
W	watt
w	width
µg	microgram
µL	microliter
µM	micromolar
µm	micrometer
µTAS	micro-total analysis system
µV	microvolt

LIST OF SYMBOLS

Symbol	Definition
°	degree
A	absorbance
A	eddy diffusion term (van Deemter equation)
B	longitudinal diffusion term (van Deemter equation)
b	path length
C	capacitance
C	resistance to mass transfer term(van Deemter equation)
c	concentration
D	diffusion coefficient
e	fundamental charge of an electron
F	Faraday's constant
f	frequency
H	height equivalent of a theoretical plate
L	length of a separation column
M	molarity
N	number of theoretical plates
r	radius
T	transmittance
V	Volts
z	ion charge
Å	Angstrom

ε	molar absorptivity
κ	electrical conductivity
λ	wavelength
μ	ion mobility
η	viscosity
π	pi
σ_L^2	spatial variance

Chapter 1: Detection Methods in Microfluidic Systems

1.1 Microfluidic Systems

The history of the development of analytical-scale separation techniques involves a general movement to the use of ever smaller systems. This trend has produced a number of advantages for the analysis of complex mixtures. Electrophoresis or chromatographic techniques that incorporate small volume components have the advantage of decreased reagent consumption and can be used to complete analyses in a very short amount of time. The advent of micro total analysis systems (μTAS) has further decreased necessary sample volumes and reduced analysis times to mere seconds. Such devices can also be mass produced, increasing reproducibility from one analysis to another. By integrating these microfluidic devices, numerous procedures can be performed on a single microchip, completing diagnostics or analyses in a fraction of the time required by conventional methods.[1-5]

The first example of a microfabricated system was credited to Terry, Jerman, and Angell in 1979.[6] The device was a miniature gas chromatographic air analyzer which they fabricated on a silicon wafer. Using photolithographic techniques and chemical etching, a 1.5 m long channel was etched into the wafer. The device incorporated a sample injection system and a thermal conductivity detector and was bonded to a Pyrex coverplate to enclose the system. The channels were then coated with a standard OV-101 liquid stationary phase, and the device was used to separate a mixture of gaseous hydrocarbons. Although the device was found to be useful and easily operated, its success was hampered by poor resolving

power in comparison to conventional capillary gas chromatography systems. The limitations in the photolithographic procedures of the time prevented generation of narrower channels. Reducing the channel depth was found to somewhat increase the separation resolution, but the resulting sharp corners and curves caused uneven coating of the stationary phase. The non-homogeneous stationary phase led to poor column performance, but the simplicity and elegance of the system opened the door for the development of μTAS devices.

Since that initial device, significant research efforts have been put into the development of microfluidic devices for use with many analytical techniques. In 1990, Manz et al.[7] introduced a device used to perform open-tubular liquid chromatography. Also fabricated from a silicon wafer, the device was simulated to have a separation efficiency of 8000 theoretical plates with a 1 minute run time or 25,000 plates with a 5 minute run time. Two years later, the same group introduced a glass device that used electrophoresis to separate analytes.[8] With an applied electric field of 5 kV, a maximum separation efficiency of 35,000 theoretical plates was achieved. Characterization of the device indicated that reducing the channel cross section in relation to the overall length could greatly improve the separation performance and time. The channels in this device were relatively small for the time, at 10 μm deep and 30 μm wide.

Electrokinetic flow has since become the most common fluid driving force used in microfluidic devices.[9] Electrophoresis has a number of advantages over liquid chromatographic techniques. For such systems, it has been shown that the separation efficiency, or the number of theoretical plates (N), is proportional to the running voltage (V) and the species mobility (μ) and inversely related to the diffusion coefficient of the analyte (D) according to the equation:

$$N = \frac{\mu V}{2D} \tag{1-1}$$

Therefore, more efficient separations can be achieved by increasing the driving voltage and subsequently decreasing the separation time and the time for the analyte to diffuse from the band.[10] However, the speed at which a separation can be performed is limited by Joule heating and how fast the generated heat can be dissipated. Small dimension systems like those in microfluidic devices, which often involve channel depths of a few tens of microns, allow very rapid dissipation of heat and, therefore, can be run at very high electric fields.

1.2 Challenges of Detection in Microcolumn and Microfluidic Devices

Unfortunately, as the systems decrease in size, so also does the maximum amount of analyte that can be injected into them before overloading becomes an issue. Therefore, in order to obtain accurate measurements of such small samples, more sensitive detection schemes are required. A variety of detection schemes have been incorporated into microfluidic systems, including various forms of optical absorbance detection, amperometric detection, and fluorescence detection.[11-23]

Currently, laser induced fluorescence (LIF) is among the most common methods of detection due to its high sensitivity and relatively simple application. LIF has been used to reach detection limits on the order of a single molecule.[24] To induce fluorescence for detection, light of a specific wavelength is applied to the detection region. As an analyte passes into this region, it absorbs the incident light and can relax back to its ground state in a number of ways. The most common means of relaxation is through vibration, producing heat. In relatively rare cases, relaxation can occur through the emission of a photon of a longer wavelength than the original light, or fluorescence. By measuring the light emitted

out of plane with the incident light, low background, highly sensitive measurements can be taken. Unfortunately, to achieve such detection limits, the analyte must provide a very high quantum yield of fluorescence.[10] There are examples of natively fluorescing analytes,[14,18,19,25] but most require the addition of a fluorescent tag. Fluorescent tagging can be a tedious process, and often the tags are as large as or larger than the analyte of interest, drastically altering the tagged analyte's behavior and further limiting the applicability of this detection method.

Electrochemical techniques are also often used for highly sensitive detection, sometimes detecting as low as nanomolar amounts.[16] Amperometric detection can be performed by applying a potential to an electrode and oxidizing or reducing the analyte at the electrode surface while measuring the current. Unfortunately, this method is also highly selective, as only analytes that are redox active within the applied potential range can be detected.[10]

Although fluorescence and electrochemical techniques are useful and sensitive, optical (UV/Vis) absorbance detection, which is more common in larger volume systems, is still of great interest in microfluidic detection devices due to its wide range of applicability. This method relies on comparison of the light incident on the detection region and the amount of light transmitted through it, and is described by Beer's Law:

$$A = -\log T = \varepsilon bc \tag{1-2}$$

where the absorbance (A) and transmittance (T) are related to the molar absorptivity of the analyte (ε), the optical path length (b), and the concentration of the analyte (c). Absorbance detection can be used to detect a much broader range of analytes, but the small volume of microcolumn and microfabricated devices presents an obstacle for this technique due to its

path length dependence. There have been a number of techniques introduced to increase the path length for detection, including z-shaped detection cells,[26-28] bubble cells, [29,30] multireflection cells,[31-34] and waveguides.[35-37] However, such structures increase the spatial extent over which detection occurs, thus decreasing the spatial resolution of the detector, and decreasing the resolution achieved in the separation. An optical technique that can overcome many of the problems inherent in fluorescence and absorbance detection would be a great advantage for microcolumn and microfluidic devices. One promising possibility is photothermal absorbance detection.[17,38-47]

1.3 Photothermal Absorbance Detection

1.3.1 Thermal Lens Spectroscopy

Photothermal absorbance detection, or thermooptical spectroscopy, depends on the indirect measurement of the absorbance by observing a change in some inherent physical property of the solution, resulting from the temperature increase caused by the absorption of light. Beginning in the late 1970's, thermal lens spectrometry (TLS) was introduced and developed as an early photothermal detection scheme.[38] Photothermal detection begins with the same principle as fluorescence detection: absorbance by an analyte of incident light and its subsequent relaxation to the ground state. Unlike fluorescence, photothermal detection relies on the more common form of vibrational relaxation. As the molecules relax to the ground state, the released energy is emitted in the form of heat, with the amount of heat produced depending on the amount of incident light, the concentration of absorbing analyte, and the absorptivity of the molecule. Specifically, TLS measures the change in temperature of the solution by monitoring the refractive index of analyte solutions.[48] As the temperature of any liquid changes, minute changes in the solvent's optical properties, specifically the

change in refractive index can be observed. There have been a number of recent attempts to incorporate this detection method into microfluidic devices.[17,39-43] Most of these examples focus on the production of microfabricated lenses and fiber optics integrated into a microfluidic system.

1.3.2 Conductivity-Based Photothermal Detection

The use of conductivity detection has been proposed as an alternative to refractive index measurements to observe the temperature changes that are central to photothermal absorbance detection.[44-47] The heat released through vibrational relaxation after the absorbance of incident light by an analyte creates a decrease in the viscosity of the solution. Reduced viscosity (η) allows for greater ion mobility (μ) according to the equation:

$$\mu = \frac{ez}{6\pi\eta r} \tag{1-3}$$

where e is the fundamental charge of an electron, z is the charge of the ion, and r is the ionic radius. As ion mobility increases, so also does the conductivity (κ) of the solution:

$$\kappa = zFc\mu \tag{1-4}$$

where F is Faraday's constant and c is the ion concentration. The change in conductivity can be monitored through conductivity detection. Conductivity-based photothermal detection measures changes in the conductivity of the solution using conductivity detection as the indirect detection method. As light is absorbed by a molecule, the heat produced from this absorption changes the viscosity of the solution and therefore the ionic conductivity of the solution.[45,46] Conductivity detection can thus form the basis for detecting the heat produced in the photothermal absorbance process.

1.3.2.1 Conductivity Detection

As a stand-alone detection method, conductivity detection, like absorbance detection, is a nearly universal technique. By measuring the resistance of a solution between two electrodes, any change in the background ion concentration results in an alteration of the conductivity signal. Therefore, any analyte that induces a change in the background conductivity can be detected. The first instances of conductivity detection were used with capillary isotachophoresis (CITP) in the 1970s by Everaerts et al.[49] To create this detector, a 50 μm thick sheet of Terylene polymer film with a 100 μm thick layer of metal foil on either side was pressed between two pieces of Kel-F plastic and placed into a brass capillary holder. The center of the Terylene/Kel-F sandwich was drilled out to match the inner diameter (i.d.) of the capillary to be used for CITP. The result was two ring electrodes formed by the metal foil through which the solution would flow. The Terylene film between the electrodes served as an insulating layer and defined the size of the detection region. During the initial testing, both alternating current (AC) and direct current (DC) were applied to the sensing electrodes. While the AC mode was mostly effective under the CITP conditions, the DC mode was found to have a number of problems. Polarization of the electrode surface prevented isolation of the zone boundaries, and the potentials used for running CITP interacted with the electrodes causing gas formation from electrolysis, resulting in high background noise. Electrolysis was minimized when using AC mode, but did occasionally occur. Over time, it was also found that direct contact with the analyte solutions could cause fouling of the electrodes

In order to prevent the difficulties caused by interactions of the conductivity detectors with the voltages used to run CITP, Gas et al.[50] introduced contactless conductivity detection. The detector electrodes consisted of four 200 μm copper enameled wires arranged in an equiplanar formation around the capillary. High frequency AC signals set 180° out of phase

were applied to two of the four electrodes. The signal, through capacitive coupling, passed through the capillary wall to the analyte solution. After the signal capacitively coupled again through the capillary wall, it was detected using the remaining two electrodes. Signal from the two electrodes was amplified using a differential amplifier circuit and was then filtered. The resulting detector was more stable than the contact conductivity detector. However, the capacitive nature of the detector increased the effective sensing region, reducing the detectors' spatial resolution when compared to the contact method.

Conductivity detection was first introduced for use with capillary zone electrophoresis (CZE or CE) in the late 1980s by Huang, et al.[51-53] In this case, two 40 μm holes were laser-drilled into the capillary wall directly across from each other. Two 25 μm diameter platinum wires were placed into the holes and held in place with epoxy. The detector was very fragile, so the detection system was encased within a Plexiglas frame for added support. The resulting electrodes directly contacted the solution, but the narrow wires and their arrangement reduced the voltage dropped across the metal surface, thus reducing electrolysis seen in previous systems. The system was reported to be effective for detecting small inorganic ions such as Li^+ and was found to have good linearity over several orders of magnitude. Despite the favorable response, the detector was difficult to produce and implement, and once completed, the capillary was very fragile and easily broken.

Contactless conductivity detection was independently developed for use with capillary electrophoresis by two groups in 1998. Zemann et al.[23] fabricated their detection electrodes of metal electrodes painted on the surface of a capillary or from 15 mm to 50 mm long syringe cannulae, producing cylindrical electrodes through which the capillary could be inserted. One advantage of this particular design was the external placement of the detection electrodes, which allowed for easy placement of the electrodes or removal of the capillary in case of capillary blockage or any other problem with the system. The detection limits

obtained using this system were 200 ppb for sodium (Na^+) and chloride (Cl^-). Using a similar design, da Silva and do Lago[54] created their contactless conductivity detector by painting 2 mm silver ring electrodes with a gap of 1 mm onto the surface of a fused silica capillary. Separations of small inorganic ions were reported, and a detection limit of 1.5 μM for Li^+ was obtained.

Both contact conductivity detection and contactless conductivity detection have since been studied extensively in microcolumn and microfluidic devices, with varying electrode geometries, placements, analytical applications and more.[55-71]

1.3.2.2 Previous Developments with Conductivity-Based Photothermal Detection

Photothermal detection using contactless conductivity detection in capillary systems has been previously studied.[44-47] For the conductivity aspect of the detection scheme, the electrodes were composed of 23-gauge stainless steel tubing drilled to have an inner diameter of 390 μm. These electrodes provided a tight fit around any 360 μm outer diameter (o.d.) capillary. Three of these electrodes were used, with excitation signals applied to the two outer 5 mm long electrodes and detection performed through the center 1-2 mm long electrode. The electrodes were arranged with 1 mm spacing to allow sufficient space for capacitive coupling within the capillary without excessive signal leakage between them. A typical excitation signal of 20 V_{pp} at 100 kHz was applied to each excitation electrode and balanced 180° out of phase with each other. The resulting destructive interference nulled the conductivity background at the center detection electrode for more sensitive detection. The signal from the center electrode was subsequently amplified and filtered with a series of two lock-in amplifiers. The first lock-in amplifier was referenced to the excitation frequency for monitoring of the basic conductivity signal. The second lock-in amplifier was referenced to

the modulation frequency of the optical chopper for isolation of the photothermal absorbance signal.

To obtain the photothermal signal, a 488 nm argon laser beam was focused between two of the three electrodes and modulated with an optical chopper. The alternating "on" and "off" phases caused by the chopper created periods of heating in the presence of an absorbing analyte and cooling when the light was removed. These alternating hot and cold periods caused parallel increases and decreases in the conductivity of the detection region. The magnitude of the temperature shift and corresponding conductivity change was determined by the nature and concentration of the absorbing analyte.

Extensive research has been done to characterize this system,[44,47] and it has been shown that, while sensitive, the observed experimental signal is not in agreement with values predicted by simple models. In order to elucidate the reasons for the reduced signals observed, a series of simulations were performed. These simulations indicated that the area being photothermally heated was experiencing drastic changes in temperature with each phase of the laser beam modulation, but by relying on contactless conductivity to monitor the change in capillary systems, this heated volume is small compared to the actual sensing volume. Simulating an effective detection volume with a length of 1mm with a 300mW laser beam focused to 50μm and assuming that 1.6% of the beam's energy was absorbed by the solution, only a 1-degree temperature change was observed. For comparison, simulating a system under similar conditions and using a detection region the same size as the laser beam, a temperature change of 8 degrees was observed. By averaging the temperature change over the larger volume, much of which does not experience a temperature increase caused by the absorption of light, the photothermal signal was drastically reduced. However, due to the capacitive nature of the contactless conductivity detector, creating a conductivity detection volume this small is impossible. In order to obtain a smaller detection region and therefore

an increased signal, one option is to transfer the detection scheme to a microfluidic platform. The fabrication techniques used to create microfluidic devices facilitate the production of electrodes and channel features on the same scale as the laser spot size, reducing the overall conductivity sensing region and maximizing the detected photothermal signal.

1.4 Research Goals and Scope of the Dissertation

The ultimate goal of this research is the development, optimization, and application of a photothermal absorbance detection system on a microfluidic platform for use in studying native analytes. The first step, to be described in Chapter 2, was the fabrication of a robust and simple microfluidic conductivity detector. The resulting poly-dimethyl siloxane (PDMS) "sandwich" device needed to be completely characterized in its response to changes in the conductivity excitation signals and to the geometry and dimensions of the electrodes. Once a microfluidic conductivity detector was developed, it was applied to photothermal absorbance detection, which will be discussed in Chapter 3. This chapter will also describe the development of an all-quartz microchip, which was optically cleaner than the PDMS device. All initial characterization of the device was done with a visible wavelength with a tagged analyte used in previous capillary-based photothermal experiments. While the visible wavelength studies showed that the device was very effective and highly sensitive, relatively few analytes absorbed strongly in the visible range. Chapter 4 will discuss the application of the conductivity detector to photothermal detection using UV wavelength excitation for native analytes. The device was modified in order to place the detection electrodes in an electrically field-free region to remove the problems associated with combining contact conductivity detection with the high voltages used to drive electrophoretic separations. The resulting microchip was characterized using several small biological molecules while varying

the electrical and optical conditions of the setup. The studies in Chapter 4 culminate with the discussion of a separation of native oligonucleotides and determination of their respective detection limits. Finally, Chapter 5 will discuss the application of a microfluidic device designed for use with high performance liquid chromatography (HPLC). This detection method was applied as an end-column detector for a conventional HPLC system and as an integrated device with a particle bed packed into the device. Through the sensitive detection of native analytes with both electrophoretic and chromatographic separations, the goals of this project were attained, and photothermal absorbance detection on a microfluidic platform was proven to be a promising technique for use in small volume, low path length systems.

1.5 References

(1) Auroux, P.-A.; Iossifidis, D.; Reyes, D. R.; Manz, A. *Analytical Chemistry* **2002**, *74*, 2637-2652.

(2) Dapeng Wu, J. Q.; Lin, B. *Journal of Chromatography A* **2008**, *1184*, 542-559.

(3) Erickson, D.; Li, D. *Analytica Chimica Acta* **2004**, *507*, 11-26.

(4) Vilkner, T.; Janasek, D.; Manz, A. *Analytical Chemistry* **2004**, *76*, 3373-3386.

(5) West, J.; Becker, M.; Tombrink, S.; Manz, A. *Analytical Chemistry* **2008**, *80*, 4403–4419.

(6) Terry, S. C.; Jerman, J. H.; Angell, J. B. *IEEE Transactions on Electron Devices* **1979**, *26*, 18801886.

(7) Manz, A.; Miyahara, Y.; Miura, J.; Watanabe, Y.; Miyagi, H.; Sato, K. *Sensors and Actuators B* **1990**, *1*, 249-255.

(8) Harrison, D. J.; Manz, A.; Fan, Z.; Ludi, H.; Widmers, H. M. *Analytical Chemistry* **1992**, *64*, 1928-1932.

(9) Jacobson, S. C.; Hergenroder, R.; Koutny, L. B.; Warmack, R. J.; Ramsey, J. M. *Analytical Chemistry* **1994**, *66*, 1107-1113.

(10) Harris, D. C. *Quantitative Chemical Analysis*; 6 ed.; W. H. Freeman and Company: New York, NY, 2003.

(11) Gebauer, P.; Deml, M.; Bocek, P.; Janak, J. *Journal of Chromatography* **1983**, *267*, 455-457.

(12) Khurana, T. K.; Santiago, J. G. *Analytical Chemistry* **2008**, *80*, 279-286.

(13) Koebel, M.; Zimmt, M. B. *Journal of Physical Chemistry B* **2005**, *109*, 16736-16743.

(14) Li, Q.; Seeger, S. *Analytical Chemistry* **2006**, *78*, 2732-2737.

(15) Liu, Y.; Wipf, D.; Henry, C. *Analyst* **2001**, *126*, 1248-1251.

(16) Matysik, F.-M. *Microchimica Acta* **2008**, *160*, 1-14.

(17) Mawatari, K.; Shimoide, K. *Lab on a Chip* **2005**, *6*, 127-130.

(18) Paul, U. P.; Li, L.; Lee, M. L.; Farnsworth, P. B. *Analytical Chemistry* **2005**, *77*, 3690-3693.

(19) Schulze, P.; Ludwig, M.; Kohler, F.; Belder, D. *Analytical Chemistry* **2005**, *77*, 1325-1329.

(20) Schwarz, M. A.; Hauser, P. C. *Lab on a Chip* **2001**, *1*, 1-6.

(21) Swinney, K.; Bornhop, D. J. *Electrophoresis* **2000**, *21*, 1239-1250.

(22) Wang, J.; Ibanez, A.; Chatrathi, M. P.; Escarpa, A. *Analytical Chemistry* **2001**, *73*, 5323-5327.

(23) Zemann, A. J.; Schnell, E.; Volgger, D.; Bonn, G. K. *Analytical Chemistry* **1998**, *70*, 563-567.

(24) Dovichi, N. J.; Chen, D. *Single-Molecule Optical Detection, Imaging and Spectroscopy* **1997**, 223-243.

(25) Li, Q.; Ruckstuhl, T.; Seeger, S. *Journal of Physical Chemistry B* **2004**, *108*, 8324-8329.

(26) Chervet, J. P.; Soest, R. E. J. V.; Ursem, M. *Journal of Chromatography* **1991**, *543*, 439-449.

(27) Kahle, V. *Biomedical Chromatography* **1999**, *13*, 93–94.

(28) Moring, S. E.; Reel, R. T. *Analytical Chemistry* **1993**, *65*, 3454-3459.

(29) Heiger, D. N.; Kaltenbach, P.; Sievert, H.-J. P. *Electrophoresis* **1994**, *15*, 1234-1247.

(30) Xue, Y.; Yeung, E. S. *Analytical Chemistry* **1994**, *66*, 3575-3580.

(31) Daridon, A.; Fascio, V.; Lichtenberg, J.; Wütrich, R.; Langen, H.; Verpoorte, E.; Rooij, N. F. d. *Fresenius Journal of Analytical Chemistry* **2001**, *371*, 261–269.

(32) Mishra, S. K.; Dasgupta, P. K. *Analytica Chimica Acta* **2007**, *605*, 166-174.

(33) Salimi-Moosavi, H.; Jiang, Y.; Lester, L.; McKinnon, G.; Harrison, D. J. *Electrophoresis* **2000**, *21*, 1291-1299.

(34) Wang, T.; Aiken, J. H.; Huie, C. W.; Hartwick, R. A. *Analytical Chemistry* **1991**, *63*, 1372-1376.

(35) Mogensen, K. B.; Eriksson, F.; Gustafsson, O.; Nikolajsen, R. P. H.; Kutter, J. P. *Electrophoresis* **2004**, *25*, 3788–3795.

(36) Mogensen, K. B.; Petersen, N. J.; Hübner, J.; Kutter, J. P. *Electrophoresis* **2001**, *22*, 3930-3938.

(37) Petersen, N. J.; Mogensen, K. B.; Kutter, J. P. *Electrophoresis* **2002**, *23*, 3528–3536.

(38) Dovichi, N. J.; Harris, J. M. *Analytical Chemistry* **1979**, *51*, 728-731.

(39) Hiki, S.; Mawatari, K.; Hibara, A.; Tokeshi, M.; Kitamori, T. *Analytical Chemistry* **2006**, *78*, 2859-2863.

(40) Li, F.; Kachanov, A. A.; Zare, R. N. *Analytical Chemistry* **2007**, *2007*, 5264-5271.

(41) Llobera, A.; Wilke, R.; Büttgenbach, S. *Lab on a Chip* **2004**, *4*, 24-27.

(42) Mawatari, K.; Naganuma, Y.; Shimoide, K. *Analytical Chemistry* **2005**, *77*, 687-692.

(43) Tokeshi, M.; Yamaguchi, J.; Hattori, A.; Kitamori, T. *Analytical Chemistry* **2005**, *77*, 626-630.

(44) Johnston, S. E. *Applications of Conductivity Detection in Microcolumn Separations*; Doctoral Dissertation, University of North Carolina at Chapel Hill, 2005.

(45) Johnston, S. E.; Fadgen, K. E.; Jorgenson, J. W. *Analytical Chemistry* **2006**, *78*, 5309-5315.

(46) Johnston, S. E.; Fadgen, K. E.; Tolley, L. T.; Jorgenson, J. W. *Journal of Chromatography A* **2005**, *1094*, 148-157.

(47) Dennis, P. J. *Advancements and Applications of Ionic Conductivity Detection to Microcolumn and Microfluidic Separations*; Doctoral Dissertation, University of North Carolina at Chapel Hill, 2007.

(48) Proskurnin, M. A.; Kononets, M. Y. *Russian Chemical Reviews* **2004**, *73*, 1143-1172.

(49) Everaerts, F. M.; Verheggen, T. P. E. M. *Journal of Chromatography* **1972**, *73*, 193-210.

(50) Gas, B.; Demjanenko, M.; Vacik, J. *Journal of Chromatography* **1980**, *192*, 253-257.

(51) Huang, X.; Gordon, M. J.; Zare, R. N. *Journal of Chromatography* **1988**, *425*, 385-390.

(52) Huang, X.; Luckey, J. A.; Gordon, M. J.; Zare, R. N. *Analytical Chemistry* **1989**, *61*, 766-770.

(53) Huang, X.; Pang, T.-K. J.; Gordon, M. J.; Zare, R. N. *Analytical Chemistry* **1987**, *59*, 2747-2749.

(54) da Silva, J. A. F.; do Lago, C. L. *Analytical Chemistry* **1998**, *70*, 4339-4343.

(55) Benedikt Grass, D. S., Andreas Neyer, Roland Hergenröder *Fresenius Journal of Analytical Chemistry* **2001**, *371*, 228–233.

(56) Berthold, A.; Laugere, F.; Schellevis, H.; Boer, C. R. d.; Laros, M.; Guijt, R. M.; Sarro, P. M.; Vellekoop, M. J. *Electrophoresis* **2002**, *23*, 3511–3519.

(57) Grass, B.; Neyer, A.; Johnck, M.; Siepe, D.; Eisenbeiss, F.; Weber, G.; Hergenrodera, R. *Sensors and Actuators B* **2001**, *72*, 249-258.

(58) Guijt, R. M.; Baltussen, E.; Steen, G. v. d.; Frank, H.; Billiet, H.; Schalkhammer, T.; Laugere, F.; Vellekoop, M.; Berthold, A.; Sarro, L.; van Dedem, G. W. K. *Electrophoresis* **2001**, *22*, 2537–2541.

(59) Guijt, R. M.; Baltussen, E.; Steen, G. v. d.; Schasfoort, R. B. M.; Schlautmann, S.; Billiet, H. A. H.; Frank, J.; Dedem, G. W. K. v.; van den Berg, A. *Electrophoresis* **2001**, *22*, 235-241.

(60) Guijt, R. M.; Evenhuis, C. J.; Macka, M.; Haddad, P. R. *Electrophoresis* **2004**, *25*, 4032–4057.

(61) Jeff E. Prest, S. J. B., Peter R. Fielden, Nicholas J. Goddard and Bernard J.; Brown, T. *The Analyst* **2002**, *127*, 1413–1419.

(62) Joseph Wang, M. P., Greg E. Collins, and Ashok Mulchandani *Analytical Chemistry* **2002**, *74*, 6121-6125.

(63) Kubán, P.; Hauser, P. C. *Electrophoresis* **2005**, *26*, 3169–3178.

(64) Kuban, P.; Hauserb, P. C. *Analytica Chimica Acta* **2008**, *607*, 15-29.

(65) Laugere, F.; Guijt, R. M.; Bastemeijer, J.; van der Steen, G.; Berthold, A.; Baltussen, E.; Sarro, P.; van Dedem, G. W. K.; Vellekoop, M.; Bossche, A. *Analytical Chemistry* **2003**, *75*, 306-312.

(66) Lee, C.-Y.; Chen, C. M.; Chang, G.-L.; Lin, C.-H.; Fu, L.-M. *Electrophoresis* **2006**, *27*, 5043–5050.

(67) Lichtenberg, J.; de Rooij, N. F.; Verpoorte, E. *Electrophoresis* **2002**, *23*, 3769–3780.

(68) Liu, Y.; Wipf, D. O.; Henry, C. S. *The Analyst* **2001**, 1248-1251.

(69) Michelle Galloway, W. S., Alyssa Henry, Sean M. Ford, Shawn Llopis,; Robin L. McCarley, a. S. A. S. *Analytical Chemistry* **2002**, *74*, 2407-2415.

(70) Prest, J. E.; Baldock, S. J.; Bektas, N.; Fielden, P. R.; Treves Brown, B. J. *Journal of Chromatography A* **1999**, *836*, 59-65.

(71) Pumera, M.; Wang, J.; Opekar, F.; Jelinek, I.; Feldman, J.; Lowe, H.; Hardt, S. *Analytical Chemistry* **2002**, *74*, 1968-1971.

Chapter 2: Development of a Microfluidic Device for Conductivity Detection

2.1 Introduction

Initial work on the development of a microfluidic photothermal absorbance detector involved the incorporation of a contact conductivity detector that was compatible with the electronic and optical components of the photothermal absorbance detector onto a microfluidic device. In the previously described capillary-based system, the capacitively coupled contactless conductivity detector (C^4D) consisted of two steel tube electrodes into which a capillary was inserted. The disadvantage to this method, as discussed in Chapter 1, was the large effective sensing region, created by limits in fabrication and by the nature of capacitive coupling, compared to the small laser spot size. The result was a significant reduction of the photothermal signal and high limits of detection.[1-3] While there are examples of capillary-based conductivity detection methods in which the electrodes directly contact the solution and eliminate the limits posed by contactless detection, those devices are neither easily fabricated nor.[4]

By fabricating a conductivity detector on a microfluidic platform, many of these difficulties can be circumvented. Microfabricated devices utilizing both contactless and contact conductivity detection are prevalent in the literature, and a number of fabrication methods are discussed.[1,3-25] One of the first examples of a conductivity detector used in a lab-on-a-chip device was a contact conductivity detector initially reported by S.J. Baldock.[26] The device was fabricated using poly-dimethyl siloxane (PDMS) molded from a copper

template to form a 120 mm long channel. A single detection electrode composed of a 20 μm platinum-iridium wire was placed between the two PDMS layers and across the separation channel before bonding (Figure 2-1A). The electrode was connected to a commercially available high-voltage meter and used to passively monitor the local potential. The device made use of isotachophoresis (ITP) to separate and detect a series of metal cations, and the behavior of the microfabricated device was compared to an equivalent capillary system. The microdevice was later modified to incorporate a more sensitive dual electrode design (Figure 2-1B). Two 200 μm diameter platinum wires were positioned and held in place with UV-curable adhesive across a 300 μm channel milled a in poly-methyl methacrylate (PMMA) chip. The device was used to separate selenium(IV) and (VI), and the resulting detection limit was reported to be 6 μM.[10,22,23,27]

A number of different electrode geometries were investigated by Grass et al.[5] The electrodes were composed of a thin film of 40-60 nm chrome (Cr) followed by 200-300nm of platinum (Pt) applied to a PMMA substrate. The metal was sputtered onto a substrate covered with a patterned resist, and the excess metal was removed using a lift-off procedure, leaving only the desired design. Two of the geometries discussed consisted of electrodes patterned directly across the separation channel with 77-79 μm separating the tips, which were either 12 μm or 49 μm wide (Figure 2-1C). The remaining electrodes were arranged parallel to each other and perpendicular and across the width of the channel. Four parallel electrodes were fabricated with various widths and gap sizes between them (Figure 2-1D). Conductivity measurements could be taken between two of the four electrodes to provide data for six different gap sizes. The behavior of the electrodes and the conductivity response was compared using identical ITP runs. Although all of the designs proved successful,

narrower, facing electrodes were found to give the most sensitive response. The parallel designs were slightly less sensitive, but had the advantage of easier alignment during fabrication of the device.

Using another approach, Galloway and Soper[20] presented a device using contact conductivity detection in order to analyze polymerase chain reaction (PCR) products separated via reverse-phase ion-pair capillary electrochromatography (RP-IPCEC). The detector was fabricated using polished platinum wires inserted into groves in the PMMA device prior to bonding (Figure 2-1E). A bipolar pulse waveform was used as the excitation signal for the detector and applied to one of the two electrodes. The pulse frequency was generally set at 5 kHz, and the duration was determined based on the detection cell time constant. The separation electric field strength was kept low, and baseline separation of the PCR products was achieved at 67 V/cm. The conductivity detector provided a detection level of approximately 10^{-21} mol. The same group also presented a device that demonstrated even greater sensitivity using a similar, but modified setup.[21] In this case, the electrode wires were placed facing each other across the 15 μm separation channel. A series of amino acids were separated using the device, and a detection limit of 8 nM was achieved for alanine. It was concluded that this limit is comparable to the expected detection limit for unlabeled amino acids using indirect laser fluorescence.

Contactless conductivity detection has also been used with microfabricated devices. The separation of detection electrodes from direct contact with the solution is useful for isolating them from the high DC voltages used to drive electrophoretic separations. The nature of microfabricated systems makes use of very thin insulating layers between the electrodes and the solution of interest, as compared to capillary-based systems. As a result,

broadening of the detection region caused by capacitive coupling is reduced. Planar electrode geometries often used for contactless detectors in microchips also reduced leakage between them, but capacitive coupling efficiency is decreased in comparison to coaxial capillary designs.[6,11-18,24]

A simple example of contactless detection was explored by Wang et al.[24] The device was fabricated using hot embossed PMMA. The planar electrodes were composed of 10 μm thick aluminum foil cut into 0.8 mm x 10 mm strips and adhered to the outer surface of a 125 μm thick PMMA cover plate. In order to reduce electronic cross-talk between the electrodes, the electrodes were placed in an anti-parallel conformation (Figure 2-1F). A 200 kHz 5 V_{pp} sinusoidal excitation signal was applied to one of the two electrodes, and a lock-in amplifier was used to isolate the detected signal. A detection limit for K^+ of 1.2 μM was achieved using this setup. The device was also used to separate and detect a number of alkyl methylphosphonic acids and the breakdown products of a number of chemical warfare agents, demonstrating its use for real world analyses.[12] An interesting modification to this detection scheme was a movable detector presented by the same group.[11] The device made use of the same aluminum foil electrodes mounted on a smaller piece of PMMA held in place with PVC clamps. The electrodes could be moved along the length of the channel to examine the analytes at different points during the separation.

Further modification of the microfabricated contactless conductivity detector was presented by Lichtenberg, Rooij, and Verpoorte.[18] The glass-based device contained 400 μm wide platinum thin-film electrodes which were fabricated perpendicular to and in the same plane as the separation channel, with 10-15 μm of glass separating them (Figure 2-1G). In order to reduce stray capacitance on the chip, each electrode was surrounded by two

shielding electrodes. To improve the limit of detection of the device, field-amplified sample stacking (FASS) was used. The resulting detection limits were amplified by up to four times those observed without preconcentration.

Several groups working in conjunction at Delft University of Technology in the Netherlands produced a contactless conductivity detection device that made use of a unique four-electrode design (Figure 2-1H).[6,8,15] The 600 nm thick aluminum electrodes were deposited in recesses etched into the glass substrate such that the metal was flush with the substrate surface and would not interfere with bonding. The electrodes were physically and electronically isolated from the channel by a 30 nm thick layer of silicon carbide. Channels for fluid flow were etched into a second substrate and the two were bonded together. In a two-electrode design, the excitation voltage is applied to one electrode and detected at the second. In the case of this four-electrode design, the AC excitation voltage was applied across the two outer electrodes, and the current between the two was measured with a transimpedance amplifier. A high impedance differential-amplifier was used to measure the differential voltage between the two inner electrodes. The ratio of the current between the outer electrodes to the voltage between the inner electrodes was proportional to the conductivity of the fluid in the detection region. Stable measurements were taken up to 10 kHz, and detection limits in the low μM range were observed.

Despite the advantages of microfabricated contactless conductivity detection over similar capillary-based detectors, there is a significant loss of sensitivity due the dielectric layer. Assuming the detection signals can be easily isolated from the high voltage of electrophoresis and the electrodes are not damaged by the voltages, improved contact conductivity detection limits are much more appealing for use with photothermal detection.

A review of the literature indicates that a contact conductivity detector with thin film electrodes arranged in an antiparallel geometry was determined to be the most easily fabricated and promising for later application to conductivity-based photothermal detection.

2.2 Experimental

2.2.1 Materials

All chemical compounds obtained for these procedures were used as shipped with no further modification. Sodium hydroxide (NaOH) solution, lithium chloride (LiCl), and sodium chloride (NaCl) were obtained from Fisher Scientific (Fair Lawn, NJ), and potassium chloride (KCl) was obtained from Mallinckrodt (Paris, NY). The 2-morpholinoethansulfonic acid (MES) and L-histidine (His) were purchased from Sigma (St. Louis, MO). All buffers and solutions were prepared with deionized water from a Barnstead Nanopure Filtration System (Boston, MA). The standard electrophoresis running buffer was a solution of 20 mM MES and 20 mM His at pH 6.1. All solutions were further filtered with a 0.2 µm nylon membrane filter (Whatman, Brentford, Middlesex, UK) before injection into the reservoirs.

Substrates used for chip fabrication were 4 in x 4 in x 0.9 mm (length x width x thickness) white crown (B-270) glass grade PG wafers coated with 1200 Å film of low reflectivity chrome and 5300 Å of AZ 1518 photoresist (Telic, Valencia, CA). Blank substrates were 4 in x 4 in x 0.6 mm grade CG wafers obtained from Telic (Valencia, CA). Four inch diameter silicon wafers were purchased from Silicon, Inc. (Boise, ID). Poly-dimethyl siloxane (PDMS, Sylgard 184) was bought through Ellsworth Adhesives (Germantown, WI) and produced by Dow Corning (Corning, NY).

2.2.2 Microchip Fabrication

2.2.2.1 Electrode fabrication

Electrodes for the conductivity detector were fabricated on B-270 white crown glass blanks (Telic, Valencia, CA), which were cut into 1 in x 2 in substrates using a Basic Dicer II (Dicing Technology, Longwood, FL). All substrates were immersed in Nanostrip 2x (Cyantek Corperation, Fremont, CA) for up to 15 minutes in order to remove any organic residue on the surfaces. The substrates were then rinsed with deionized water and dried with pressurized nitrogen gas. A flow diagram of the electrode fabrication process is shown in Figure 2-2.

Photomasks for the electrodes were designed using TurboCAD v. 9.2 Student Edition (Novato, CA). The completed designs were sent to The Photoplot Store (Colorado Springs, CO) for printing on a mylar film base with an Accumax ARD7 emulsion layer (Kodak, Rochester, NY). Resolution on these masks provided a minimum feature size of 6 μm. All designs were dark field and RRED (right reading emulsion down). The resulting prints are the reverse of the original design so that the emulsion side of the mask can directly contact the photoresist, giving the correct exposure and maximizing the resolution of the features. All electrodes were plotted anti-parallel to each other, and the design included masks for electrodes with different electrode widths (10 μm to 160 μm), gap sizes (10 μm to 160 μm), and electrode overlap lengths (100 μm to 400 μm, to ensure the electrodes cross the width of the channel).

A film of S1813 was applied to the electrode substrates through spin coating using a Model 6700 Spincoater (Specialty Coating Systems, Indianapolis, IN). The resist was applied in a thick layer via pipetting, and the excess was removed spinning with an initial

ramp from 0 to 300 rpm over 5 seconds and held at 300 rpm for an additional 5 seconds. The resulting even layer was further thinned by increasing the spin rate to 4000 rpm over 5 seconds and then holding the spin rate at 4000 rpm for 35 seconds providing an overall thickness of approximately 1.5 μm. After ensuring a uniform film of photoresist, the coated substrate was placed into a mechanical convection oven (Barnstead Thermolyne, Boston, MA) and baked at 95°C for 10 minutes.

The appropriate photomask was placed face down directly onto the coated substrate for exposure. To prevent shifting of the mask and to ensure good contact between the mask and the substrate surface, a 4 in x 4 in x 0.9 mm quartz blank (Telic, Valencia, CA) was placed as a weight on top of the mask. The photoresist was exposed through UV flood exposure with a J200 UV Exposure System (OAI, Milpitas, CA) for 65-75 seconds. Following exposure, the coated substrate was immersed in MF-319 developer for 45-60 seconds (Shipley, Marlboro, MA) to remove the exposed areas. The substrate was removed from the developer, rinsed with deionized water, and dried with pressurized nitrogen gas. The design was then observed under an optical microscope to ensure complete development. Any obstructing resist left in the exposed area was carefully removed to ensure no breaks in the electrodes.

The metal thin films making the electrodes were deposited using a Model IBSe Ion Beam Deposition System (South Bay Technologies, San Clemente, CA). The films were composed of an adhesive layer of 1-10 nm chrome followed by a 20-100 nm layer of platinum, depending on the experimental parameters. The substrate was then immersed in a bath of acetone and sonicated using a Model 2510 sonicator (Branson Ultrasonics, Danbury,

CT) to remove, or "lift off," the photoresist and excess metal film not directly contacting the substrate surface.

2.2.2.2 Channel Mold Fabrication

Silicon wafers (Silicon, Inc., Boise, ID) were used as the substrate for the fabrication of a master for PDMS molding. The substrate was pretreated by immersion in buffered oxide etch (BOE) consisting of 1:10 HF/NH_4F solution (Transene, Danvers, MA) for 1 minute, rinsed with deionized water, and dried with pressurized nitrogen. The surface was dehydrated by baking at 200°C for 5 minutes in an Isotemp convection oven (Fisher Scientific, Fair Lawn, NJ). The wafer was then placed in a Model 6700 Spincoater (Specialty Coating Systems, Indianapolis, IN) and spun at a rate of 3500 rpm. Upon reaching the maximum speed, the wafer was sprayed once with acetone, twice with isopropanol, and spun for an additional 30 seconds to dry before placing it on a hot plate at 125°C for 5 minutes.

With the pretreatment completed, the silicon wafer was placed back into the spincoater. Approximately 3 mL of SU-8 2050 was dispensed in the center of the wafer. The wafer was spun at 500 rpm for 10 seconds with a 5 second ramp time, in order to completely coat the surface with the viscous photoresist and to ensure uniformity in photoresist thickness. The spincoater was then ramped to 2000 rpm over 5 seconds and held for 30 seconds in order to produce a layer thickness of 75 μm.

The coated silicon wafer was then placed on a larger B-270 white crown glass blank for added support. The wafer and glass were placed on a hotplate (Barnstead Thermolyne, Boston, MA) at 65°C and covered with a tent of aluminum foil to protect it from dust. The

temperature on the hot plate was increased to 95°C and held for 10 minutes after which the hotplate was turned off and both it and the wafer were cooled slowly to room temperature.

Photomasks for the channels were designed using TurboCAD v. 9.2 Student Edition (Novato, CA) and sent to The Photoplot Store (Colorado Springs, CO) for printing on a mylar film base. All designs were dark field and RRED (right reading emulsion down). The appropriate photomask was placed face down directly on the SU-8 coated silicon wafer. The resist was exposed using a Model B 100 AP 100W Long Wave UV lamp (Black-Ray UVP Inc., San Gabriel CA) for 90 seconds. Exposure of the SU-8 to UV light induced the first step of cross-linking of the photoresist polymer. The second and final step occurred during the post-exposure bake. The wafer was placed back on the hotplate at 65°C and covered with foil. The temperature was then increased to 95°C and held for 7 minutes, after which both the substrate and hot plate were cooled slowly to room temperature.

To develop the SU-8, the coated silicon wafer was immersed in an adequate volume of SU-8 developer (Microchem, Newton, MA) in order to cover the surface. The solution was gently agitated for 7 minutes to remove unexposed SU-8. Any white residue observed indicated underexposure of the photoresist. To halt the development, the wafer was rinsed with isopropanol, rinsed with deionized water, and dried with pressurized nitrogen gas. Finally, the wafer was placed back on the hot plate and the temperature was increased to 200°C for 30 minutes.

2.2.2.3 PDMS Chip Fabrication and "Sandwich" Chip Design

The PDMS used to fabricate the channel layer consisted of a silicone elastomer base and a curing agent. To obtain the correct rigidity for the chip, the two were thoroughly

mixed in a 10:1 ratio. The mixture was degased on the counter top over 30 minutes. The PDMS channel layer was fabricated with a silicon master mold (discussed previously). To restrict the size of the PDMS, a 1 in x 2 in in-house machined mold was placed over the silicon master and held in place with HN type Kapton tape (DuPont, Wilmington, DE). The master and mold were placed on a hot plate, and approximately 2 mL of PDMS was dispensed to fill the mold. The hot plate was covered with aluminum foil to protect against dust and particulates. The hot plate was then adjusted to 35°C for 15 minutes to remove any remaining gas in the polymer. The temperature was increased to 85°C in steps of 15°C/15 min until the PDMS was approximately 90% cured. The still tacky PDMS was carefully removed from the mold and excess polymer was cut away with a razor blade. Access holes were punched at the ends of the channels using one of two in-house machined punches 2 mm or 3 mm in diameter.

The final chip consisted of the PDMS layer "sandwiched" between the electrode substrate and a cover plate (Figure 2-3). An in-house built positioner was used to align and lay the PDMS layer over the electrode substrate. The positioner consisted of a pair of holding arms for the PDMS and three translational stages, providing adjustments in three dimensions. A SMZ-U stereoscope with 10x objective (Nikon, Mellville, NY) was used to observ the electrode-channel placement.

Once properly aligned and contacted, the incomplete curing of the PDMS let the polymer conform around the metal electrodes and maximized adhesion to the electrode substrate. The cover plate was made from a Gold Seal microslide (Erie Scientific, Portsmouth, NH) cut into 1 in x 2 in sections. Access holes approximately 3 mm in diameter were drilled through the cover plate using a MB 1000-1 powder blaster (Comco, Inc.,

Burbank, CA). The cover plate was then placed over the PDMS layer, and the "sandwich" chip was gently pressed together. A thin layer of uncured PDMS was applied around the edges of the cured PDMS layer to act as a sealant between the layers. The PDMS then cured completely overnight at room temperature.

All reservoirs and connectors applied to the cover plate were attached using a UV curable optical adhesive (Norland, Cranbury, NJ). For the pressure driven chips, an N-129H nanoport connection (Upchurch Scientific, Oak Arbor, WA) with reservoir, nut, and ferrule was used as the entrance port for connecting 75/360 (i.d./o.d.) polyetheretherketone (PEEK) tubing to the chip. An N-131 nanoport connection (Upchurch Scientific, Oak Arbor, WA) was used as an outlet for fluid flow with a length of 1/16" Teflon tubing (Upchurch Scientific, Oak Arbor, WA) leading to a waste container. For the electrokinetic chip, small glass cloning cylinders (Fisher Scientific, Fair Lawn, NJ) were attached to the cover plate to act as fluid reservoirs. The completed microchips are shown in Figure 2-4.

2.2.3 Pressure Driven Flow and Electrophoresis Setups

Initial measurements made use of helium gas to apply pressure to an in-house machined pressure bomb containing the running buffer. The pressure was set to give a flow rate of approximately 17 μL/min. A six port valve injector (VICI Valco Instruments Co. Inc., Houston, TX) with a 750 μL injection loop was used to hold and inject the analyte solution.

Electrokinetic flow was provided by an in-house built high voltage power supply with 4 high voltage output modules (10A12-P4 modules, UltraVolt, Ronkonkoma, NY) controlled by the DAQ board. Platinum wires were used to apply the voltages to fluid reservoirs, and

the voltages were controlled through the analog output of a PCI 6713DAQ board (National Instruments, Austin, TX) by custom software written in LabVIEW ((National Instruments, Austin, TX). Appropriate running voltages were determined using a solution of rhodamine B and running buffer in the sample reservoir. Gated injections[28] were performed by altering the electrophoresis voltages to flow fluid from the sample reservoir into the separation channel. The fluid flow behavior was viewed through a TE300 inverted microscope (Nikon, Melville, NY) equipped with a 20X objective, a high pressure mercury lamp, and a NTE/CCD-512-EBFT video camera (Roper Scientific, Trenton, NJ).

2.2.4 Conductivity Setup

Schematic diagrams of the setup for both pressure driven and electrokinetic flow are shown in Figures 2-5 and 2-6. The AC excitation signal for the conductivity detection was provided by a DS345 digital function generator (Stanford Research Systems, Sunnyvale, CA). All studies were performed at 100 kHz unless otherwise specified for the frequency-dependent studies. Typical excitation voltages varied between 0.25-1 V_{pp}, but extended up to 5 V_{pp} in low response conditions. The excitation signal was passed through a 3 kV, 100 pF radial disc capacitor (Panasonic-ECG, Secaucus, NJ) before being applied to the electrodes via a micro-alligator clip (Mueller Electronics Co., Cleveland, OH). The capacitor acted to isolate the sensitive electronics from the high DC voltage used for electrophoresis. After passing through the detection cell, the signal passed through a second alligator clip and capacitor. The microfluidic chip was housed in a grounded aluminum box to provide shielding against external noise.

The signal was amplified using a current-to-voltage amplification circuit consisting of an OPA602 operational amplifier (Texas Instruments, Dallas, TX) with a 1 MΩ feedback resistor (Multicomp, Chicago, IL) to give a 10^6 V/A gain. Surface mounted 1000 pF capacitors (Newark Electronics, Chicago, IL) added to the circuit removed any high frequency noise from the power supply or feedback loop of the operational amplifier. A second grounded aluminum box provided shielding for the electronic circuit. Power to the operational amplifier was provided by a Model 1310 Power Supply (Global Specialties, New Haven, CT) at ±15 V.

The signal was isolated and amplified by a SR810 digital lock-in amplifier (Stanford Research Systems, Sunnyvale, CA). The lock-in was referenced to the DS335 function generator via the external reference setting. Other settings on the lock-in were a 100 ms time constant with a 24 dB/octave slope, and the line and 2x line filters were used to minimize noise from the AC power lines. The sensitivity was adjusted to avoid saturation based on the maximum signal produced under given conditions. The lock-in amplifier output was digitized with a PCI-MIO-16XE-50 DAQ card (National Instruments, Austin, TX) and collected with a personal computer equipped with custom software written in LabVIEW (National Instruments, Austin, TX). Data analysis was performed using Igor Pro (Wavemetrics, Lake Oswego, OR) with baseline subtraction.

2.3 Results and Discussion

The PDMS sandwich chip was used to conduct a number which investigated the behavior and stability of the conductivity detector under a number of conditions such as excitation voltage, excitation frequency, and electrode dimensions. The electrodes were

fabricated with a number of variations in their dimensions, including electrode width, gap size between the excitation and detection electrodes, length of electrode overlap, and metal film thickness and composition. Also studied were the effects of excitation voltage and frequency on these different electrodes. Finally, the detector was tested with a separation of simple tagged analytes.

2.3.1 Electrode Properties and Excitation Investigations

2.3.1.1 Electrode Widths and Excitation Voltage

Taking into account the anti-parallel geometry of the conductivity detector electrodes in which the electrodes completely traverse the channel, two simple approaches to adjust the electrode dimensions included varying the electrode widths and the electrode gap widths. Focusing on the electrode width, the metal film resistance was expected to increase inversely with width.[29] As such, electrodes with greater widths should provide a higher conductivity response. In the case of electrokinetic flow, electrode width is limited by the electric field strength due to the potential for electrolysis and the production of microscopic gas bubbles. Both phenomenon disrupt fluid flow and detection and can damage the electrodes. For the present studies, this concern is eliminated by using pressure driven flow to drive the fluids, thus allowing the investigation of any electrode dimensions.

To investigate the effect of varying the electrode width, a PDMS sandwich chip was fabricated using a mask with five electrode pairs having widths of 10, 20, 40, 80, and 160 μm with a constant gap size of 40 μm. The 20 μm wide electrode pair contained a break in the metal film and was not used. All measurements were taken with a 100 kHz excitation frequency. The remaining four electrode pairs were studied at varying excitation voltage,

starting at 0.1 V_{pp} and increasing until the maximum background signal reached the lock-in amplifier input limit.

The analyte was a 250 μL plug of 50 ppm solution of sodium chloride, and the running buffer was 20 mM MES/His. The conductivity response of the background (buffer) and the analyte were plotted against excitation voltage as shown in Figure 2-7. As expected given the scaling behavior of microfabricated features, both the background signal and the analyte signal increase with increasing electrode width for the three narrowest electrodes. Of particular interest, the 160 μm wide electrodes provided no increase in conductivity response over the electrodes 80 μm wide, indicating a cut off point after which the increase in width has little effect on the detector sensitivity. As this is near the microchip's channel depth, 75 μm, it is believed that the signal behavior observed relies primarily on the resistance of the fluid in the detection region and, thus, the channel depth. A schematic diagram of the electric field lines for three different electrode widths is shown in Figure 2-8. In the first example (Figure 2-8A), the electrodes are narrower than the depth of the channel, and the field lines are constricted primarily at the electrodes, creating greater resistance and lower signal. Figure 2-8B shows case in which the electrodes are the same width as the channel depth. The electric field lines in this example are equally constricted by the electrodes and the channel. The final example (Figure 2-8C) shows a design where the electrodes are wider than the channel depth. In this case, the electric field is restricted primarily by the depth of the channel, and the field lines focus on the inner edges of the electrodes. Therefore, electrodes of any width beyond the channel depth provide no benefit in detected signal and would be more susceptible to interact with high DC voltages in electrophoretic running conditions.

Figure 2-9 plots the background conductivity noise and signal to noise ratio for sodium chloride with respect to excitation voltage. For the two smaller widths, the 10 μm width displayed very little variation in noise except at the lowest applied excitation voltages, and the 40 μm demonstrates a relatively linear noise change with regard to excitation voltage. The resulting signal to noise versus excitation voltage plots for these two electrode widths were essentially linear. Data obtained with two wider electrodes, 80 and 160 μm, was collected over a shorter range of excitation voltages, due to the lock-in input limits, and the noise had a more erratic pattern. The amplitude stability of the function generator has been shown to be a major contributor to background noise in previous studies, with the exact contribution dependent on the signal output.[1,3] As the wider electrodes were more sensitive to signal input, they were also more sensitive to noise from the function generators.

2.3.1.2 Electrode Gap Size and Excitation Signal

In order to investigate the effect of varying the electrode gap size, a second chip was fabricated with five pairs of 40 μm wide electrodes with different gap sizes. The gaps were 10, 20, 40, and 160 μm. Pressure driven flow was used in this study. As with the electrode width studies, the different gap sizes were examined with respect to increasing excitation voltage. For these studies a constant excitation frequency of 100 kHz was maintained. The plots in Figure 2-10 demonstrate the electrode responses with increasing excitation voltage. According to this data, the 10 μm electrode gap had a significantly higher conductivity signal than the 20, 40, and 160 μm gap electrodes. The background signal of the 10 μm gap electrodes was roughly double that of the other three, all of which had relatively similar background signals. The 50 ppm sodium chloride analyte demonstrated an even more

extreme difference for the 10 μm gap electrode signal. The two mid-sized electrodes, 20 μm and 40 μm, exhibited similar signal behavior, and the 160 μm gap signal was slightly lower. Noise for all of the electrode gap widths followed a trend similar to the analyte response (Figure 2-11). Despite having higher noise, the 10 μm gap signal to noise ratios were still significantly greater than the others, indicating the advantage of using closely spaced electrodes to reduce the resistance in the detection region.

In order to study the effect of excitation frequency on the electrodes, a second chip was fabricated with electrode widths of 40 μm and varying electrode gap sizes, and the straight channel for pressure driven flow was replaced with a molded PDMS cross channel for electrokinetic flow. The cross channel design was used for gated injection of a 10 ppm solution of potassium chloride, which was placed in the top reservoir. The 20 mM MES/His running buffer was placed in the remaining three reservoirs. Voltages applied to the microchip were kept at a low electric field strength of 150 V/cm in order to prevent electrolysis at the detection electrodes. Gaps of 10, 40, and 160 μm were used for this study.

Previous studies using capillaries and contactless conductivity indicate that the optimal excitation frequency was approximately 375 kHz, but the SR810 lock-in amplifier, which has a maximum frequency input of 102 kHz, was found to have significantly less noise than the SR844 RF lock-in.[1] Therefore, the frequency range for this study was done over a range of 10 to 100 kHz with an excitation voltage of 0.25 V_{pp}. Figure 2-12 shows the response of background conductivity and the signal of a 1 second injection of potassium chloride analyte plotted against the excitation frequency. A gradual increase in background and signal for all three electrode gap sizes was observed as a function of frequency. The noise response remained relatively independent of frequency for all three electrodes,

resulting in a gradual increase in the signal to noise ratio as a function of excitation frequency (Figure 2-13). For the frequency range studied, the optimal excitation frequency was determined to be 100 kHz.

2.3.1.3 Electrode Thickness and Composition

Since the electrodes are central to the detection scheme and cannot be replaced without fabricating new chips, it is vital that they are composed of a material that is robust and reliable. While using the electrokinetic chip, high electric field strengths caused electrolysis and the formation of gas bubbles at the electrode edges. The bubbles tended to form erratically and sometimes violently, degrading the adhesive layer and causing the platinum to peel away from the substrate surface. Another concern was oxidation of the chrome layer, which could be exposed at the electrode edges or through pits in the platinum layer. Although electric field strengths in the electrode region were limited to below 200 V/cm for most studies, some damage was observed over time.

A number of electrode thicknesses were studied to determine the most robust combination. The compositions fabricated were the 10 nm Cr/20 nm Pt used previously, as well as 1 nm Cr/100 nm Pt and 5 nm Cr/10 nm Pt. The 5 nm Cr/10 nm Pt electrodes did not survive under the separation voltages and were not used for this analysis. The responses of background conductivity and the signal of a 1 second injection of 50 ppm sodium chloride for 10 nm Cr/20 nm Pt and 1 nm Cr/100 nm Pt are shown in Figure 2-14. Background signal for both electrode thicknesses were observed to be identical, and the signal for the 10 nm Cr/20 nm Pt electrodes was slightly lower. The thicker electrodes also gave slightly higher noise and signal to noise ratio (Figure 2-15). In general, the thicker electrodes had a slightly

better performance than the thinner electrodes and demonstrated a much longer lifetime throughout the course of experimentation.

In attempting to determine the optimal material for the electrodes, several electrodes composed of iridium were fabricated. Iridium had the advantage of adhering directly to the substrate surface, avoiding the need for an additional adhesive layer. Electrically, iridium and platinum exhibit similar behavior, having specific resistances of 4.8×10^{-8} Ωm and 5.7×10^{-8} Ωm, respectively. Initial testing with only the DC electrophoresis running voltage or only the AC excitation voltage showed promise. Upon application of both fields, the iridium immediately degraded and the electrodes were destroyed. The cause of the failure was investigated, but a satisfactory answer was never determined, so thicker Cr/Pt electrodes were used for all future experimentation.

2.3.2 Sample Separation

A separation of three simple inorganic salts, potassium chloride, sodium chloride, and lithium chloride, demonstrated the power of the microfabricated conductivity detector. A 1 second injection of a 10 ppm solution of three salts was detected using the electrokinetically driven sandwich chip with a running buffer of 20 mM MES/His. Excitation was induced by a 0.25 V_{pp} 100 kHz sine wave applied to electrodes with 20 μm width and 40 μm gap, and electrophoresis was run under a 150 V/cm electric field. The electropherogram is shown in Figure 2-16. For this separation, the signal to noise ratios were 1270, 1840, and 3990 for K^+, Na^+, and Li^+ respectively. As a comparison, the reported[1,3] signal to noise values for the same ions separated with standard capillary electrophoresis and detected using a capacitively coupled contactless conductivity detector (C^4D) are listed alongside those for the sandwich

chip in Table 2-1. All detection electronics are identical for the two systems. Based on the values presented in the table, the microfluidic chip not only has detection limits several times lower but can also perform the separation in almost one fifth the time.

2.4 Conclusions

The successful design and fabrication of the microfluidic glass-PDMS-glass "sandwich" chip with an integrated conductivity detector has now been realized. The central PDMS layer provided flexibility to molding around the metal electrodes, effectively sealing the chip. Chips for both pressure driven and electrokinetic flow were produced, and the detector proved viable under both conditions.

The microfabricated conductivity detector was fully tested to understand its behavior. Modifications to the electrodes included electrode gap size, electrode width, and metal film thickness and composition. The conductivity signal was shown to scale inversely with gap width as the volume of resistive solution between the electrodes was reduced. Although the noise likewise scaled inversely with the gap width, it did so at a reduced rate. As a result, the smaller gap sizes provided the greatest signal to noise ratio and lowest detection limits. Electrode width studies followed the trends expected by theory, i.e. wider electrodes provided lower resistance and greater conductivity signal. However, a limit to this trend was observed for electrode widths greater than 80 μm, and larger widths provided no increase in sensitivity. When using the wider electrodes in conjunction with electrokinetic flow, consideration must be given to the electric field strength as electrolysis and gas bubble formation can be a problem. The final electrode dimension studied was the metal film thickness. Electrodes composed of 10 nm chrome adhesive layer under 20 nm of platinum

were fairly robust, but did degrade over time. The thinnest films studied did not last when placed under a combination of AC excitation voltage and DC electrophoresis voltage. Electrodes 100 nm and thicker proved to be the most robust while yielding favorable signal to noise ratios.

Studies concerning the conditions of conductivity excitation were also performed. The signal response to excitation voltage proved to be directly linear for all electrodes studied. Noise scaled linearly for electrodes that gave lower signals, but was less predictable for the more sensitive electrodes, such as those with greater widths. The conductivity signal for increasing excitation frequency was less pronounced, creating a modest signal to noise maximum near 100 kHz.

A separation of inorganic ions was used to demonstrate a simple application of the PDMS "sandwich" chip. The high signal to noise ratios for the analyte peaks demonstrated the advantage of small detection regions and of fabricating the chip with electrodes directly contacting the solution. This was especially true in comparison to the contactless conductivity detectors previously used with capillaries. The PDMS "sandwich" chip was easily fabricated and permitted rapid exploration of detection geometry. However, PDMS is not as optically clean as glass or quartz, and its elasticity allows for swelling or shrinking depending on the solvents used. These factors would result in increased light scatter and changes in the detection cell geometry that make it not an ideal material for photothermal absorbance detection.

2.5 Tables and Figures

Table 2-1: Comparison of the capillary based C^4D method to the microfluidic sandwich chip conductivity detection method. Limits of detection (LOD) were calculated at S/N=3.

Property	Capillary C^4D	Microfluidic Chip
Electric Field Strength	310 V/cm	150 V/cm
AC Excitation Voltage	20 V_{pp}	0.25 V_{pp}
Conductivity Noise	3 μV	2 μV
Total Analysis Time	~7 minutes	~90 seconds
Potassium Ion S/N (Approx. LOD)	420 (71 ppb)	1270 (24 ppb)
Sodium Ion S/N (Approx. LOD)	410 (73 ppb)	1840 (16 ppb)
Lithium Ion S/N (Approx LOD)	610 (49 ppb)	3990 (7.5 ppb)

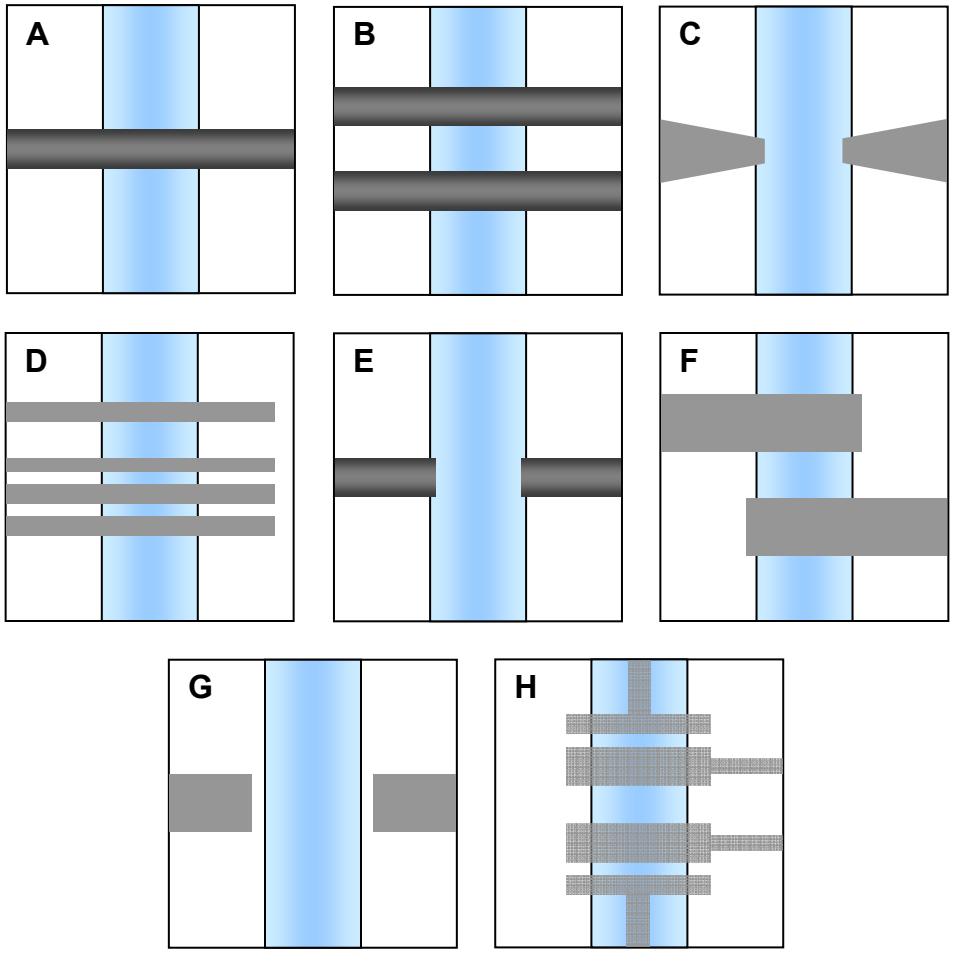

Figure 2-1: Diagrams of various electrode geometries.

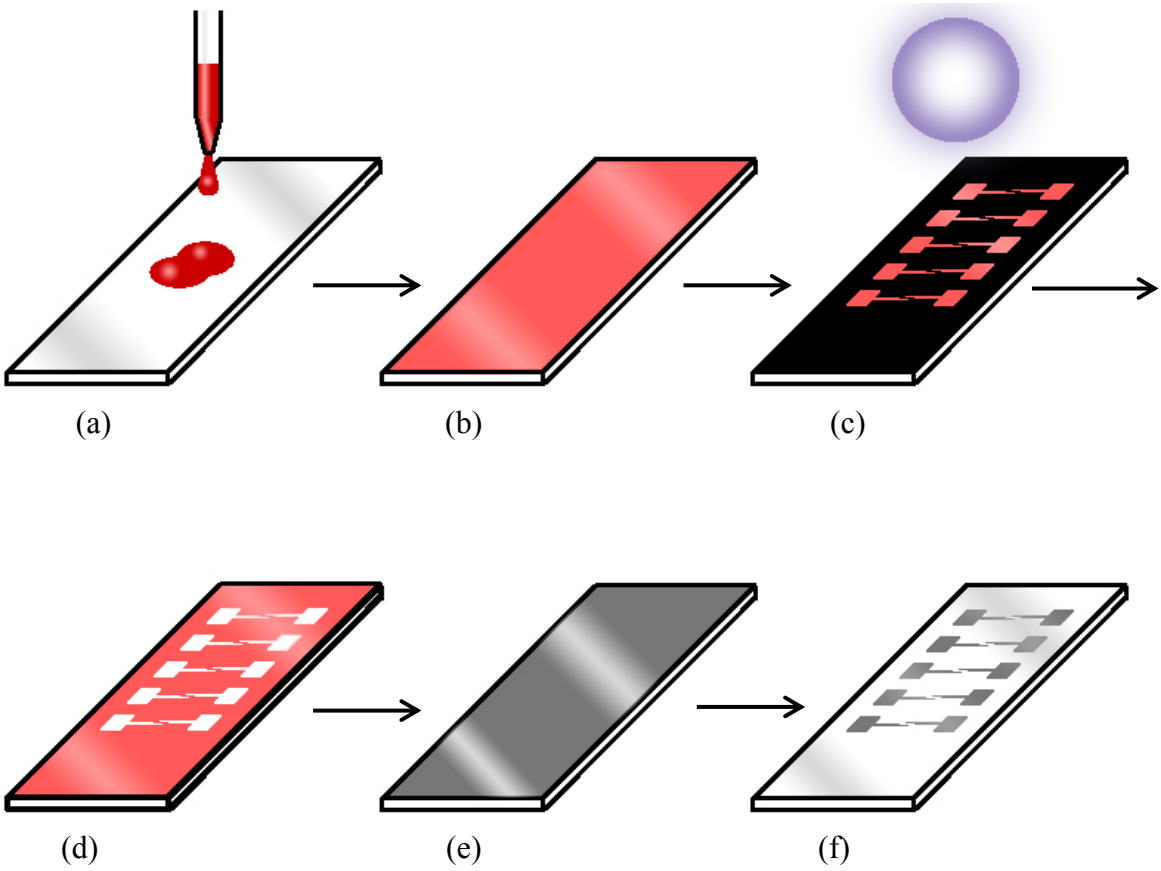

Figure 2-2: Fabrication of the metal thin film electrodes via the lift off method. From the top left, (a) a layer of S-1813 photoresist is applied to the substrate, (b) the substrate is spun to provide an even layer, (c) a mask is applied over the resist and exposed, (d) the design is developed with MF-319 developer, (e) using ion beam sputtering, an adhesive layer of chrome is applied followed by a layer of platinum, (f) the excess metal film is removed by sonicating the substrate in acetone.

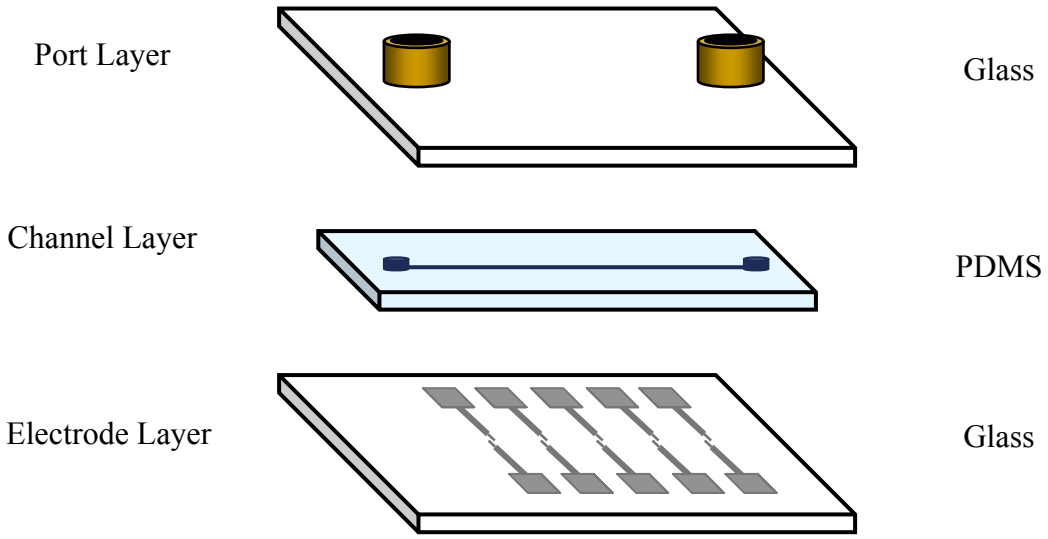

Figure 2-3: An exploded diagram of the PDMS "sandwich" chip. The PDMS layer containing the molded channel is bound between the electrode substrate and a glass cover plate, to which is applied surface-mounted ports for fluid flow.

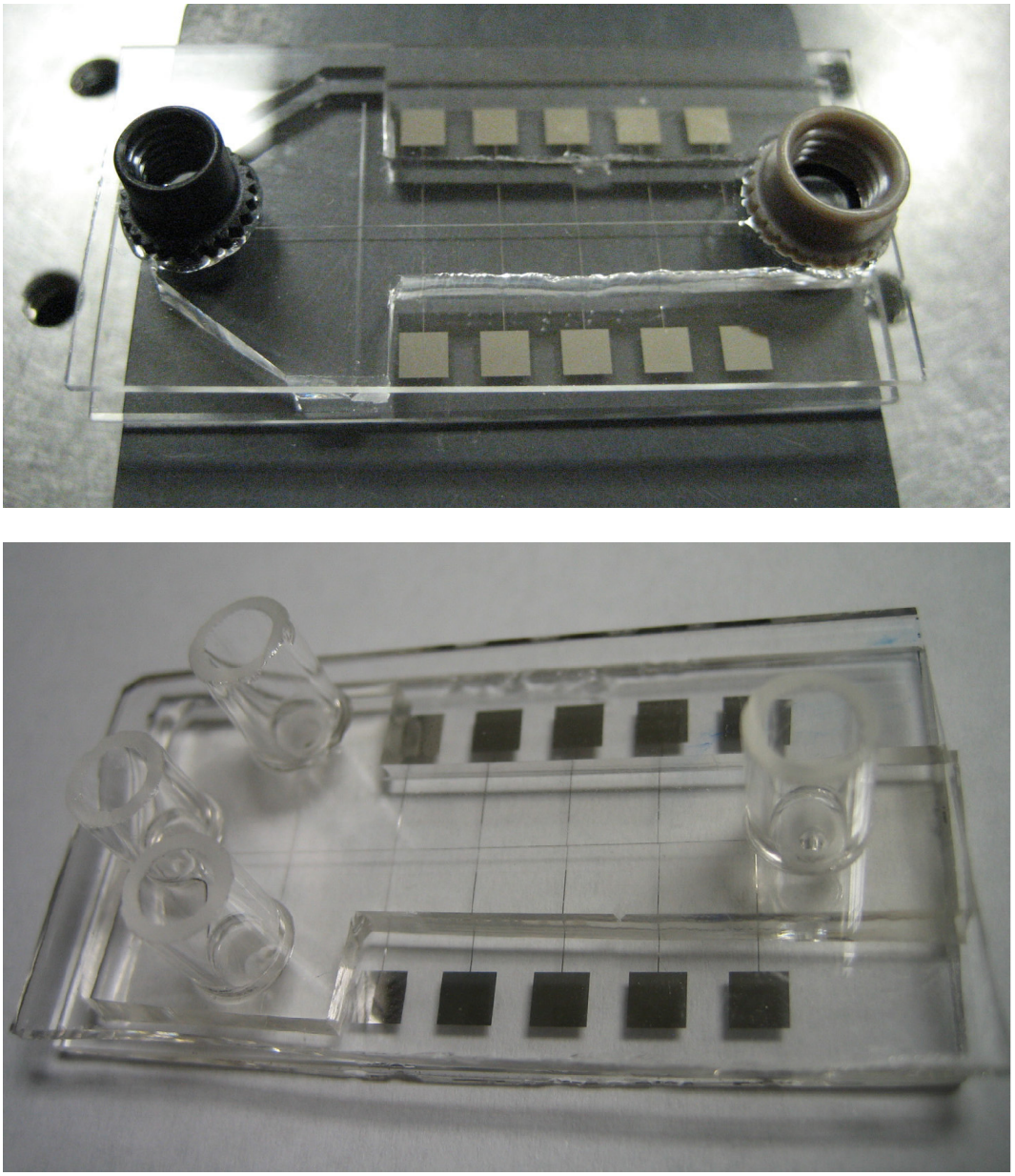

Figure 2-4: Assembled PDMS "sandwich" chips for pressure driven (top) and electrokinetic (bottom) fluid flow.

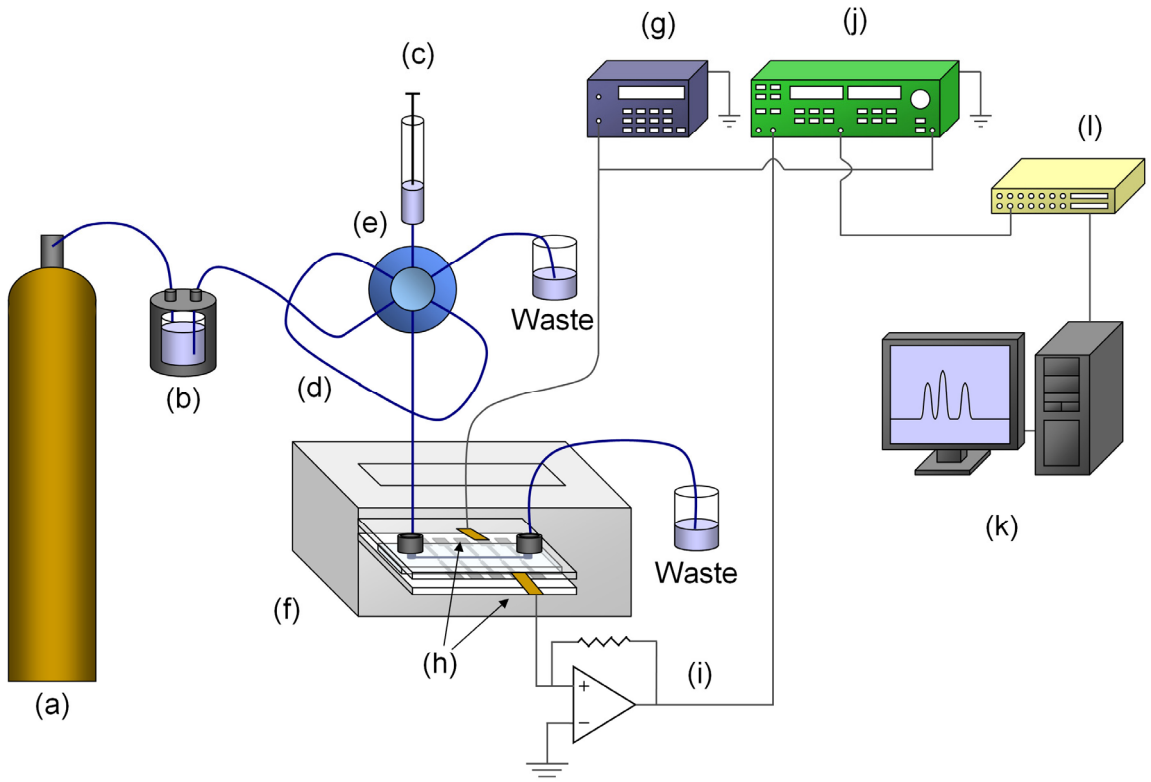

Figure 2-5: Schematic diagram of the setup for the pressure driven conductivity "sandwich" chip. Pressure to drive fluid flow is provided by a helium gas (a), fed into a pressure bomb containing the running buffer (b). Sample is injected with a syringe (c) into the sample loop (d) of a six-port valve (e). Once injected, the sample is forced into the conductivity chip, which is housed in a shielding metal box (f). Signal to the conductivity detector is supplied by the function generator (g) via clamps to one of the chip's electrodes (h). A second clamp is applied to the corresponding detection electrode to feed signal to a current-to-voltage amplifier with 10^6 gain (i). The signal is filtered by the lock-in amplifier (j) and recorded with a computer (k) through a data acquisition board (l).

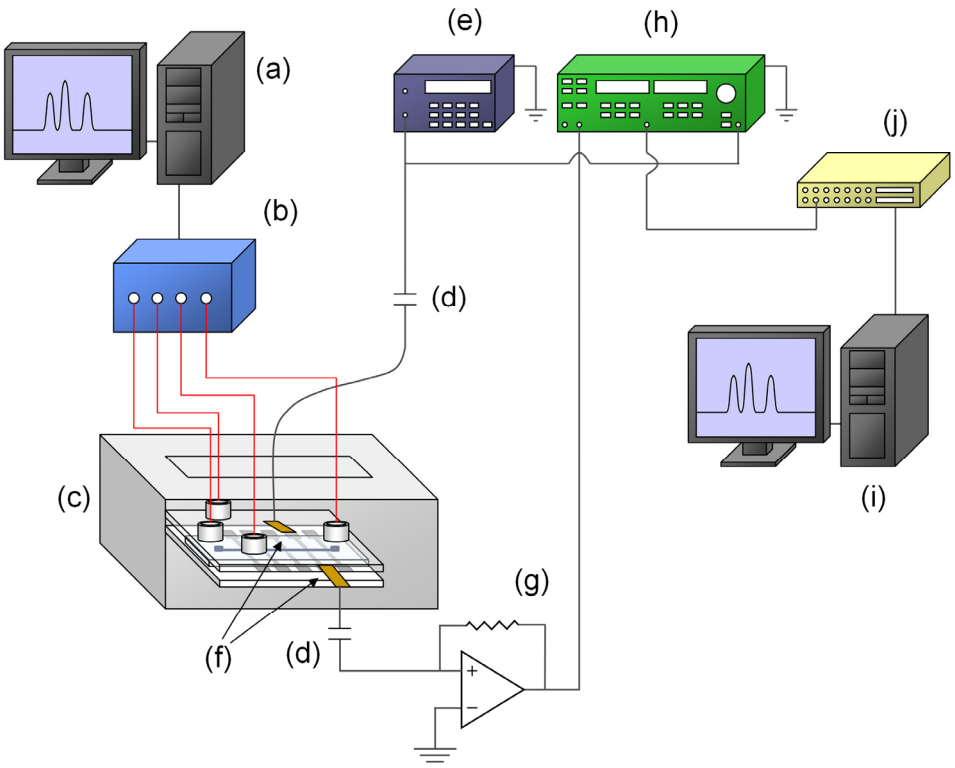

Figure 2-6: Schematic diagram of the setup for the electrokinetically driven conductivity "sandwich" chip. Electrophoresis is driven by a computer (a) controlled high voltage power supply (b). The conductivity chip is housed in a shielding metal box (c). High voltage 100pf capacitors (d) are used to isolate the detection electronics from the electrophoresis voltage. Signal to the conductivity detector is supplied by the function generator (e) via clamps to one of the chip's electrodes (f). A second clamp is applied to the corresponding detection electrode to feed signal to a current-to-voltage amplifier with 10^6 gain (g). The signal is filtered by the lock-in amplifier (h) and recorded with a second computer (i) through a data acquisition board (j).

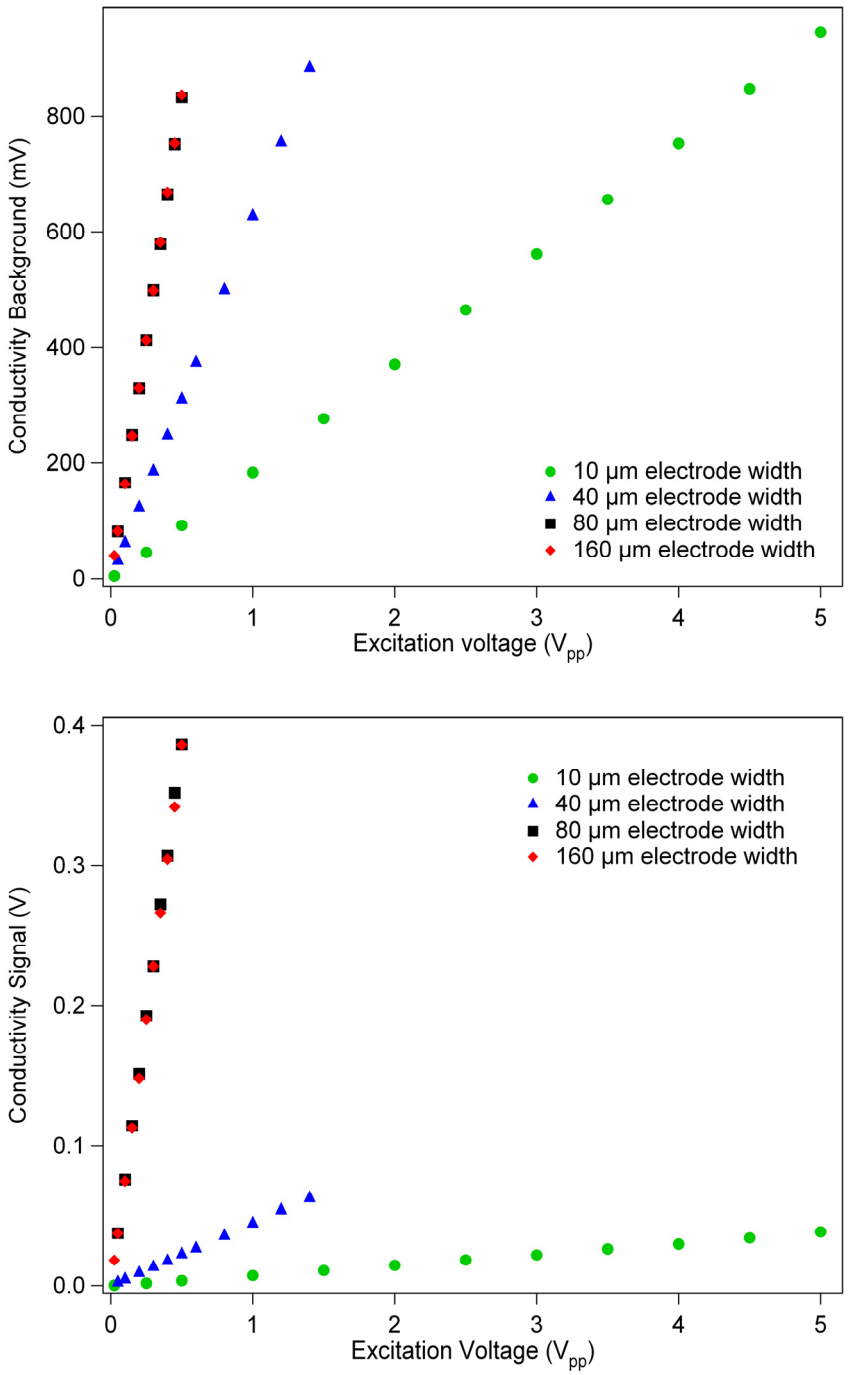

Figure 2-7: Background conductivity (top) and conductivity signal of a front of 50 ppm Na^+ (bottom) taken at increasing excitation voltages for varying electrodes widths. The excitation frequency was set at 100 kHz. Helium back pressure was 11.5 psi, and all values were taken with a running buffer of 20 mM MES/His.

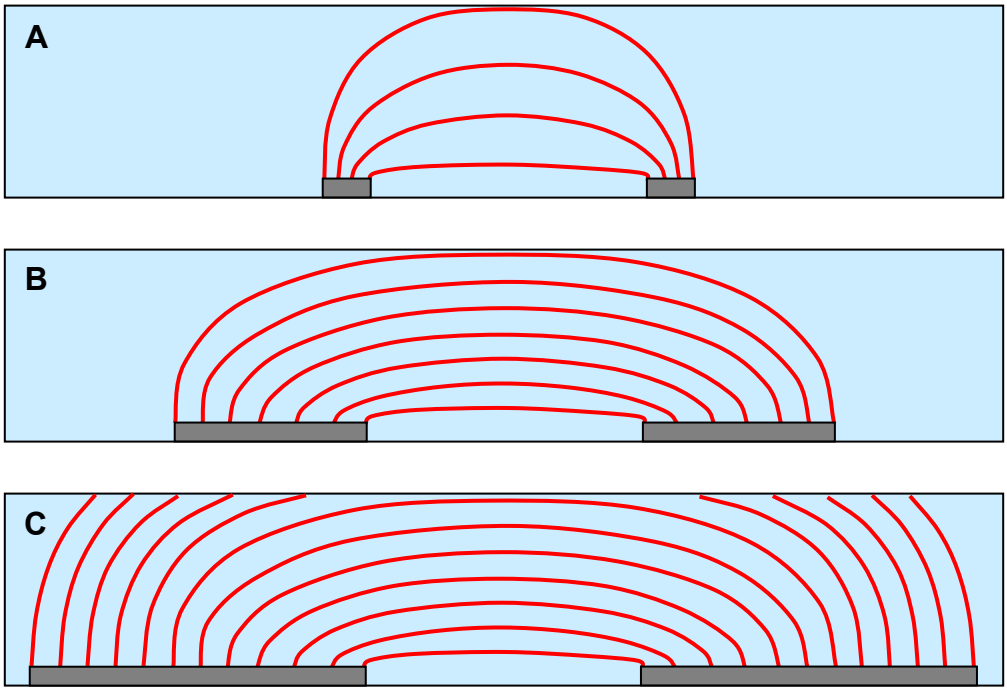

Figure 2-8: Diagrams of the axial cross section of the detection regions and electric field lines when (A) the electrode width is narrower than the channel width, (B) the electrode width is the same as the channel depth, and (C) the electrode width is wider than the channel depth.

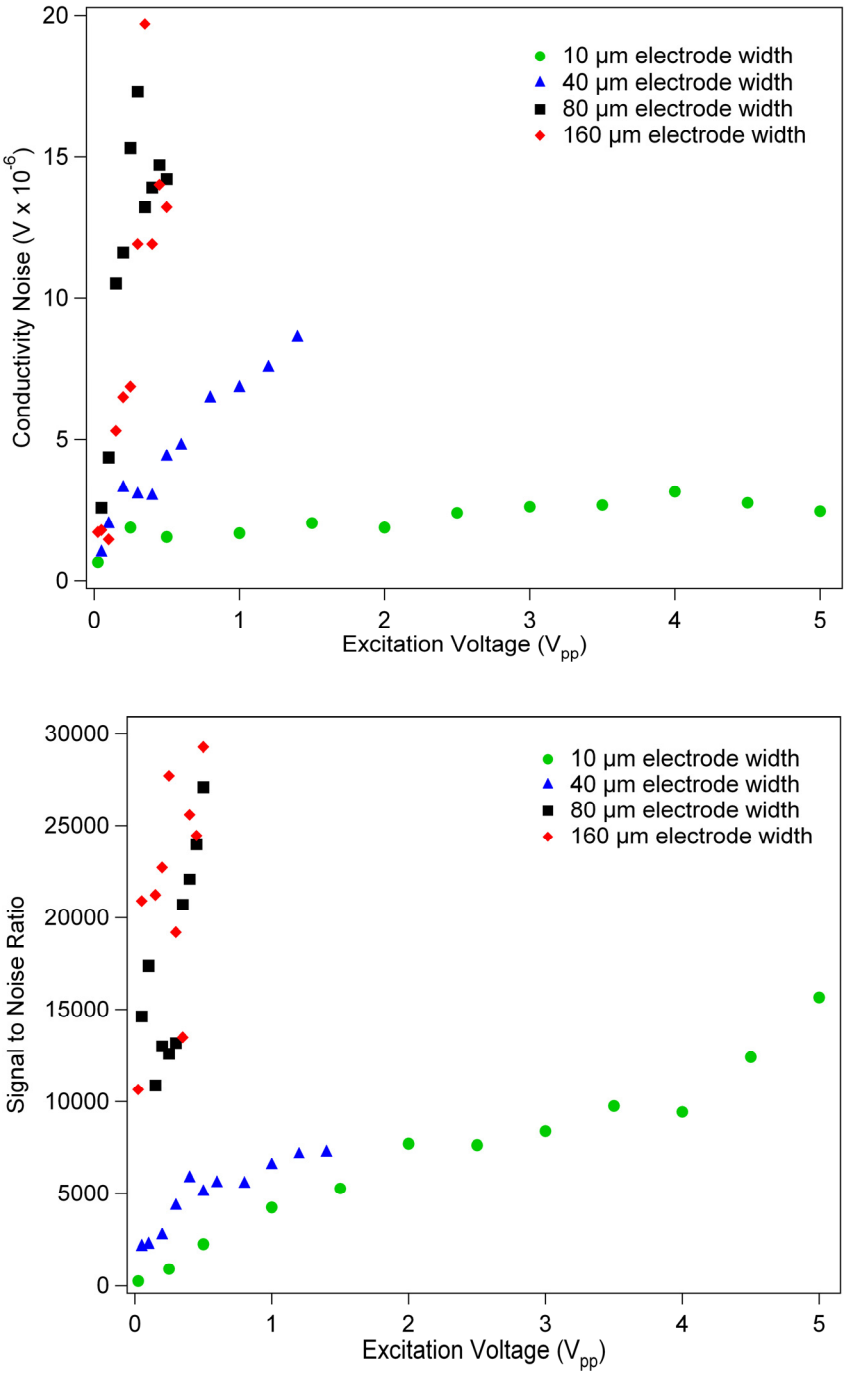

Figure 2-9: The conductivity noise (top) and signal to noise ratio of a front of 50 ppm Na^+ (bottom) taken at increasing excitation voltages for varying electrodes widths. The excitation frequency was set at 100 kHz. Helium back pressure was 11.5 psi, and all values were taken with a running buffer of 20 mM MES/His

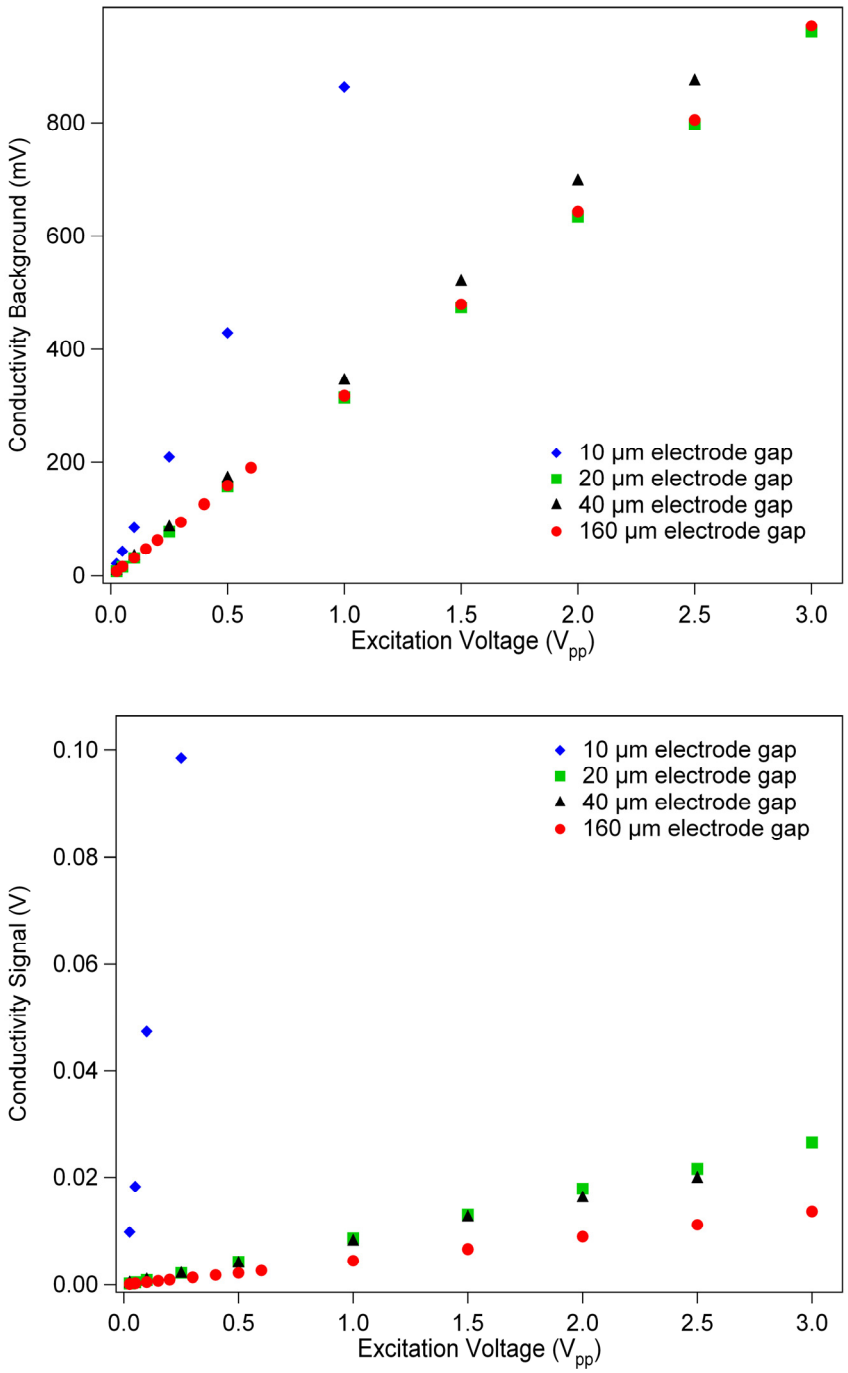

Figure 2-10: Background conductivity (top) and conductivity signal of a front of 50 ppm Na^+ (bottom) taken at increasing excitation voltages for electrodes with varying gap widths. The excitation frequency was set at 100 kHz. Helium back pressure was 11.5 psi, and all values were taken with a running buffer of 20 mM MES/His.

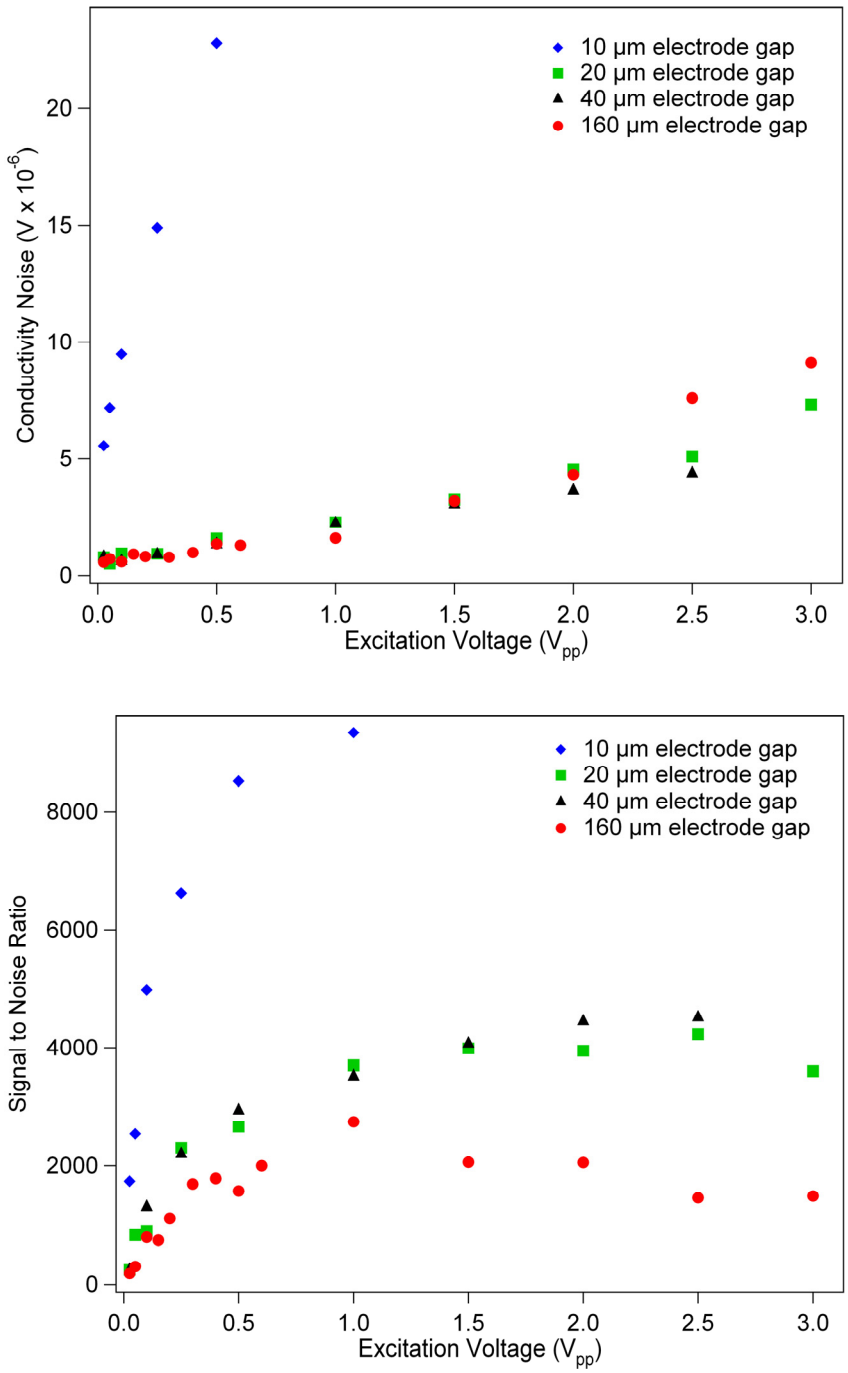

Figure 2-11: The conductivity noise (top) and signal to noise ratio of a front of 50 ppm Na^+ (bottom) taken at increasing excitation voltages for electrodes with varying gap widths. The excitation frequency was set at 100 kHz. Helium back pressure was 11.5 psi, and all values were taken with a running buffer of 20 mM MES/His.

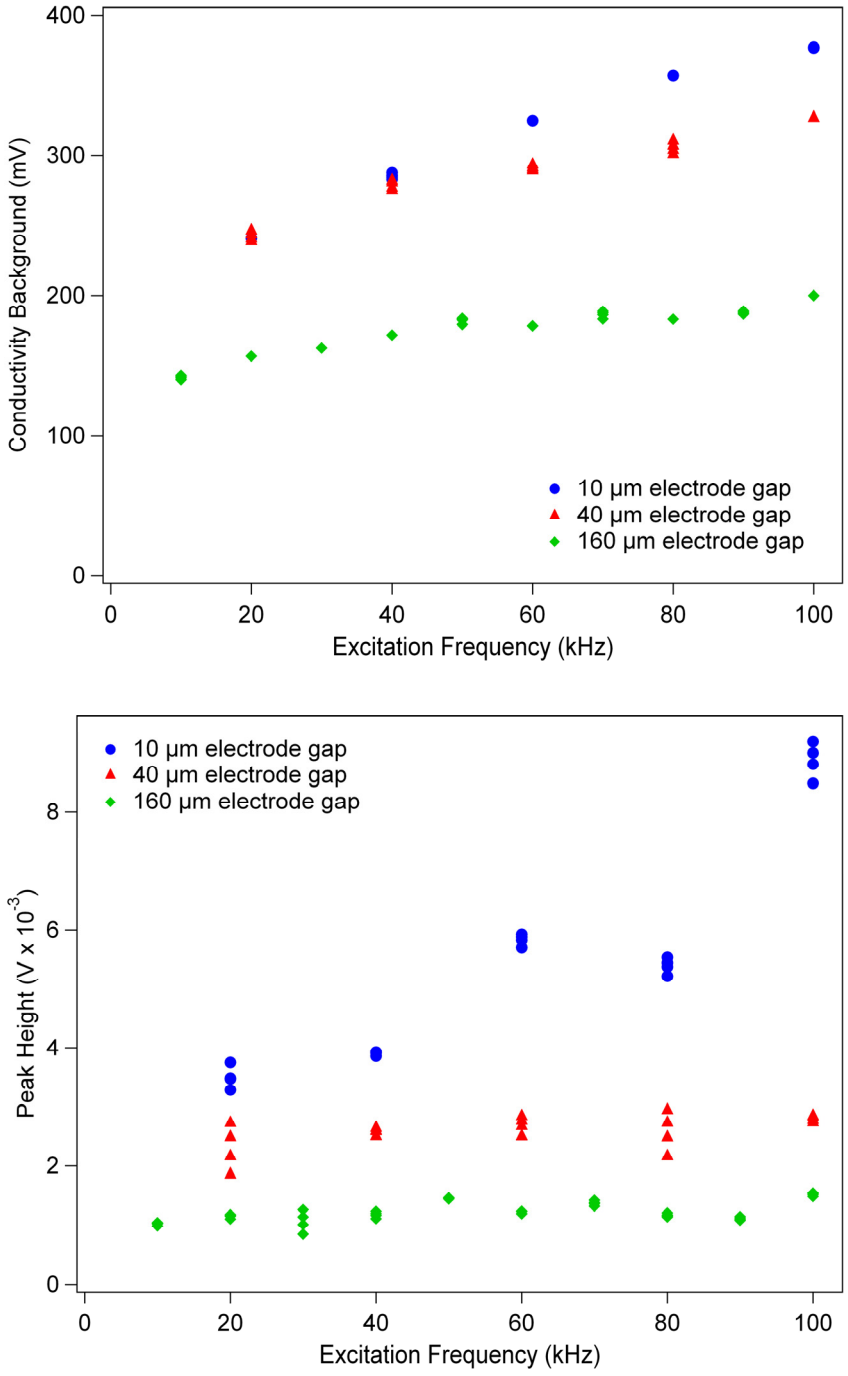

Figure 2-12: Background conductivity (top) and peak height of a 1 s injection of 10 ppm K^+ (bottom) taken at increasing excitation frequencies for electrodes with varying gap widths. The excitation voltage was set at 0.25 V_{pp} and an electric field of 100 V/cm in the separation channel provided the electrokinetic flow. All values were taken with a running buffer of 20 mM MES/His.

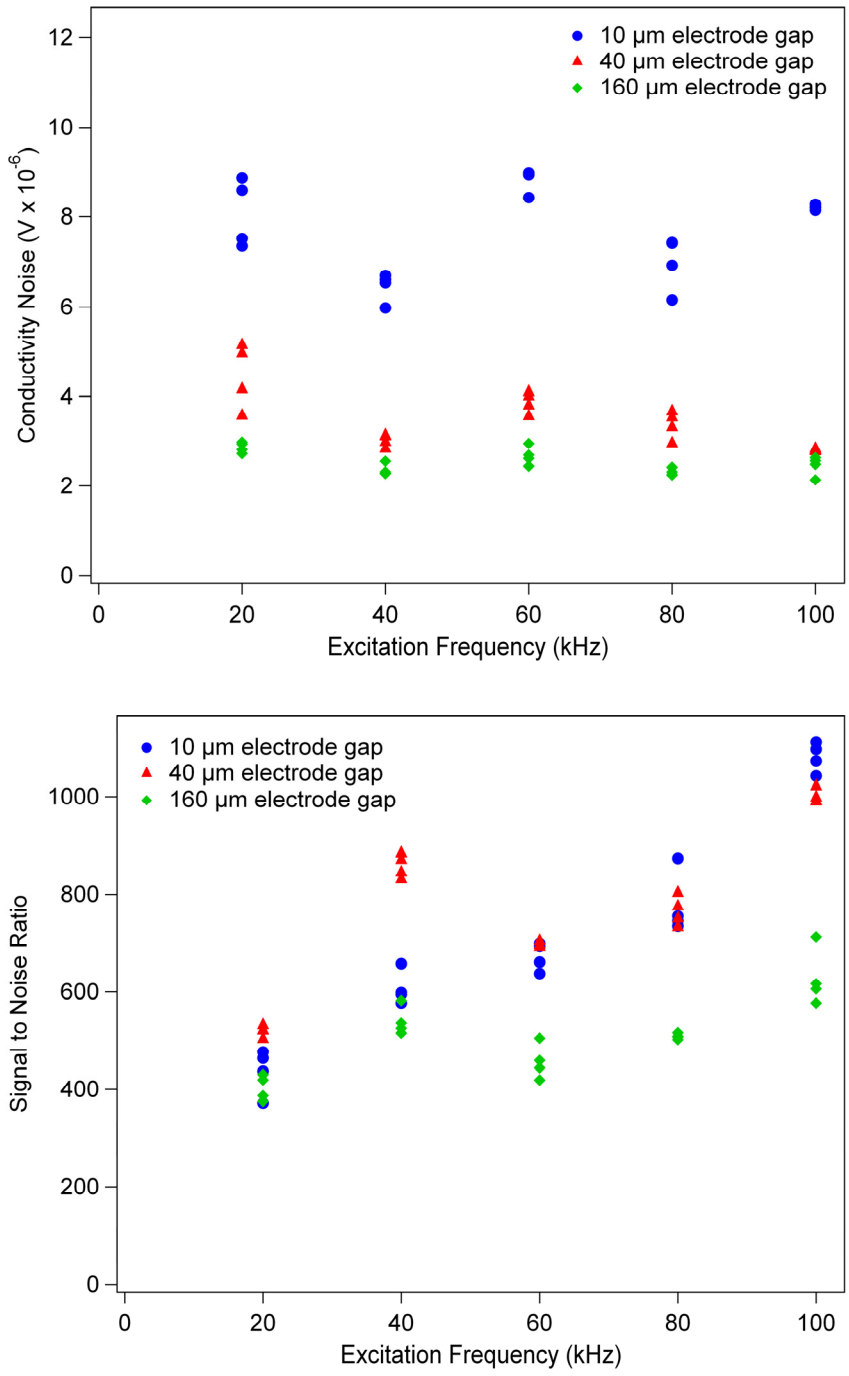

Figure 2-13: The conductivity noise (top) and signal to noise ratio of a 1 s injection of 10 ppm K^+ (bottom) taken at increasing excitation frequencies for electrodes with varying gap widths. The excitation voltage was set at 0.25 V_{pp} and an electric field of 100 V/cm in the separation channel provided the electrokinetic flow. All values were taken with a running buffer of 20 mM MES/His.

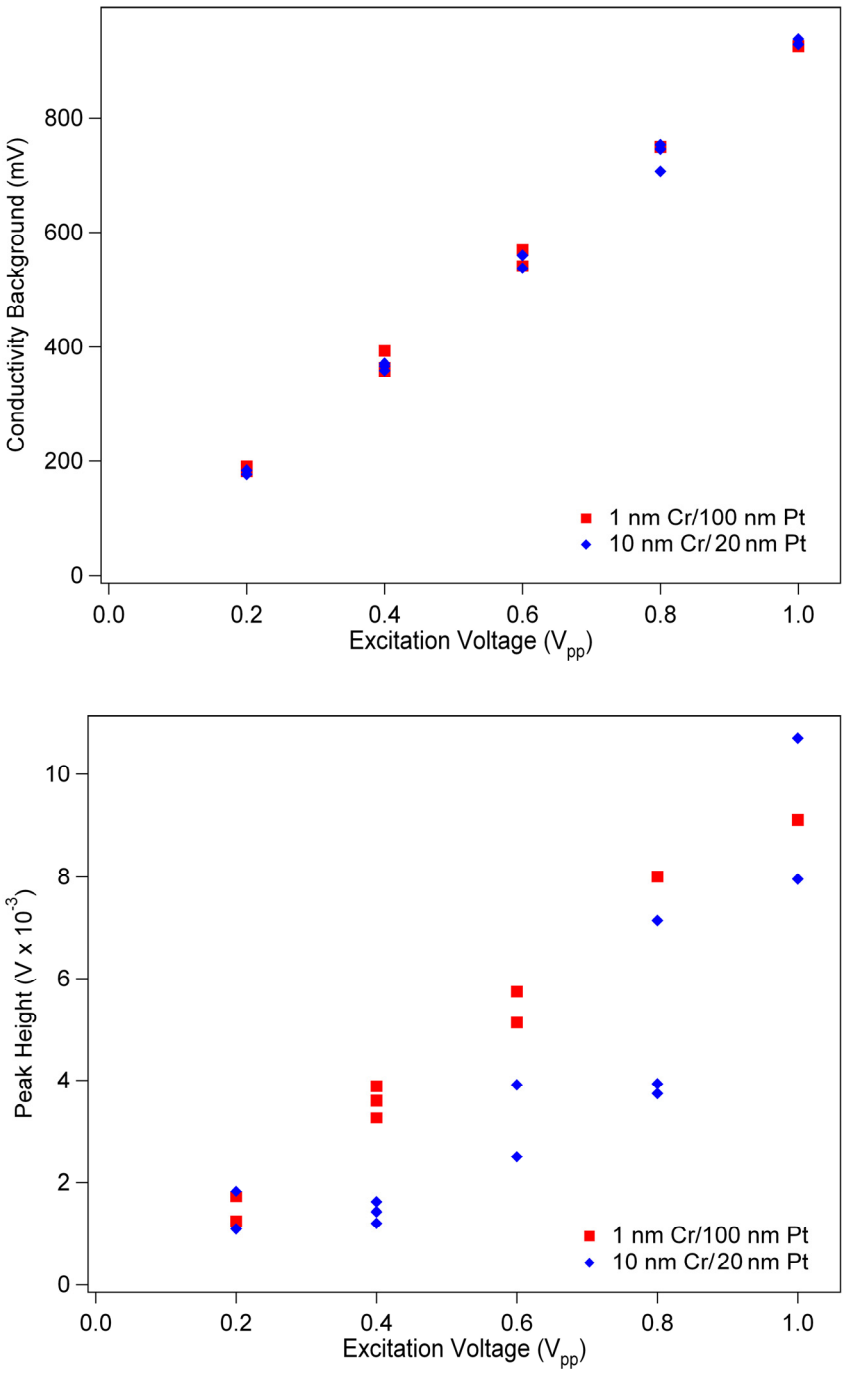

Figure 2-14: Background conductivity (top) and peak height of a 1 s injection of 50 ppm Na^+ (bottom) taken at increasing excitation voltages for electrodes with different metal film thickness. The excitation frequency was 100 kHz and an electric field of 100 V/cm in the separation channel provided the electrokinetic flow. All values were taken with a running buffer of 20 mM MES/His.

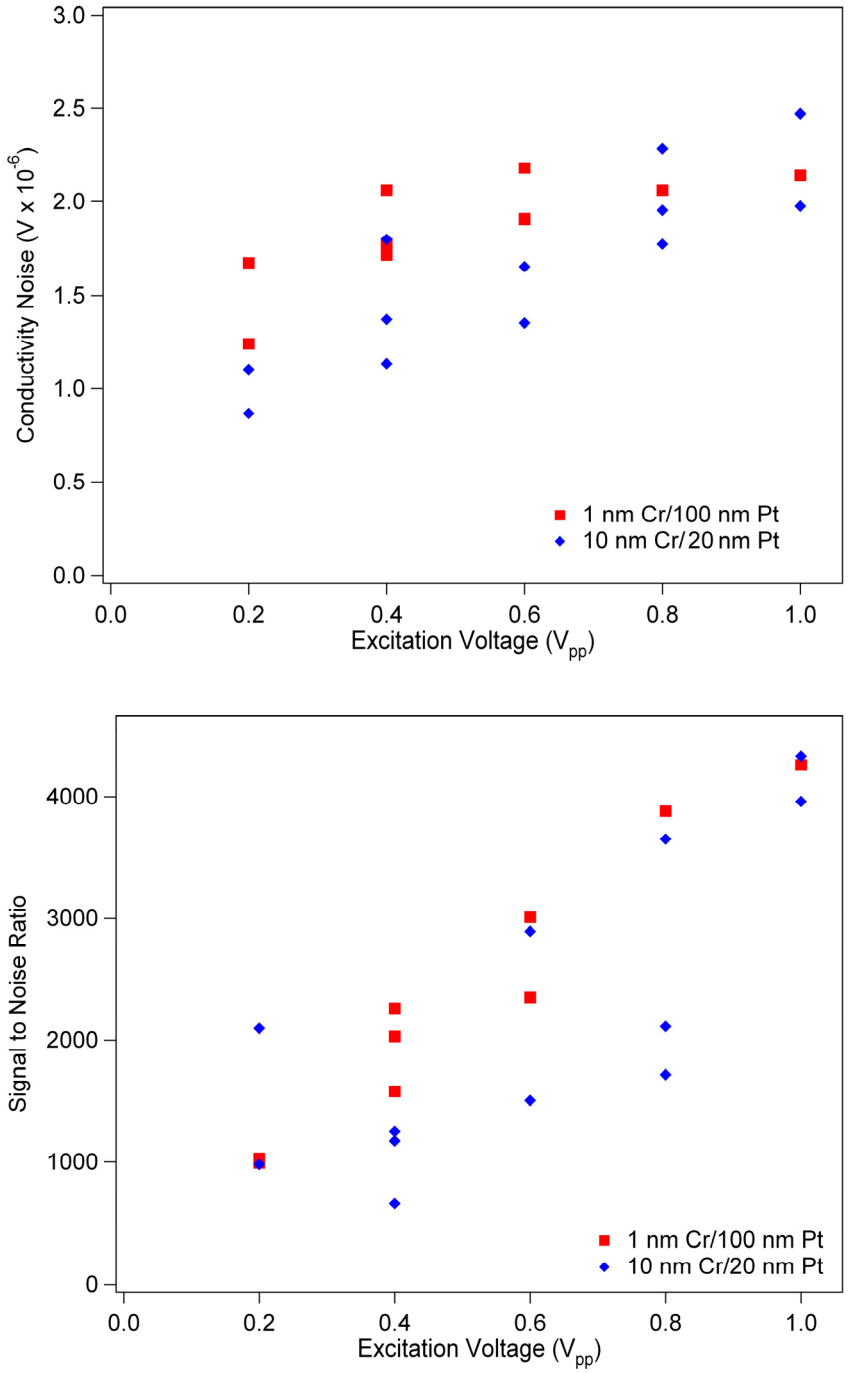

Figure 2-15: Conductivity noise (top) and signal to noise ratio of a 1 s injection of 50 ppm Na^+ (bottom) taken at increasing excitation voltages for electrodes with different metal film thickness. The excitation frequency was 100 kHz and an electric field of 100 V/cm in the separation channel provided the electrokinetic flow. All values were taken with a running buffer of 20 mM MES/His.

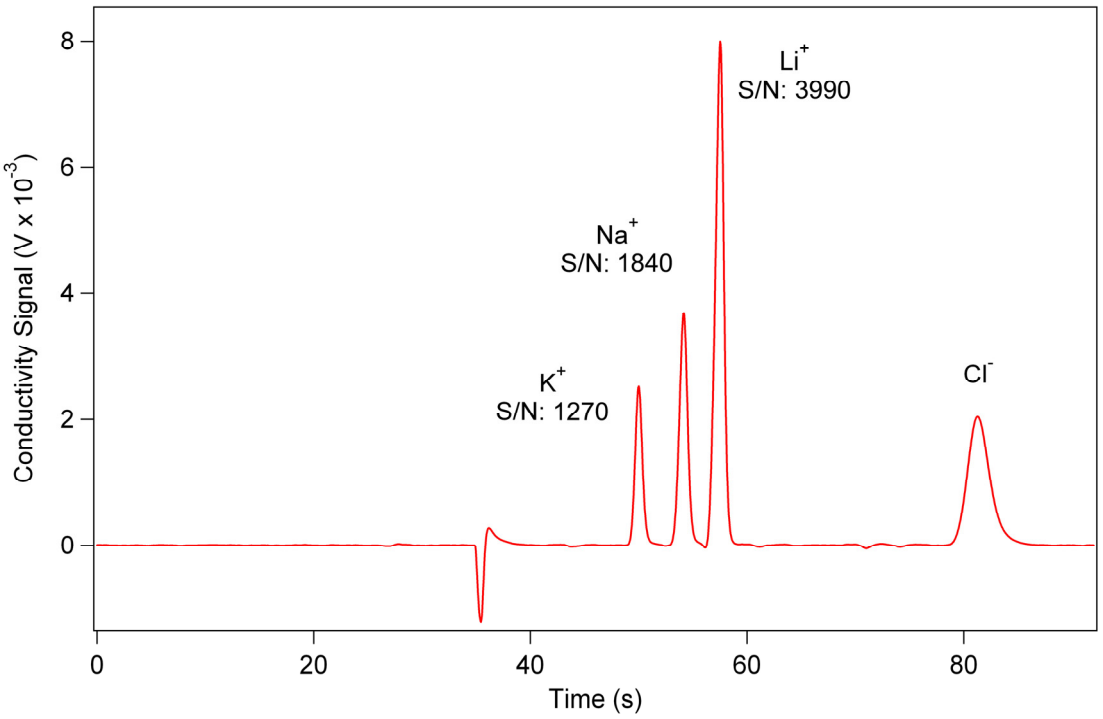

Figure 2-16: Separation of a 1 s injection of a mixture of chloride salts, potassium, sodium and lithium, in a running buffer of 20 mM MES/His. The downward spike at 33 s indicates the dead time. The excitation signal was a 0.25 V_{pp} 100 kHz sine wave. The separation was performed using the PDMS sandwich chip with 20 µm wide 40 µm gap detection electrodes under a 150 V/cm electric field.

2.6 References

(1) Dennis, P. J. *Advancements and Applications of Ionic Conductivity Detection to Microcolumn and Microfluidic Separations*; Doctoral Dissertation, University of North Carolina at Chapel Hill, 2007.

(2) Fadgen, K. E. *Advancements in Detection for Micocolumn Separations*; Doctoral Dissertation, University of North Carolina at Chapel Hill, 2001.

(3) Johnston, S. E. *Applications of Conductivity Detection in Microcolumn Separations*; Doctoral Dissertation, University of North Carolina at Chapel Hill, 2005.

(4) Guijt, R. M.; Evenhuis, C. J.; Macka, M.; Haddad, P. R. *Electrophoresis* **2004**, *25*, 4032–4057.

(5) Benedikt Grass, D. S., Andreas Neyer, Roland Hergenröder *Fresenius Journal of Analytical Chemistry* **2001**, *371*, 228–233.

(6) Berthold, A.; Laugere, F.; Schellevis, H.; Boer, C. R. d.; Laros, M.; Guijt, R. M.; Sarro, P. M.; Vellekoop, M. J. *Electrophoresis* **2002**, *23*, 3511–3519.

(7) Grass, B.; Neyer, A.; Johnck, M.; Siepe, D.; Eisenbeiss, F.; Weber, G.; Hergenrodera, R. *Sensors and Actuators B* **2001**, *72*, 249-258.

(8) Guijt, R. M.; Baltussen, E.; Steen, G. v. d.; Frank, H.; Billiet, H.; Schalkhammer, T.; Laugere, F.; Vellekoop, M.; Berthold, A.; Sarro, L.; van Dedem, G. W. K. *Electrophoresis* **2001**, *22*, 2537–2541.

(9) Guijt, R. M.; Baltussen, E.; Steen, G. v. d.; Schasfoort, R. B. M.; Schlautmann, S.; Billiet, H. A. H.; Frank, J.; Dedem, G. W. K. v.; van den Berg, A. *Electrophoresis* **2001**, *22*, 235-241.

(10) Jeff E. Prest, S. J. B., Peter R. Fielden, Nicholas J. Goddard and Bernard J.; Brown, T. *The Analyst* **2002**, *127*, 1413–1419.

(11) Joseph Wang, G. C., Alexander Muck, Jr. *Analytical Chemistry* **2003**, *75*, 4475-4479.

(12) Joseph Wang, M. P., Greg E. Collins, and Ashok Mulchandani *Analytical Chemistry* **2002**, *74*, 6121-6125.

(13) Kubán, P.; Hauser, P. C. *Electrophoresis* **2005**, *26*, 3169–3178.

(14) Kuban, P.; Hauserb, P. C. *Analytica Chimica Acta* **2008**, *607*, 15-29.

(15) Laugere, F.; Guijt, R. M.; Bastemeijer, J.; van der Steen, G.; Berthold, A.; Baltussen, E.; Sarro, P.; van Dedem, G. W. K.; Vellekoop, M.; Bossche, A. *Analytical Chemistry* **2003**, *75*, 306-312.

(16) Law, W. S.; Kubán, P.; Zhao, J. H.; Li, S. F. Y.; Hauser, P. C. *Electrophoresis* **2005**, *26*, 4648–4655.

(17) Lee, C.-Y.; Chen, C. M.; Chang, G.-L.; Lin, C.-H.; Fu, L.-M. *Electrophoresis* **2006**, *27*, 5043–5050.

(18) Lichtenberg, J.; de Rooij, N. F.; Verpoorte, E. *Electrophoresis* **2002**, *23*, 3769–3780.

(19) Liu, Y.; Wipf, D. O.; Henry, C. S. *The Analyst* **2001**, 1248-1251.

(20) Michelle Galloway, S. A. S. *Electrophoresis* **2002**, *23*, 3760–3768.

(21) Michelle Galloway, W. S., Alyssa Henry, Sean M. Ford, Shawn Llopis,; Robin L. McCarley, a. S. A. S. *Analytical Chemistry* **2002**, *74*, 2407-2415.

(22) Prest, J. E.; Baldock, S. J.; Bektas, N.; Fielden, P. R.; Treves Brown, B. J. *Journal of Chromatography A* **1999**, *836*, 59-65.

(23) Prest, J. E.; Baldock, S. J.; Fielden, P. R.; Treves Brown, B. J. *The Analyst* **2001**, *126*, 433-437.

(24) Pumera, M.; Wang, J.; Opekar, F.; Jelinek, I.; Feldman, J.; Lowe, H.; Hardt, S. *Analytical Chemistry* **2002**, *74*, 1968-1971.

(25) Zemann, A. J.; Schnell, E.; Volgger, D.; Bonn, G. K. *Analytical Chemistry* **1998**, *70*, 563-567.

(26) Baldock, S. J.; Bektas, N.; Fielden, P. R.; Goddard, N. J.; Pickering, L. W.; Prest, J. E.; Snook, R. D.; Brown, B. J. T.; Vaireanu, D. I.; Harrison, D. J.; van den Berg, A. *Micro Total Analysis Systems 1998* **1998**, 359.

(27) Jeff E. Prest, S. J. B., Peter R. Fielden, Nicholas J. Goddard and Bernard J. Treves Brown *The Analyst* **2003**, *128*, 1131–1136.

(28) Jacobson, S. C.; Koutny, L. B.; Hergenroder, R.; Moore, A. W.; Ramsey, J. M. *Analytical Chemistry* **1994**, *66*, 3472-3476.

(29) Madou, M. J. *Fundamentals of Microfabrication*; CRC Press: Washington, DC, 2002.

Chapter 3: Photothermal Absorbance Detection on a Microfluidic Device

3.1 Introduction

Conductivity based photothermal absorbance detection, as was described in Chapter 1, was initially performed with capillary electrophoresis and capacitively coupled contactless conductivity detection (C^4D). The detector consisted of three cylindrical electrodes, the outer two to apply the excitation potential and the center to detect the conductivity response. A laser beam focused between the first two electrodes was used as the light source for absorption. Experimentation and simulation results found that this detection scheme, while promising, was inadequate for low analyte concentration detection compared to commercially available UV/visible detectors. This insensitivity was caused by the large electrodes and electrode spacing necessary for effective capacitive coupling. The large size disparity between the electrodes and the region heated by the laser spot caused photothermal signal reduction and the decreased sensitivity.[1-5]

Simulations indicated that reducing the detection region size to the same order of magnitude as the heated region would greatly increase the sensitivity. One approach to accomplish this was to transfer the system to a microfluidic platform. The fabrication methods used to create microfluidic devices can manufacture micrometer-scale, solution-contacting electrodes for increased sensitivity.[6] Following validation and characterization of the PDMS "sandwich" chip conductivity detector discussed in Chapter 2, the next step was to apply it to conductivity based photothermal detection. Initial photothermal studies were

completed using a chip with a 75 μm x 75 μm molded PDMS channel and electrodes composed of 30 nm chrome and 60 nm platinum that were 20 μm wide with a gap size of 80 μm. Helium pressure was used to drive the fluid flow, and the 50 μM 4-(dimethylamino) azobenzene-4'-sulfonyl (DABSYL) tagged glucosamine was used ad the analyte. The PDMS "sandwich" chip in this system followed the expected trends when varying the excitation signal and optical excitation, and a detection limit of 150 nM was obtained. This limit of detection far exceeded any observations using the capillary system.[1]

Despite the successful photothermal detection on PDMS chips, the elasticity of PDMS presents a problem. PDMS has a tendency to swell or contract depending on the composition of the running buffer, and temperature change from the incident laser light could affect the shape of the detection region. Such changes in the detection region geometry results in reduced reproducibility and sensitivity. The hydrophobic nature of PDMS also required further surface modification to be useful for electrokinetic separations, and composite devices made of glass and PDMS can have flow patterns that are difficult to characterize.[7]

As the ultimate goal is photothermal detection using a UV wavelength, fused silica or quartz substrates would be preferred over borosilicate glass or PDMS. To reach this point, fabrication issues that need to be addressed include electrode development and substrate bonding while maintaining electrode integrity. There are multiple examples of microfabricated conductivity detectors in the literature that make use of glass or fused silica substrates. A few of these, including Lichtenberg et al.[8] and Laugere et al.,[9] were discussed previously in Chapter 2. While these examples used contactless conductivity detection, the electrode fabrication procedure, in which the electrodes were created in etched trenches,

could easily be applied to a contact conductivity detector. These embedded electrodes would allow good contact between two planar glass substrates during the bonding process.[6,10,11] However, when bonding, quartz requires higher temperatures than B270 white crown or other glasses, and platinum films have been found to degrade at temperatures above 700°C.[12]

Also of interest was the characterization of a new type of electrode. Polyelectrolyte salt bridge electrodes (PSBE) were reported by Chun et al.[13,14] and are composed of an ionic polymer network where movement of charge much like a traditional salt bridge occurs. Excitation potentials can be applied to the "electrodes" through reservoirs filled with a salt solution. One advantage of PSBEs over standard metal electrodes is that they are not susceptible to electrolysis caused by the high voltages necessary for electrokinetic flow. Characterization and comparison of the two types of electrodes, as well as further modifications to the microchip designs, will be discussed.

3.2 Experimental

3.2.1 Materials

Materials were used as received without further modification. Sodium hydroxide (NaOH) solution, lithium chloride (LiCl), and sodium chloride (NaCl) were obtained from Fisher Scientific (Fair Lawn, NJ). Potassium chloride (KCl) was obtained from Mallinckrodt (Paris, NY). 2-morpholinoethansulfonic acid (MES) and L-histidine (His) were purchased from Sigma (St. Louis, MO). All buffers and solutions were prepared with water from a Barnstead Nanopure Filtration System (Boston, MA). The standard electrophoresis running buffer was a solution of 20 mM MES and 20 mM His adjusted to pH 6.1. All solutions were further filtered with a 0.2 μm nylon membrane filter (Whatman, Brentford, Middlesex, UK)

before injection into the system. Glucosamine and 4-(dimethylamino)azobenzene-4'-sulfonyl (DABSYL) chloride were obtained from Supelco (St. Louis, MO). DABSYL tagged glycine, proline, and tryptophan were obtained from Anaspec (San Jose, CA).

Quartz substrates used for device fabrication were 4 in x 4 in x 2.2 mm (l x w x h) grade CG wafers coated with a 1200 Å low reflectivity chrome layer and a 5300 Å layer of AZ 1518 photoresist (Telic, Valencia, CA). Also used were 4 in x 4 in x 0.9 mm white crown (B-270) glass grade PG wafers coated with 1200 Å film of low reflectivity chrome and 5300 Å of AZ 1518 photoresist (Telic, Valencia, CA).

Diallyldimethylammonium chloride (DADMAC), N,N'-methylene-bisacrylamide, 2-hydroxy-4'-(2-hydroxyethoxy)-2-methylpropiophenone, and 3-(trimethoxysilyl)propyl methacrylate (TMSMA) were purchased from Sigma-Aldrich (St. Louis, MO) and used to fabricate the polyelectrolyte salt bridge electrodes (PSBEs). Glacial acetic acid, ethanol and acetonitrile were obtained from Fisher Scientific (Fair Lawn, NJ).

3.2.2 Preparation of DABSYL-tagged Glucosamine

The procedure for tagging glucosamine with DABSYL has been described previously.[15] Equal volumes of 6mM DABSYL chloride in filtered acetone and 1 mM glucosamine in 50 mM carbonate buffer (at pH 9.0) were prepared and mixed in a round bottom flask. The flask was sealed with a stopper and placed in a water bath at 75º. The reaction proceeded to completion within 12 minutes. The solution was then cooled to room temperature before immersing the flask into liquid nitrogen and freezing the solution. After removing the flask from the liquid nitrogen, it was placed at room temperature into a vacuum chamber and the solvent was removed by lyophilization over the course of 4 to 12 hours,

resulting in a fine powder. This powder was freed of any remaining carbonate by mixing the powder in deionized water, sonicating for 10 minutes, and centrifugation at 10,000 rpm for 15 minutes. The supernatant was removed and set aside, and the remaining solid was collected and mixed in deionized water. This process was repeated at least 4 to 5 times. The cleaned solids were collected and dissolved in deionized water to give the final product.

3.2.3 Microchip Fabrication

3.2.3.1 Metal Electrode Fused Silica Microchip

The top substrate was etched with the channels used for fluid control. The chips were made from photoresist/chrome coated quartz plates (Telic, Valencia, CA), which was cut into 1 in x 2 in substrates using a Basic Dicer II (Dicing Technology, Longwood, FL). A photomask with the channel layout was designed using TurboCAD v. 9.2 Student Edition (Novato, CA). The completed designs were sent to The Photoplot Store (Colorado Springs, CO) for printing on a mylar film base with an Accumax ARD7 emulsion layer photoplotter (Kodak, Rochester, NY). The mask was placed emulsion side down directly onto the substrate surface, and a 4 in x 4 in quartz blank was placed over it to ensure good contact between the two. The photoresist was exposed through UV flood exposure with a J200 UV Exposure System (OAI, Milpitas, CA) for 65-75 seconds. Following exposure, the coated substrate was immersed in MF-319 developer (Microchem Corp., Marlboro, MA) for 45-60 seconds to remove the exposed areas. The substrate was removed from the developer, rinsed with deionized water, and dried with pressurized nitrogen gas. The design was then observed under an optical microscope to ensure complete development. The chrome in the exposed areas was removed using chrome etchant (Transene, Danvers, MA) for 5-10 minutes. The

substrate was then rinsed with deionized water, cleaned with 2% sulfuric acid, rinsed again with deionized water, and dried with pressurized nitrogen gas.

The channels were etched isotropically into the quartz substrate using 5:1 buffered oxide etchant (Transene, Danvers, MA). Throughout the etching process, the channel depth was monitored using a P-15 profilometer (KLA Tencor, San Jose, CA). The etching process was halted before each check by rinsing in deionized water, cleaning with 2% sulfuric acid to remove residue from the channel surface, rinsing again with deionized water, and drying with pressurized nitrogen gas. Upon reaching the desired depth, the substrate was coated with a thick layer of S1813 photoresist to protect the etched channels. Access holes were drilled at the end of each channel segment using a MB 1000-1 powder blaster (Comco, Inc., Burbank, CA) set to make holes 1-2 mm in diameter. The powder blaster was also used to cut away excess substrate to provide access to the electrode pads. The photoresist was then removed with acetone, and the remaining chrome mask was removed with chrome etchant.

The metal film electrodes were fabricated using the same procedure outlined in Chapter 2 for the PDMS sandwich chip. Chromium (Cr) and platinum (Pt) thickness was dependent on the experimental parameters. For some of these electrodes, an additional etching step was added prior to sputtering metal film. The resulting electrodes were flush with the substrate surface. For all photothermal chips, electrodes were 50 μm wide and arranged in a three-electrode, anti-parallel geometry.

To prepare for bonding, the completed microchip halves were immersed in Nanostrip 2x (Cyantek Corperation, Fremont, CA) for up to 15 min in order to remove any remaining organic residue on the surfaces. After rinsing with deionized water, the substrates were sonicated in a 2% Contrad 70 solution for 10 minutes, removed, and rinsed. A hydrolysis

bath composed of two parts water, two parts 30% ammonium hydroxide, and one part 30% hydrogen peroxide was prepared and heated to 65-70°C. The substrates were immersed in the hydrolysis bath for 10-15 minutes to activate the quartz surfaces. They were then rinsed with deionized water and sonicated for an additional 10 minutes. After removing from sonication, the electrode substrate was held face up, and deionized water was pooled over its surface. The channel substrate was laid over the electrodes, and the excess water was removed by vacuum. The channel and electrodes were carefully aligned under an optical microscope, and the substrates were clamped together. The chip was placed in a convection oven set to 95°C to evaporate the remaining water. After 5 minutes, the chip was removed from the oven and examined for good contact around the microfabricated features. Poorly bonded areas are evident through the appearance of interference patterns. If good bonding was observed, the chip was placed back into the 95° oven for an additional 10-20 minutes. The device was then placed into a furnace (Lindberg/Blue, Watertown, WI) for the final bake. The furnace program was set to ramp from ambient temperature to 90°C over 10 minutes and hold at 90°C for 2 hours to ensure removal of any remaining water. The temperature then increased to 200°C over 2 hours, held for 1 hour, and ramped to 550°C over 2 hours. The furnace was held at 550°C for 10 hours, after which it was cooled to 95°C over 2 hours. Once bonding was completed, cloning cylinders were applied over the access holes using a UV curable optical adhesive. To prevent fluid leakage through any gaps around the electrodes, a small amount of epoxy was applied at the junction between the electrodes and the channel substrate. Images of the completed metal electrode microchip are shown in Figure 3-1.

3.2.3.2 Polyelectrolyte Salt Bridge Electrode (PSBE) Microchips

The PSBE microchips were designed, developed, and fabricated by Honggu Chun, Ph.D. in the Ramsey research group in the Department of Chemistry at the University of North Carolina at Chapel Hill.

The PSBE microchips were fabricated using B270 white crown glass precoated by Telic (Valencia, CA). A maskless SF100 photoexposure system (Intelligent Micro Patterning, LLC, St. Petersburg, FL) was used to pattern the electrode and channel design. Chip designs were created in TurboCAD, and the total exposure time was 4.5 seconds. Following exposure, the coated substrate was immersed in MF-319 developer (Shipley, Marlboro, MA) for 45-60 seconds to remove the exposed photoresist. The substrate was removed from the developer and rinsed with deionized water and dried with pressurized nitrogen gas. The design was then observed under a microscope to ensure complete development. The chrome in the exposed areas was removed using chrome etchant (Transene, Danvers, MA) for 5-10 minutes. The substrate was then rinsed with deionized water, cleaned with 2% sulfuric acid, rinsed again with deionized water, and dried with pressurized nitrogen gas. The design was isotropically etched using 10:1 buffered oxide etchant (Transene, Danvers, MA), and monitored and cleaned according to the procedure described earlier. The final depth was 12 μm.

The bonding cover plate for the PSBE microchip was a 150 μm thick Corning 2940-245 coverglass (Corning, NY). Access holes to the channels and electrode reservoirs were made with the MB 1000-1 powder blaster (Comco, Inc., Burbank, CA) set to make holes 1 mm in diameter. The two substrates were cleaned and bonded according to the procedure

described previously, except the maximum final bake temperature was 300°C. Cloning cylinders were attached at the access holes with UV curable optical adhesive.

The PSBE electrodes were made according to the procedure described by Chun et al.[13] A 200 μL volume of TMSMA was diluted with 1.2 mL of a 10% glacial acetic acid in water solution and 40 mL of ethanol. The microchip was filled with this solution for 3 minutes, covalently bonding the TMSMA to the glass surface. The solution was removed, and the channels rinsed with ethanol. A solution of 65% DADMAC, 2% 2-hydroxy-4'-(2-hydroxyethoxy)-2-methylpropiophenone, and 2% N,N'-Methylene-methylpropiophenone was prepared in deionized water. The solution was flushed through the channels and the electrode reservoirs. A mask was placed over the chip, exposing the area to be polymerized. Polymerization was induced with a Model B 100 AP 100W Long Wave UV lamp (Black-Ray UVP Inc., San Gabriel, CA) for 4 seconds. The microchip was flushed with a 1 M solution of potassium chloride to remove any remaining DADMAC. Signal was applied to the PSBEs via Ag/AgCl electrodes placed in each electrode reservoir. Images of the PSBE chip are shown in Figure 3-2.

3.2.4 Electronic setup

A diagram of the photothermal system's electrical and optical components is shown in Figure 3-3. The output of two DS345 digital function generators (Stanford Research Systems, Sunnyvale, CA) were applied to the excitation and reference electrodes in order to provide the AC excitation signal. The two function generators were set in a master-slave configuration, using the 10 MHz output of one as the time base of the other. The phase and voltage were adjusted in order to balance the function generators precisely 180° out of phase

with each other, using destructive interference to provide zero background conductivity at the detection electrode. The excitation signal passed through a 3 kV, 100 pF radial disc capacitor (Panasonic-ECG, Secaucus, NJ) prior to and after the detection cell. This isolates the excitation electronics from the DC electrophoresis running voltage. Connections to the electrode pads were made with an aluminum pad connected to a 316 stainless steel compression spring (Small Parts Inc., Miami Lakes, FL), which was soldered to the end of a banana connection in a in-house machined polycarbonate microchip holder. The holder was mounted on an x-y-z translational stage for alignment to the laser beam. Signal from the detection electrode was amplified via an OPA602 operational amplifier (Texas Instruments, Dallas, TX) in a current-to-voltage circuit with a 1 MΩ feedback resistor (Multicomp, Chicago, IL), providing 10^6 V/A gain. Surface mounted 1000 pF capacitors (Newark Electronics, Chicago, IL) added to the circuit removed any high frequency noise from the power supply or feedback loop of the operational amplifier. A grounded aluminum box provided shielding for the electronic circuit. A Model 1301 Power Supply (Global Specialties, New Haven, CT) at ±15 V provided power for the operational amplifier.

Output from the chip was further amplified and filtered with two SR810 digital lock-in amplifiers (Stanford Research Systems, Sunnyvale, CA) arranged in series. The first lock-in amplifier was referenced to the master DS345 function generator and provides the standard conductivity signal for reference purposes. Output from this lock-in was input to the second lock-in amplifier, which is referenced to the "*f*" output of a SR540 optical chopper (Stanford Research Systems, Sunnyvale, CA), and thus the optical modulation frequency. The first lock-in was set at a 1 ms time constant and a 24 dB/octave slope (bandwidth = 78 Hz) with AC coupling, and the second lock-in amplifier was set with a 100 ms time constant

and a 24 dB/octave slope (bandwidth = 0.78 Hz) with DC coupling. Line and 2x line filters were used on both lock-in amplifiers. The sensitivity was set at 1 mV for the first lock-in during all experiments and varied for the second to maximize photothermal sensitivity.

Data collection and control of both the function generators and the lock-in amplifiers were maintained with a USB-6229 DAQ card (National Instruments, Austin, TX) and custom software written in LabVIEW (National Instruments, Austin, TX) on a personal computer. Data analysis was performed using Igor Pro (Wavemetrics, Lake Oswego, OR).

3.2.5 Optical setup

Photothermal excitation was provided by the 488 nm line of an Innova FReD argon ion laser (Coherent, Santa Clara, CA). The continuous wave beam was modulated using a SR540 optical chopper (Stanford Research Systems, Sunnyvale, CA) with a six slot blade for frequencies between 4-400 Hz. The beam was cleaned with a spatial filter consisting of a F5 singlet lens (ThorLabs, Newton, NJ), a 25 μm pinhole (Melles Griot, Albuquerque, NM), and a F2 singlet lens (ThorLabs, Newton, NJ). A mirror with UV enhanced reflective metal coating (ThorLabs, Newton, NJ) was used to direct the beam vertically through a long working distance 40x microscope objective (Olympus, Center Valley, PA). The beam was focused to a spot size of about 12 μm at the microchip's surface. Beam positioning in relation to the microchip electrodes was observed using a PL-A741 machine vision camera (PixeLINK, Ottawa, ON). To provide additional focusing and reduce the laser light intensity, a F/2 fused silica singlet lens (ThorLabs, Newton, NJ) and two neutral density filters (FNQ057 and FNQ065, Melles Griot, Albuquerque, NM) were placed before the camera.

3.2.6 Electrophoresis Setup

An in-house built high voltage power supply with four high voltage output modules (10A12-P4 modules, UltraVolt, Ronkonkoma, NY) was used to initiate electrokinetic flow. Platinum wires were used to apply the voltages to fluid reservoirs and controlled through the analog output of a USB-6229 DAQ board (National Instruments, Austin, TX) by custom software written in LabVIEW ((National Instruments, Austin, TX). Appropriate running voltages were determined using a solution of rhodamine B and running buffer in the sample reservoir. Gated injections[16] were performed by altering the applied voltages to force fluid from the sample reservoir to flow into the separation channel. The fluid flow was viewed through a TE300 inverted microscope (Nikon, Melville, NY) equipped with a 20X objective, a high pressure mercury lamp, and a NTE/CCD-512-EBFT camera (Roper Scientific, Trenton, NJ). The electric field strength used for all studies was approximately 200 V/cm, which was low enough to prevent the formation of gas bubbles from electrolysis at the metal electrodes.

3.3 Results and Discussion

3.3.1 Metal Electrode Fabrication and Bonding Studies

The PDMS "sandwich" chip described in Chapter 2 was convenient for initial conductivity studies since the PDMS flexibility sealed the channel layer around the electrodes. However, this elasticity was also a disadvantage because it introduced variability in the detection region, which is detrimental to the detector's reproducibility. As a result, it was decided that a microchip fabricated completely of fused silica or quartz (to limit light absorbance by the substrate) would be favorable. Initial chip fabrication used 30 nm thick

electrodes deposited onto the quartz surface. Attempts to bond around the "raised" electrodes resulted in pockets of unbonded substrate around the metal films (Figure 3-4 A and C). Buffer was easily drawn into these gaps, and when the electrophoresis running voltage was applied, bubbles from electrolysis formed between the substrates and damaged the electrodes.

The solution to the bonding problems was to either use very thin electrodes (sub 15 nm) or to etch the electrode design prior to applying the metal film, essentially embedding the electrodes. Studies of electrode thickness in Chapter 2 and a few tests with the quartz microchip demonstrated that thin electrodes have a short lifetime. While adding an extra step to the fabrication process, the embedded electrodes can be fabricated to any thickness without any detriment to the substrate bonding procedure (Figure 3-4 B and D). Metal films of 30 nm chrome and 70 nm platinum in etched trenchs of 100 nm were used during these tests and exhibited long lifetimes.

The upper bonding temperature also presented problems during microchip fabrication. Fused silica and quartz are usually fusion bonded at temperatures in excess of 1000°C. However, studies have shown that thin platinum films degrade rapidly at temperatures above 700°C.[12] A maximum temperature of 550°C typically used for B270 chips was tested and appeared to provide sufficient bonding between substrates to adequately hold the chip together. Bonding integrity was tested with long term sonication for up to 2 hours without effect. A razorblade was impinged at the substrate junction in an attempt to pry them apart, but the substrates chipped under the pressure leaving the bonding unaffected.

3.3.2 Comparison of Metal Electrode and PSBE Microchips

Figure 3-5 (top) shows a typical analysis run with the outputs of both the conductivity and photothermal lock-ins. Seven second fronts of 50 μM DABSYL-glucosamine were gate injected into the analysis channel in order to determine the absolute signal for the analyte under the given conditions. These injections were long enough to produce flat-topped "peaks," allowing for a known analyte concentration (50 μM) at the peak maximum. 10 ppm potassium chloride was also added to the analyte solution as a check for the conductivity detector response. The buffer was 20 mM MES/His adjusted to pH 6.1. A segment of the conductivity trace, demonstrating signal modulation caused by laser beam chopping, is expanded and shown in Figure 3-5 (bottom). This is the signal which is subsequently isolated for photothermal data. The metal electrode chip used in these studies had electrodes 50 μm wide with a 100 μm gap and a channel 30 μm deep and 100 μm wide. The PSBE chip had a 100 μm electrode "width" and 20 μm spacing and channel 12 μm deep and 75 μm wide.

3.3.2.1 Electronic Excitation Investigations

Both the metal film electrodes and the PSBEs were investigated to determine their response to excitation signal variation. For these studies, the laser was set to 48 mW at the chip with 20 Hz modulation. The excitation voltage was set to 5.0 V_{pp} for the frequency studies, and the excitation frequency was set to 100 kHz for the voltage studies. For all studies, the excitation voltage and phase were balanced to minimize the conductivity background.

The detector's electrical behavior depends highly on the detection region geometry as the conductivity signal recorded depends on the resistance of the fluid in the detection cell. . Taking into account only amplification circuitry, the conductivity detector signal should reach a maximum at approximately 400 kHz. The capillary system using a capacitively coupled contactless conductivity detector experienced a maximum at 375 kHz.[1,3] Using only two electrodes for both microchip types, the background conductivity was observed. To cover the full range of frequencies in question, from 50 kHz to 500 kHz, a SR844 RF lock-in amplifier (Stanford Research Systems, Sunnyvale, CA) was used. Figure 3-6 shows the conductivity response to excitation frequency for the metal electrodes and PSBEs. The metal electrodes experienced a signal maximum at about 170 kHz, and the PSBEs experienced a signal maximum of approximately 140 kHz. The large shift in the maximum to lower excitation frequencies was due to the direct contact between the electrodes and the solution. The capacitance of the contacting electrodes, as compared to the contactless detector, was much higher, reducing the impedance to lower frequencies. However, due to its higher background noise in comparison to the SR810 lock-in amplifier, the SR844 lock-in was not used for other studies. Therefore, the input signal was limited to a maximum frequency of 102 kHz.[1,3]

Using the SR810 lock in amplifier, the photothermal signal response with excitation frequencies up to 100 kHz was studied for the two electrode types. Figure 3-7 displays the photothermal signal of 50 μM DABSYL-glucosamine with changing excitation frequency. Although the PSBE conductivity signal was higher than metal film electrodes for frequencies below 100 kHz, the photothermal signal was significantly lower. Conversely, the background noise for the PSBEs was much higher and increased with increasing frequency

while that for the metal electrodes remained fairly consistent at about 3-4 μV_{rms}. As a result, the signal to noise ratios for the metal electrodes were much higher for all frequencies (Figure 3-8). Signal to noise ratios for both electrodes dropped quickly below 20 kHz, but seemed to be reaching a maximum as frequencies were increased to 100 kHz.

The excitation voltage was also varied to observe the behavior of both types of electrodes. For these studies, the excitation frequency was set to 100 kHz, and the laser was set to 48 mW with 20 Hz modulation. Previous studies have shown that the conductivity signal, and therefore the photothermal signal, should increase linearly with increasing excitation voltage. Excitation voltages are reported according to the lower of the two voltages applied. When balancing the excitation signals to achieve null conductivity background, it was found that the metal electrodes were inherently more balanced, and only slight excitation voltage modifications were required to achieve a null conductivity background. The PSBEs were found to be more difficult to null, sometimes needing a 20% increase in the excitation signal of one function generators. As a result, the PSBEs studies were limited to under 7 V_{pp}, but the metal electrodes could be studied up to 9 V_{pp}.

Figure 3-9 shows the photothermal signal response and background noise for both types of electrodes. The metal electrode signal was larger and much more linear than the PSBE signal with the noise around at 3-4 μV_{rms}. Noise for the PSBEs increased linearly to almost an order of magnitude higher than the metal electrodes at the maximum voltage tested. The increased level and proportional behavior of the noise level for the PSBEs may have been caused by the large volume over which the measurements were made. The resulting signal to noise ratios (Figure 3-10) were much lower using the PSBEs than the metal electrodes. The metal electrode's signal to noise ratios increased with the excitation

voltage but gradually began to reach a roll-off point. Concern for electrode stability at the higher voltages led to using 5 V_{pp} as the standard applied excitation voltage.

During these studies, the formation of a black residue within the PSBE polymer was observed (Figure 3-3). The residue was suspected to be caused by the degradation of the polymer under a combination of heat from the laser, high DC running and AC excitation voltages, or analyte penetration and break-down. It is also suspected that residue may have increased resistance across the electrodes, resulting in the lower photothermal signal observed as studies progressed.

3.3.2.2 Optical Excitation Investigations

Assuming ideal behavior, the light absorbed by the analyte should relate linearly to the incident laser power to the detection region, resulting in a linear response in the photothermal signal. To determine the photothermal detector behavior using both types of electrodes, the excitation signal was set to 100 kHz and 5.0 V_{pp} while varying the laser power at 20 Hz modulation. The test analyte used was 50 µM DABSYL-tagged glucosamine with a 20 mM MES/His running buffer. Figure 3-11 shows the photothermal signal for both the metal electrodes and the PSBEs plotted against the incident laser power. In this case the photothermal signal of both electrodes was very similar and did display linear behavior. The noise observed with the PSBEs was nearly an order of magnitude higher than with metal electrodes. Noise for both electrode types was essentially independent of laser power for the range studied. The resulting signal to noise ratios (Figure 3-12) were much higher for the metal electrodes than the PSBEs.

The effect of changing the modulation (chopping) frequency was also studied. The incident laser power was set to 48 mW, and the excitation signal was 100 kHz and 5.0 V_{pp}. Theoretically, lower frequencies correspond to longer periods of exposure to the light and greater opportunity for absorbance, producing an inverse relationship between the modulation frequency and photothermal signal. This held true for both types of electrodes. The average photothermal signals for both the metal electrodes and the PSBEs were comparable, but the PSBEs displayed reduced stability at the lower frequencies (Figure 3-13). Likewise, the photothermal noise was higher at the lower frequencies, and again the noise for the PSBEs was significantly greater than for the metal electrodes. The increased noise at low modulation frequencies was partially due to the longer exposure periods (possibly increasing convection due to heating). The SR540 optical chopper (Stanford Research Systems, Sunnyvale, CA) was also found to have a significant wobble at the lower frequencies and was unreliable below 4 Hz. As a result, both electrodes demonstrated a maximum signal to noise ratio between 20 and 30 Hz (Figure 3-14), with the signal to noise ratios for the metal electrodes being several times greater than the PSBEs.

3.3.3 Channel Depth Investigation

The comparison of the metal electrode and PSBE chips showed the PSBEs to be inferior. Therefore, all following studies were performed using metal electrode detectors. Laser power variations and modulation frequency were used to characterize the effects of channel depth. Three microchips were fabricated with channel depths of 15, 30, and 45 μm deep channels. Masks with channel designs of 50 (for the 15 μm deep channel), 25 (for the 30 μm deep channel), and 10 μm (for the 45 μm deep channel) wide exposed areas were used

to fabricate channels that were close to 100 μm in width. The DC electrophoresis voltages were controlled to maintain approximately 200 V/cm electric field strength in the separation channel of each chip. The excitation signal was set to 100 kHz and 5.0 V_{pp}.

The effect of laser power is shown in Figure 3-15. As expected, the photothermal response scaled linearly ($R^2 \geq 0.994$) with the laser power between 5 and 80 mW. The slopes of the lines were 5.3 x 10^{-5} V/mW, 3.5 x 10^{-4} V/mW, and 4.8 x 10^{-4} V/mW for the 15, 30, and 45 μm deep channels, respectively. Noise for the 15 μm deep channel was approximately half that of the 30 μm and 45 μm channels, which were similar. The noise for the 30 μm deep channel was more proportional to laser power than the other two, resulting in a slightly curved signal to noise plot (Figure 3-16). This curve showed that the signal to noise values for the 30 μm and 45 μm deep channels were similar for the lower laser powers, but the ratio increased at a greater rate for the 45 μm deep channel at the higher laser powers. Examining the highest laser power of about 80 mW, the signal to noise ratios were proportional to the channel depth, i.e. S/N for the 15 μm deep channel is about half that of the 30 μm deep channel and one third that of the 45 μm deep channel.

The photothermal response to changing laser modulation frequency for the different channel depths also closely followed previous trends (Figure 3-17). In this case, it was interesting to note that while the 45 μm channel signal continued to increase in a 1/x fashion as it reached lower frequencies, the plots for the 15 μm and 30 μm deep channels showed a reduction of signal gain through decreased frequency below 20 Hz. This may indicate that a greater amount of heat is escaping to the chip substrate with the shallower channels during each "on" phase, but the 45 μm channel provided enough volume to continue to heat the solution within the channel. As observed previously, the photothermal noise increases

rapidly at the lower frequencies, resulting in a maximum signal to noise ratio for all three depths between 20 and 30 Hz (Figure 3-18).

3.3.4 Electrode Gap Size Investigation

In the PDMS electrode gap studies, it was observed that smaller gaps result in greater conductivity signal and signal to noise ratios. However, focusing the laser spot between two electrodes adds another variable for consideration. The laser spot has a finite size, and at some point the heat from absorbance and any light scatter will begin to affect the measured photothermal response. Simulations with a 12 μm focused laser spot indicated that the majority of the region heated by the laser extended about 100 μm from the laser spot.[1] A gap size of 100 μm was postulated to incorporate the most intensely heated area without adding excessively to detection cell volume. To study the behavior of photothermal detection with respect to electrode gap size, three chips were made with electrode gaps of 100, 50, and 25 μm.

3.3.4.1 Laser Power Investigations

To test the laser power response for the three electrode gap sizes, the excitation signal was set to 100 kHz and 5 V_{pp}, and the chopper modulation frequency was set to 20 Hz. Figure 3-19 shows the photothermal response with respect to laser power for the three gap sizes. The slope of the 100 μm gap line was approximately half that of the 50 μm gap and one third that of the 25 μm gap. Looking at the photothermal noise values, the noise for the 100 μm and 50 μm gaps were comparable, the noise for the 25 μm gap was several orders of magnitude higher. This indicated that light scatter was affecting the electrodes, heating the

metal which subsequently heats the solution, all happening through a means unrelated to analyte absorbance. The increased noise was related to small output power fluctuations in the laser which were transmitted through the electrodes in the same process. As a result, the signal to noise ratios for the 25 μm gap were much lower than the other two gap sizes and decreased with increasing laser power (Figure 3-20). The 50 μm electrode gap provided optimal signal to noise ratios for all laser powers studied.

3.3.4.2 Limit of Detection Comparison

A series of solutions were prepared with concentrations of DABSYL-tagged glucosamine between 1 and 100 μM in order to determine the limit of detection (LOD) and study the signal linearity for the devices with 100 μm and 50 μm electrode gaps. The LOD for the 25 μm gap electrodes was not studied due to the high noise observed in the previous experiments. The excitation signal for the studies was set at 100 kHz with 5.0 V_{pp}, and the laser power was set to 48 mV with 20 Hz modulation. The photothermal signal for different concentrations using both electrode gap sizes is displayed in the top plot of Figure 3-21. The responses were observed to be highly linear ($R^2 = 0.998$) for the range of concentrations studied. The signal to noise ratios for both gap sizes were also very linear (Figure 3-21, bottom). The limit of detection, defined to be at a signal to noise value of 3, was calculated to be 50 nM for the 100 μm gap electrodes and 17 nM for the 50 μm gap electrodes. Using a molar absorptivity of 29,000 $M^{-1}cm^{-1}$ for DABSYL glucosamine at 488 nm and a channel depth of 30 μm as the pathlength, the equivalent absorbance values for these concentrations were calculated to be 4.4 μAbs and 1.5 μAbs for the 100 μm and 50 μm gap electrodes,

respectively. These values are beyond the limits of detection for a conventional UV-Vis spectrophotometer.

A concentration test for the 50 μm gap electrodes was later run under identical conditions except increasing the incident laser power to 160 mW, the maximum output of the laser. The resulting limit of detection was 5 nM, with an equivalent absorbance of 0.4 μAbs. This was the best limit of detection obtained for the conductivity-based photothermal detection system to date.

3.3.5 Amino Acid Separation

A microchip-based photothermal detector was used in conjunction with a separation of three DABSYL-tagged amino acids, glycine, proline, and tryptophan. The three analytes were dissolved in the 20 mM MES/His buffer in 65/35 acetonitrile/water (v/v) to give a final concentration of 50 μM of each tagged amino acid. The system was set with a 100 kHz, 5 V_{pp} excitation signal and laser power of 48 mW with 20 Hz modulation. A 1 second gated injection was used to direct the analytes into the 3 cm separation channel, after which they were detected with 50 μm wide, 100 μm gap electrodes. The electropherogram for the separation of the three tagged amino acids is shown in Figure 3-22. Signal to noise ratios of 390, 455, and 452 were obtained for the tagged glycine, proline, and tryptophan, respectively. This was the first observed separation using conductivity based photothermal detection.

3.4 Conclusions

The development, characterization, and application of several microfluidic devices for conductivity-based photothermal detection were investigated. The first challenge undertaken was microchip fabrication, taking into account the necessity of using fused silica substrates and the presence of metal film electrodes. A series of chips were fabricated with different electrode film thicknesses and sputtering of films either directly to the substrate surface or in trenches. Poor bonding contact was observed with thicker surface electrodes, but substrates with thin films or embedded electrodes could be successfully bonded. Thick (approximately 100 nm) electrodes deposited in trenches were found to be the most robust. A bonding program with a maximum temperature of 550°C was found to provide plenty of bonding between the layers for these experiments.

The characterization of PSBEs for photothermal detection was also investigated. These electrodes circumvent problems with bonding and electrolysis associated with metal film electrodes and display similar signal response. However, the photothermal noise observed with these electrodes was up to an order of magnitude higher than noise associated with metal electrodes, resulting in reduced signal to noise values. The PSBE lifetime was limited to a few days, and the formation of dark residues in the polymer suggested chemical or physical changes to the electrodes.

Conversely, the metal film electrodes had long lifetimes, providing chrome oxidation or damage from gas bubbles formed by electrolysis was avoided. As long as electric field strengths were kept at 200 V/cm or below, no electrolysis was observed. Variation in excitation voltage, excitation frequency, laser power, and modulation frequency produced photothermal responses according to the expected trends. Channel depth studies

demonstrated path-length dependence, with deeper channels producing higher signals. For future studies, an investigation of channel width may present interesting results. By narrowing the width of the channel, the detection volume can be decreased to further increase the photothermal signal. Consideration would need to be given to the shape of the etched channel, as reduced depth decreases the signal and rough channel walls would increase laser scatter.

While data presented in Chapter 2 showed that closer spaced electrodes produced higher signal and signal to noise values, the finite size of the focused laser beam should to be taken into account with photothermal detection. Electrodes with a 25 μm gap size demonstrated good a photothermal signal, but the noise was orders of magnitude greater than that seen with larger gaps and showed a direct relation between laser power and noise. The high noise indicated that a 25 μm gap between electrodes was too small with the 12 μm laser spot, and the electrodes themselves were being heated directly by laser scatter. A gap size of 50 μm was found to be the best balance of electrode spacing and distance from the laser spot, and a detection limit of 5 nM for DABSYL-tagged glucosamine was obtained. This was the lowest limit of detection obtained with photothermal detection to date, and it is well below the limits of commercially available absorbance systems.

The successful implementation of a microfabricated photothermal detector was demonstrated. However, by using a visible wavelength laser, detection was still limited to tagged analytes. Should the detector employ excitation using a UV wavelength, which a far greater number of analytes will absorb, absorption detection of native analytes with the same order of sensitivity as amperometric or even fluorescence detection might be achieved. Biological molecules especially absorb well in the far UV range. Currently, one common

method of detection for biological samples is fluorescence detection, which often involves large fluorescent tags that can affect molecular behavior. Application of the microfabricated photothermal absorbance detector in the UV could open up a variety of applications for the analysis of native biological samples.

3.5 Tables and Figures

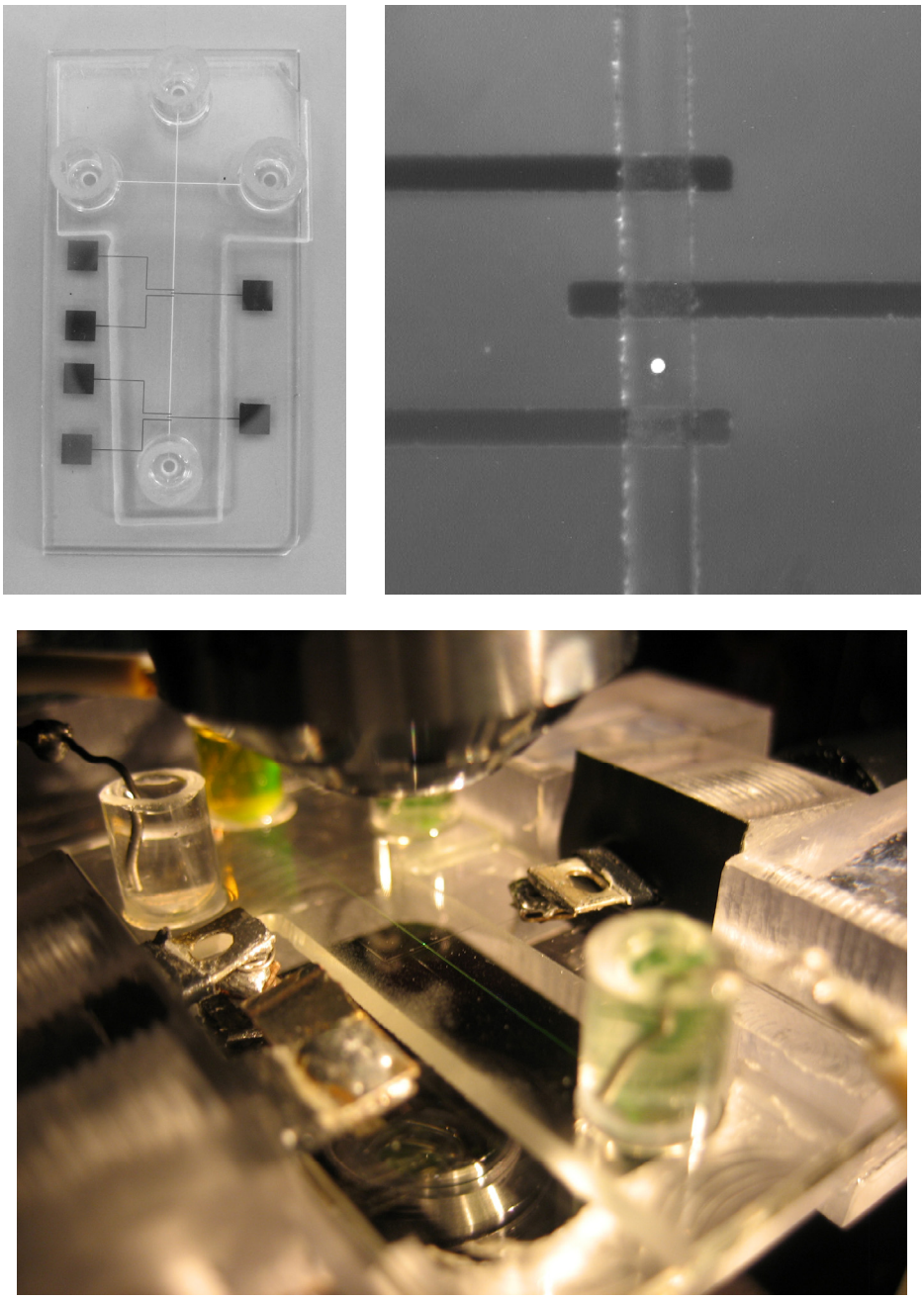

Figure 3-1: Images of the metal electrode quartz chip for photothermal detection: (top left) Quartz chip with two sets of detection electrodes and cross channel. (top right) Electrodes (50 µm width, 100 µm gap) with focused laser spot. (bottom) The micro chip in the photothermal setup, showing detection electrode lead connections, leads for the high voltage power supply, viewing microscope objective.

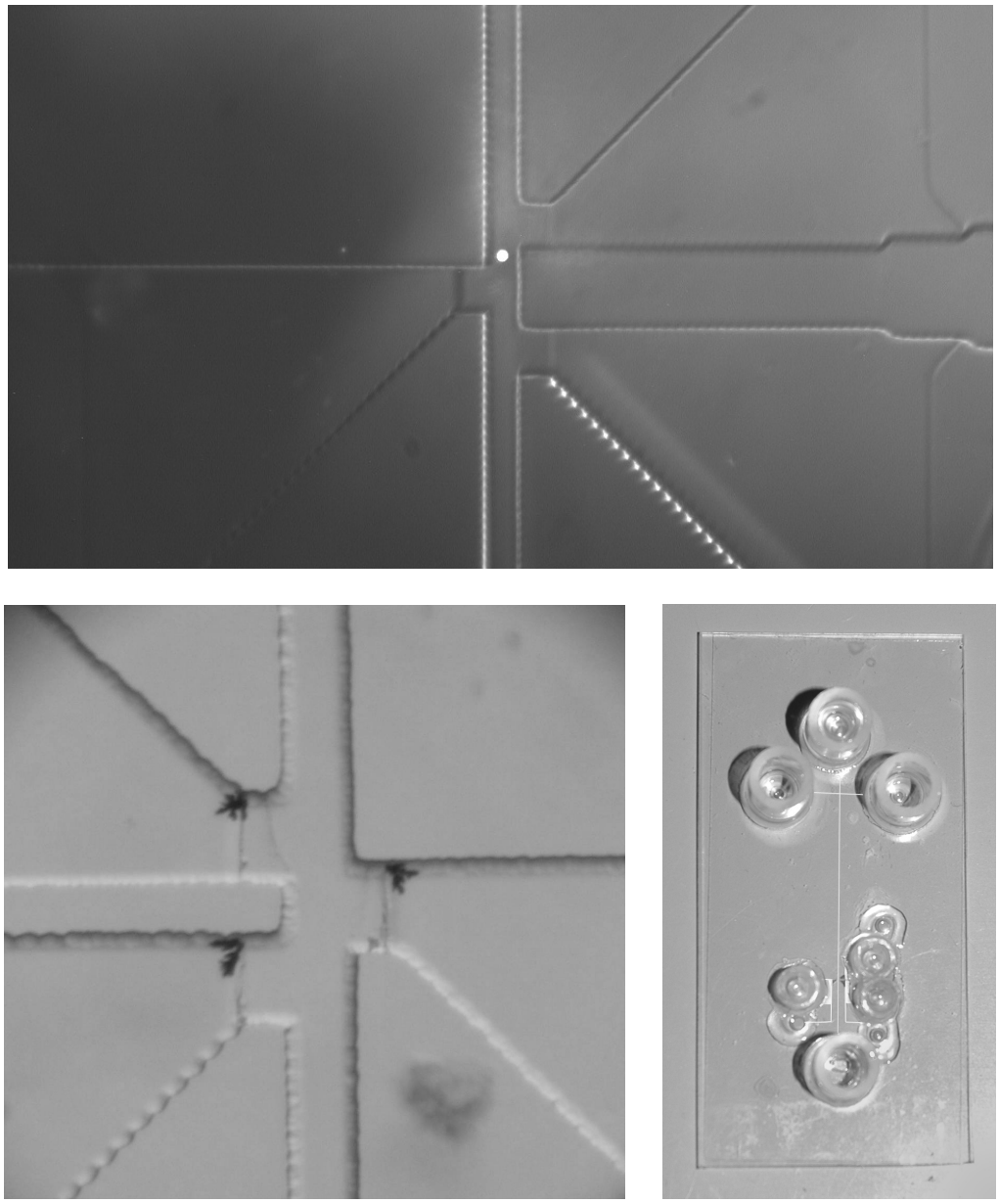

Figure 3-2: Images of the PSBE microchip for photothermal detection: (top) PSBE chip with the laser spot focused between the top two electrodes (100 µm wide, 20 µm gap). Faint lines indicate the polymer edges. (bottom left) PSBE electrodes with dark residue noticed in the excitation voltages studies. (bottom rignt) Full image of the PSBE microchip.

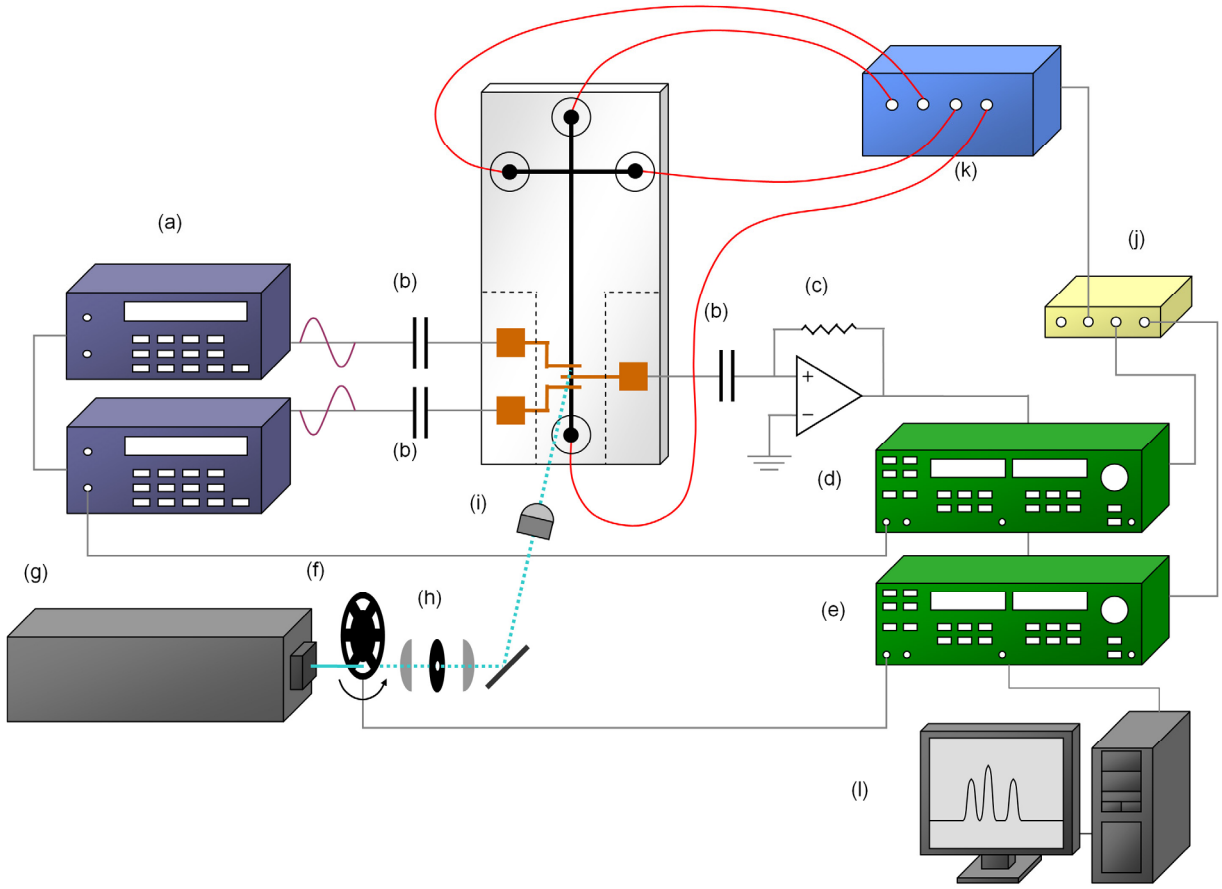

Figure 3-3: Schematic of the microchip photothermal setup, with the microchip containing the separation channels and electrodes shown at the center. Individual components are (a) two phase-locked function generators, (b) high voltage capacitors for isolation of AC components from the DC electrophoretic running voltage, (c) current to voltage amplifier circuit, (d) conductivity lock-in amplifier, (e) photothermal lock-in amplifier, (f) optical chopper, (g) laser, (h) spatial filter, (i) 40x microscope objective for beam focusing, (j) DAQ board, (k) high voltage power supply, and (l) computer for system control and data aquisition. The reference for the conductivity lock-in amplifier is supplied by one function generator, and the reference for the photothermal lock-in amplifier is supplied by the optical chopper.

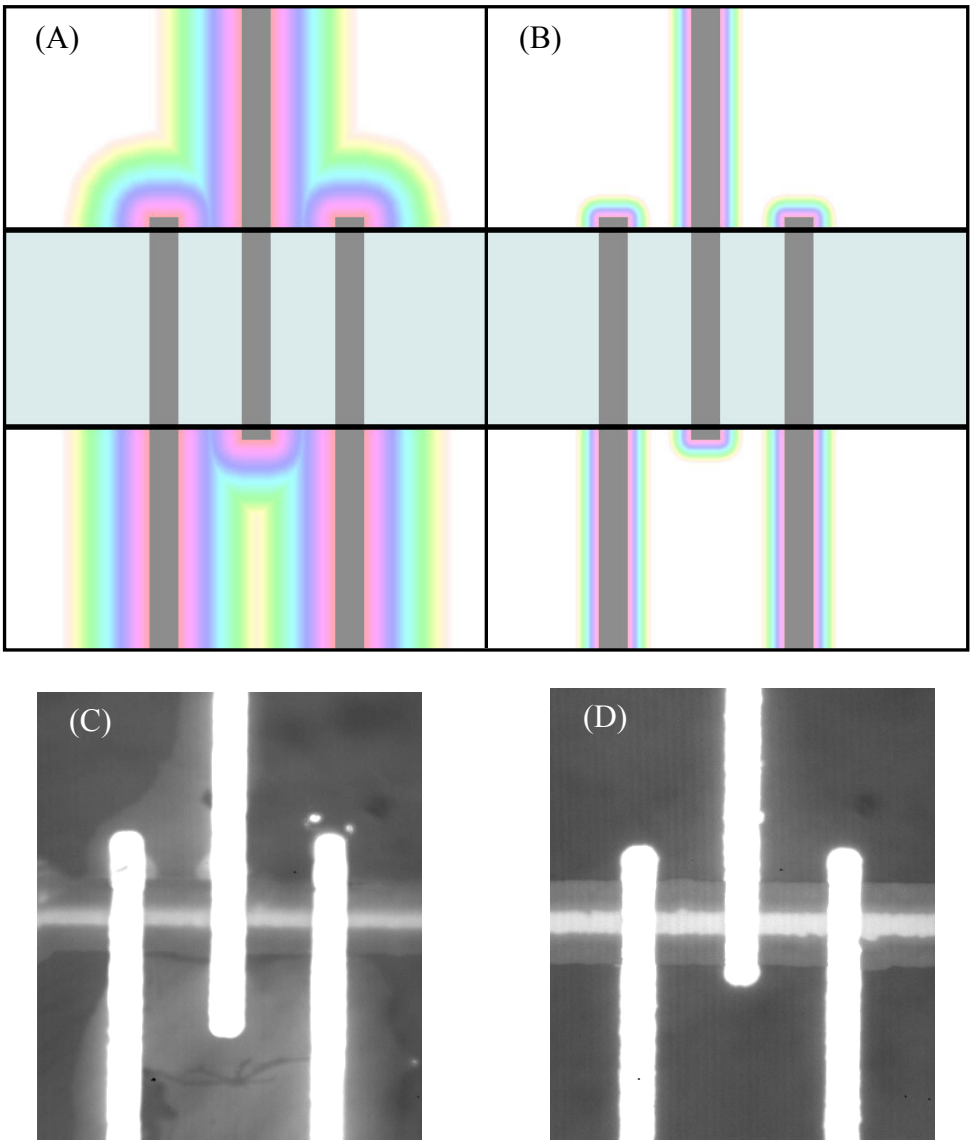

Figure 3-4: Diagram demonstrating bonding gaps around (A) thick electrodes and (B) thin or embedded electrodes, and reflective images of (C) poor bonding around thick electrodes and (D) complete bonding with thin electrodes.

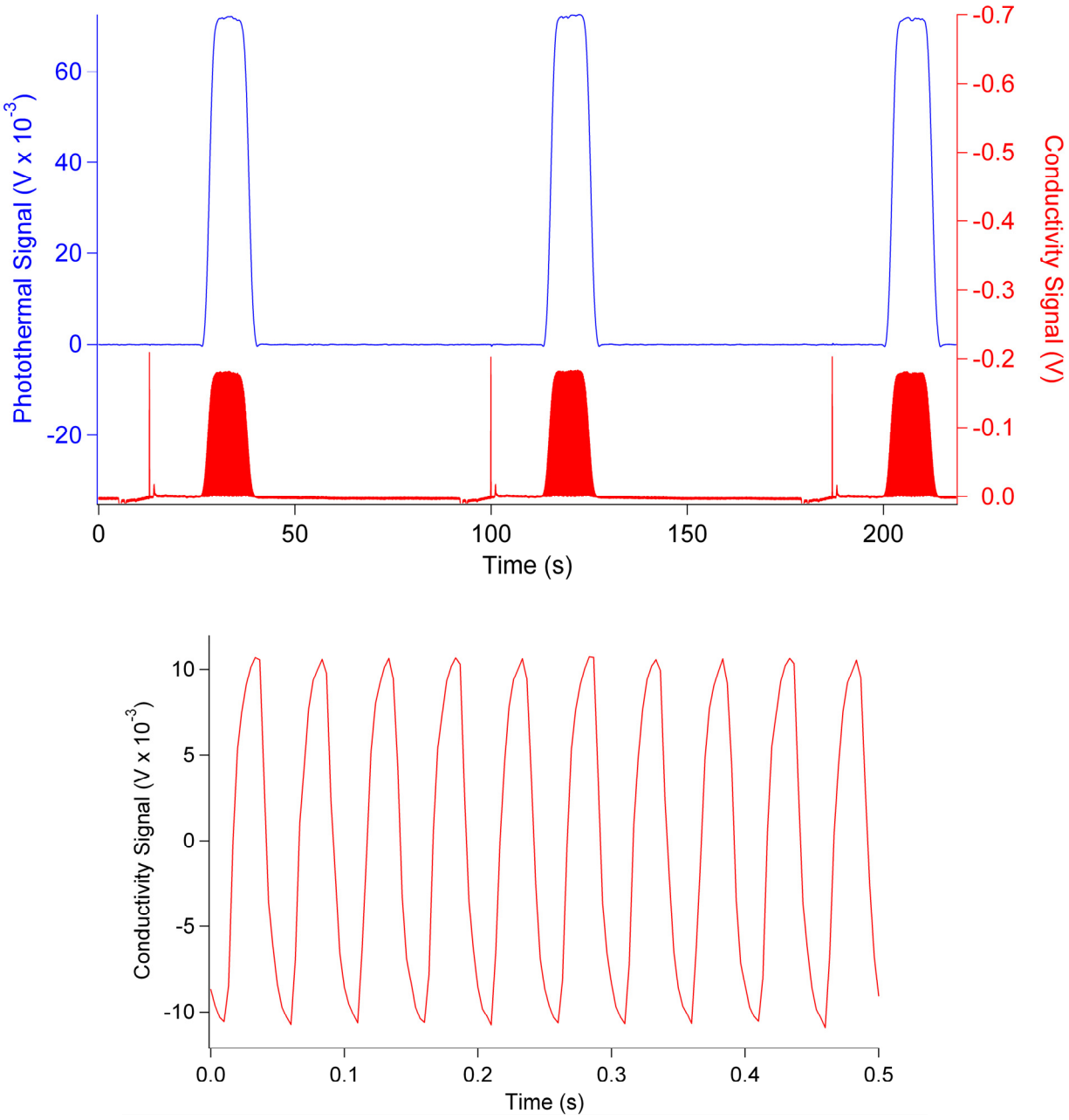

Figure 3-5: (top) Standard plot of photothermal data for three 7 s injections of 50 µM dabsyl glucosamine with 20 mM MES/His buffer. The red trace is the output of the conductivity lock-in, and the blue trace is the output of the photothermal lock-in. (bottom) expanded segment of the conductivity trace to show oscillation from laser modulation.

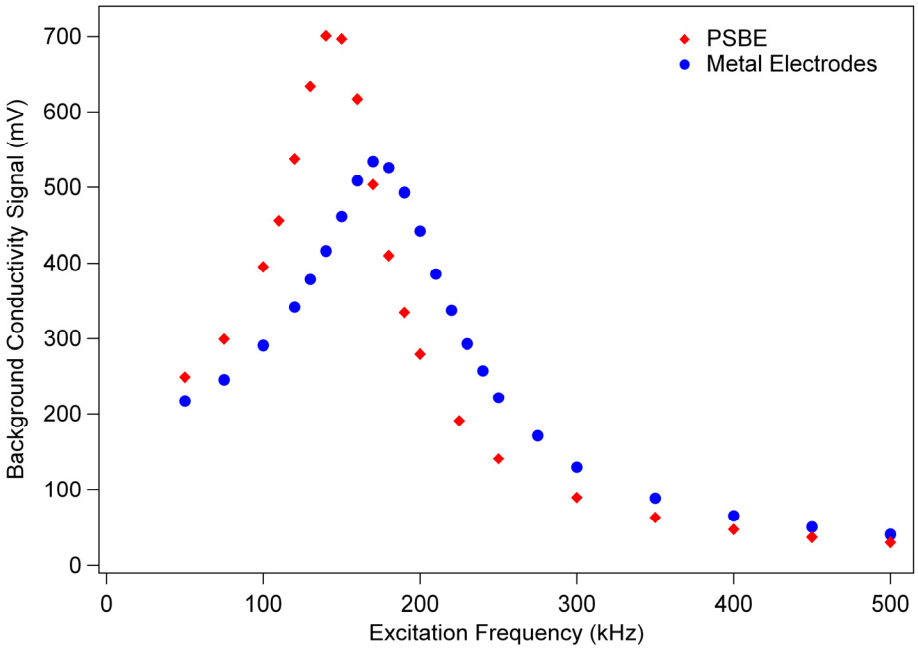

Figure 3-6: Conductivity response to excitation frequency for the metal electrodes and PSBEs measured with the SR844 RF lock-in amplifier. Excitation voltage was 1 V_{pp}.

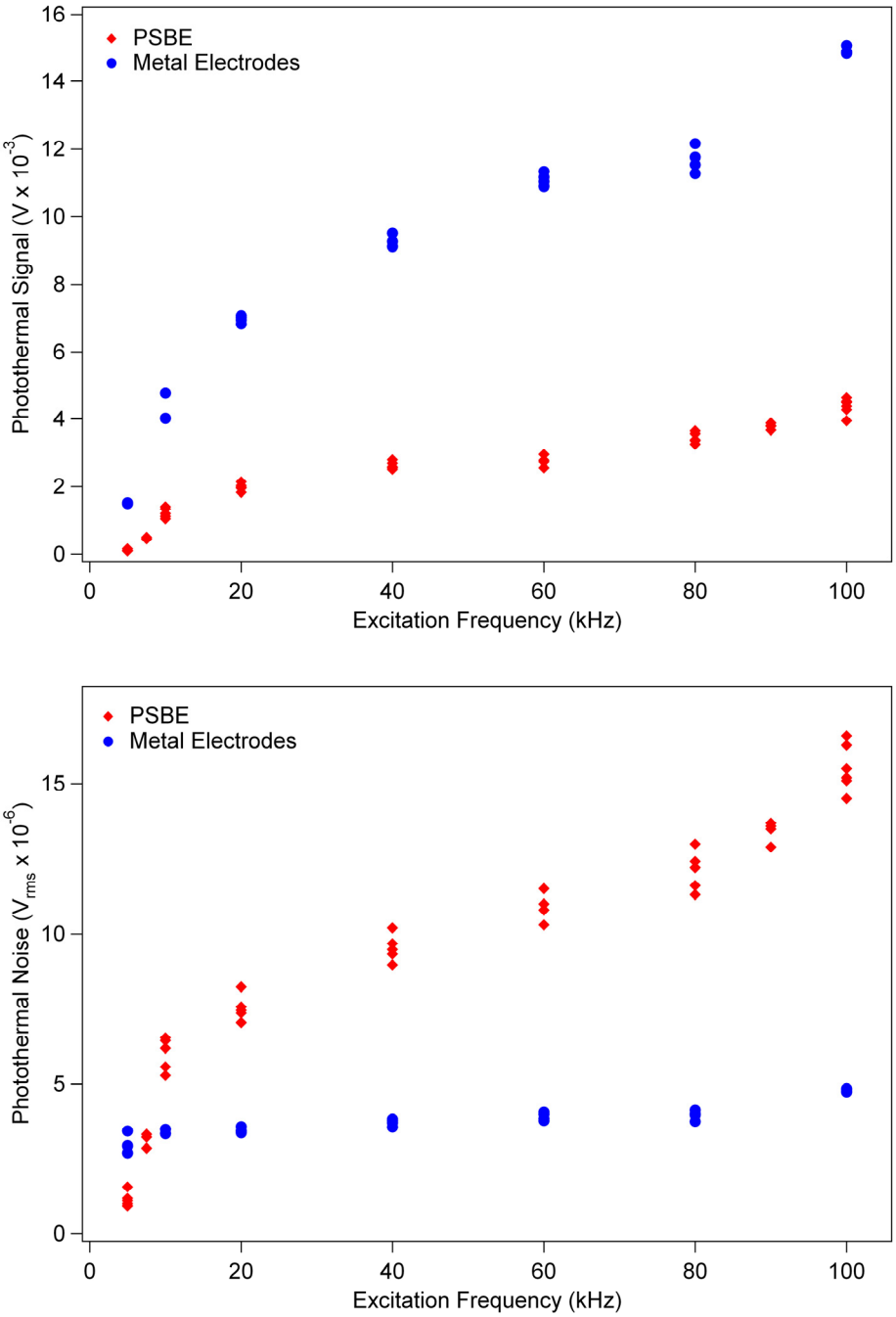

Figure 3-7: The photothermal signal of 50 µM DABSYL-glucosamine (top) and background noise (bottom) for both metal electrodes and PSBEs plotted against excitation frequency. Laser modulation frequency was 20 Hz, power was 50 mW and the excitation voltage was 5 V_{pp}.

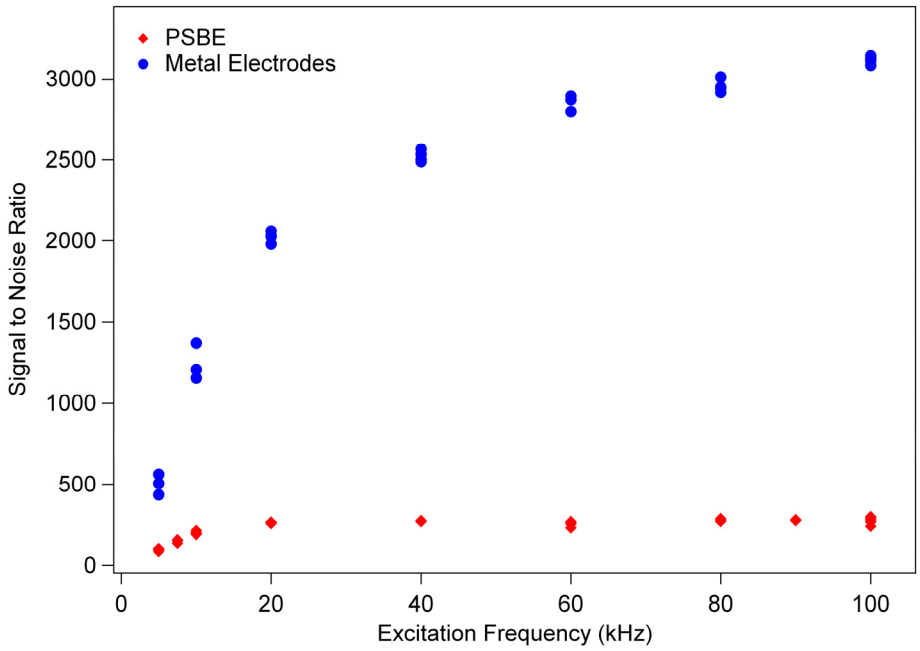

Figure 3-8: The photothermal signal to noise ratios of 50 µM DABSYL-glucosamine for both metal electrodes and PSBEs plotted against excitation frequency. Laser modulation frequency was 20 Hz, power was 50 mW and the excitation voltage was 5 V_{pp}.

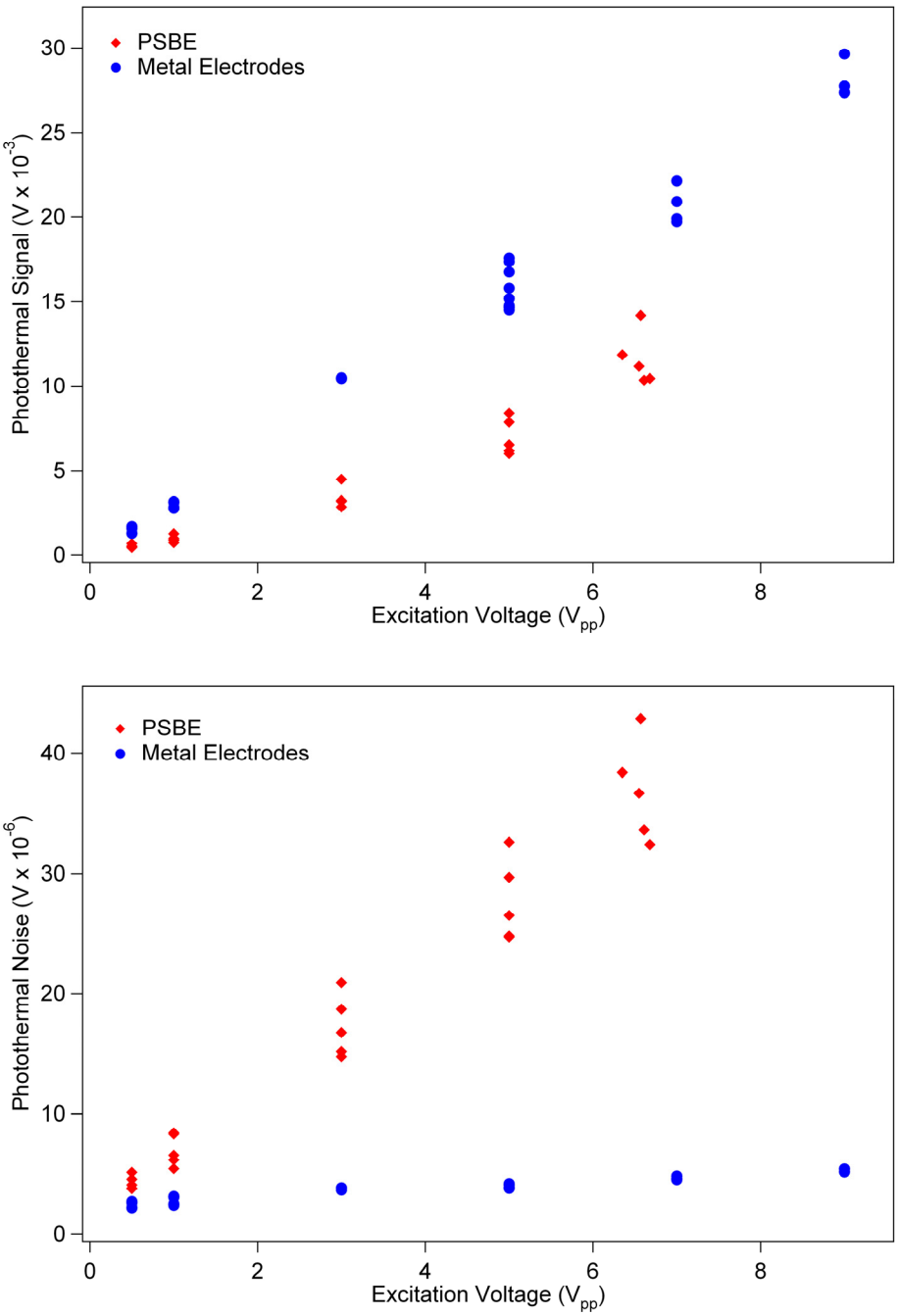

Figure 3-9: The photothermal signal of 50 μM DABSYL-glucosamine (top) and background noise (bottom) for metal electrodes and the PSBEs plotted against the excitation voltage. Laser modulation frequency was 20 Hz, power was 50 mW and the excitation frequency was 100 kHz.

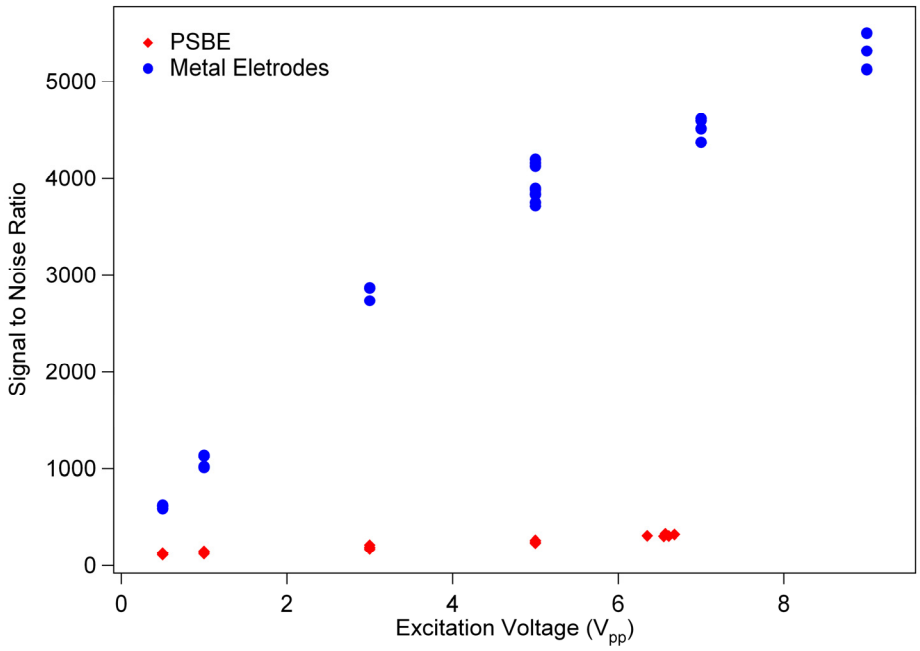

Figure 3-10: The photothermal signal to noise ratios of 50 µM DABSYL-glucosamine for metal electrodes and the PSBEs plotted against the excitation voltage. Laser modulation frequency was 20 Hz, power was 50 mW and the excitation frequency was 100 kHz.

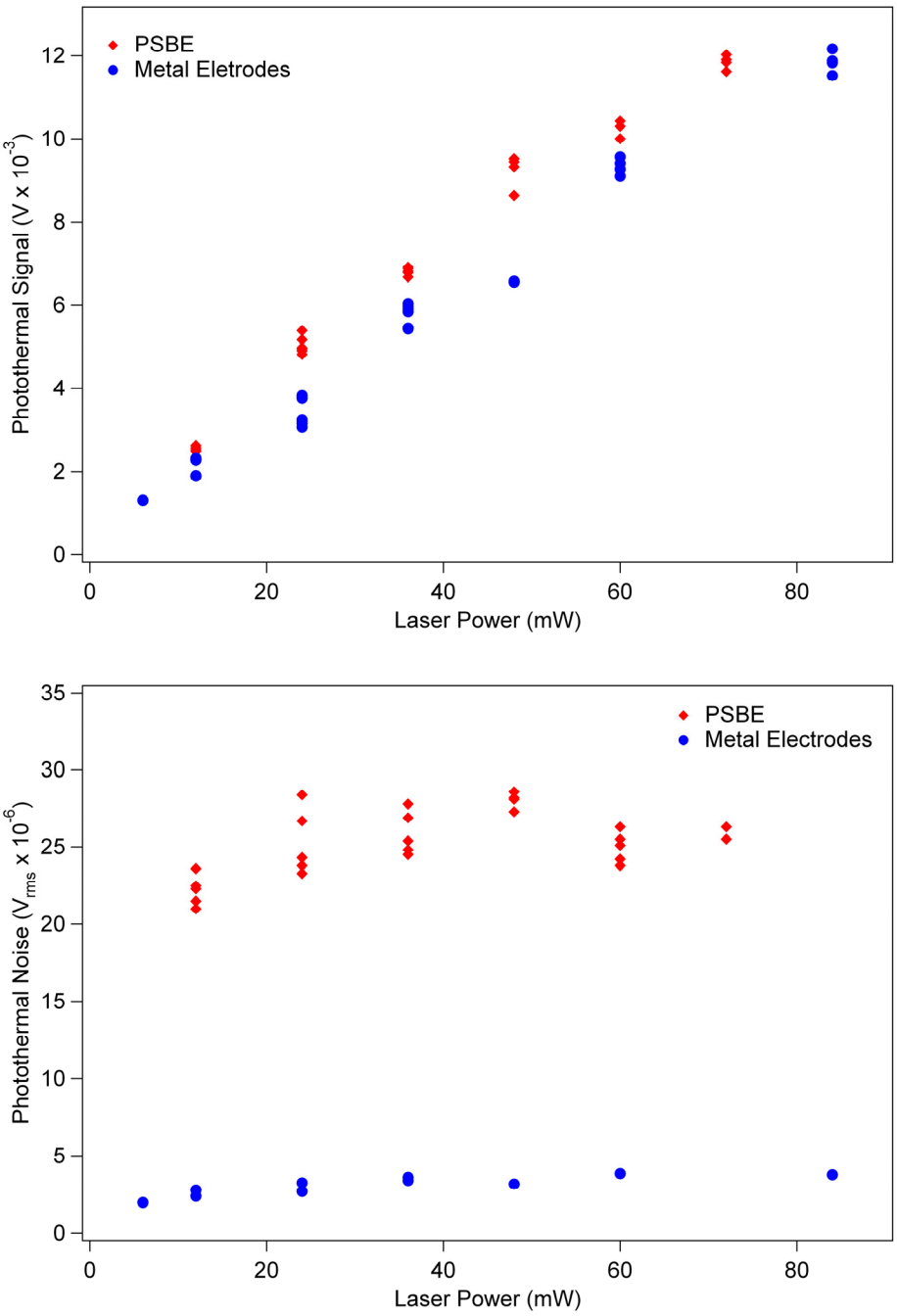

Figure 3-11: The photothermal signal of 50 µM DABSYL-glucosamine (top) and background noise (bottom) for metal electrodes and the PSBEs plotted against the laser power. Laser modulation frequency was 20 Hz and the excitation signal was 100 kHz and 5 V_{pp}.

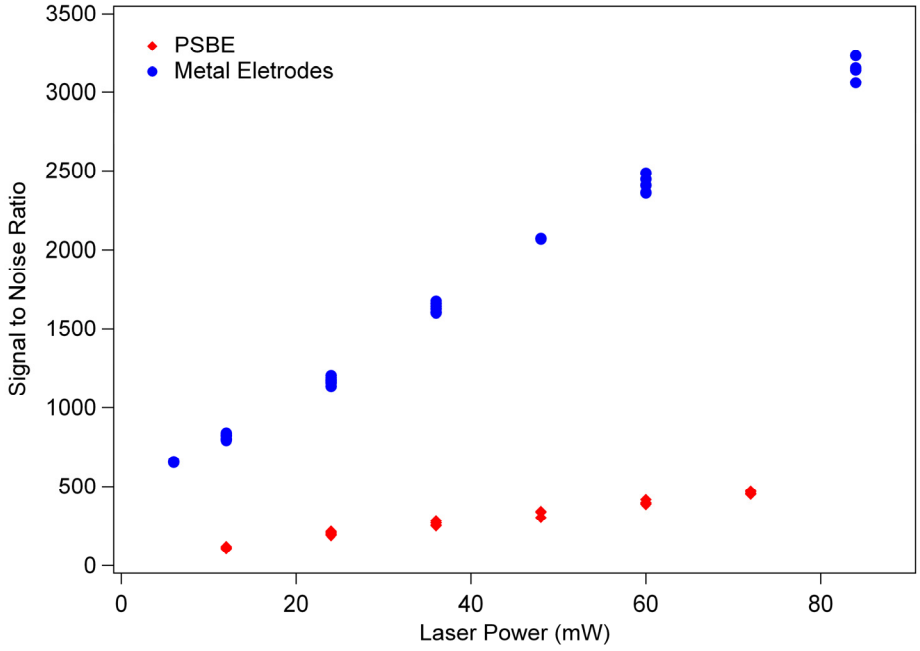

Figure 3-12: The photothermal signal to noise ratioof 50 µM DABSYL-glucosamine for metal electrodes and the PSBEs plotted against the laser power. Laser modulation frequency was 20 Hz and the excitation signal was 100 kHz and 5 V_{pp}.

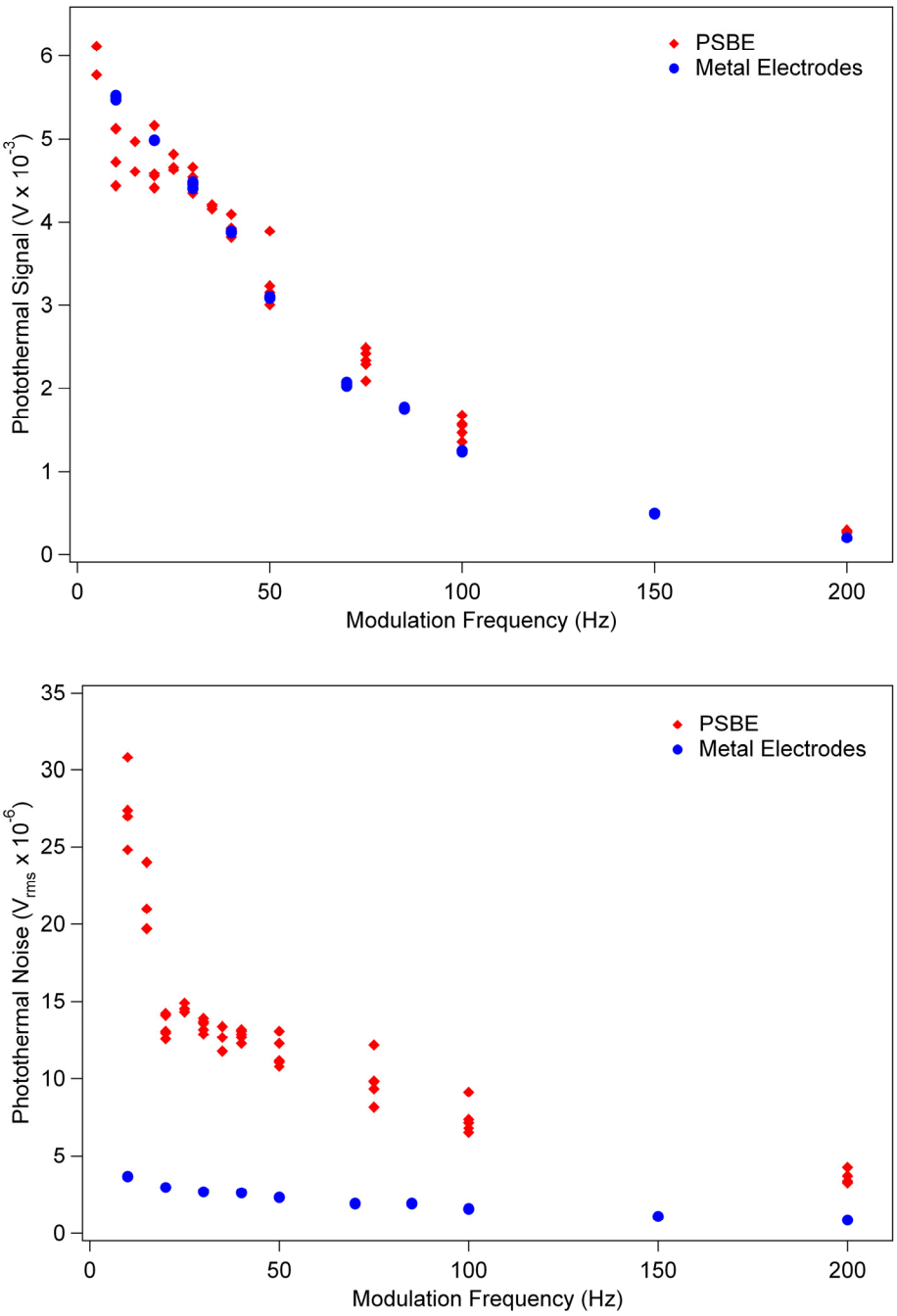

Figure 3-13: The photothermal signal of 50 µM DABSYL-glucosamine (top) and background noise (bottom) for metal electrodes and the PSBEs plotted against the laser modulation frequency. Laser power was 50 mW z and the excitation signal was 100 kHz and 5 V_{pp}.

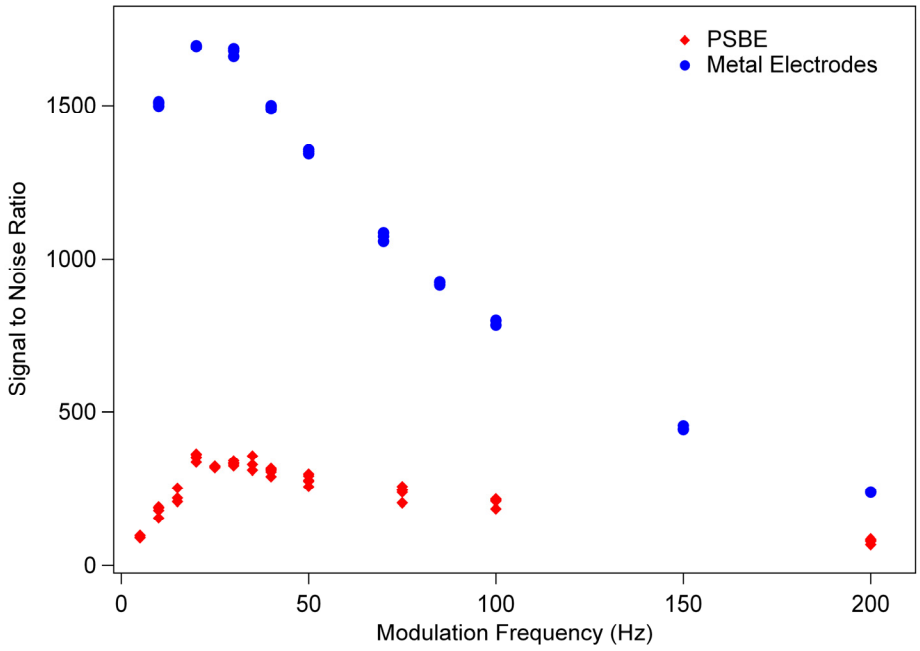

Figure 3-14: The photothermal signal to noise ratio of 50 µM DABSYL-glucosamine for metal electrodes and the PSBEs plotted against the laser modulation frequency. Laser power was 50 mW and the excitation signal was 100 kHz and 5 V_{pp}.

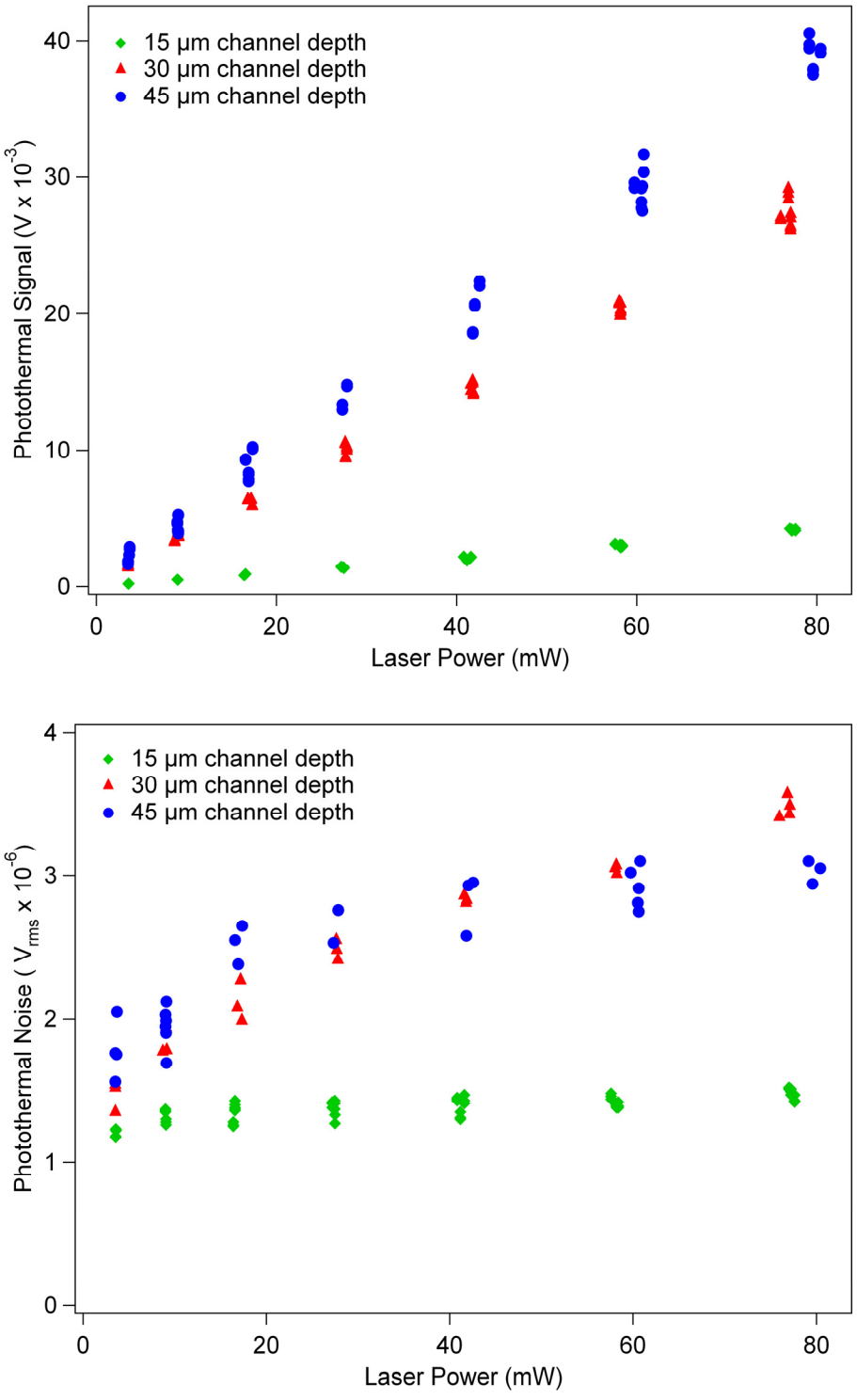

Figure 3-15: The photothermal signal of 50 µM DABSYL-glucosamine (top) and the background noise (bottom) for 15, 30, and 45 µm channel depths as a function of laser power. Laser modulation frequency was 20 Hz, and the excitation signal was 100 kHz at 5 V_{pp}.

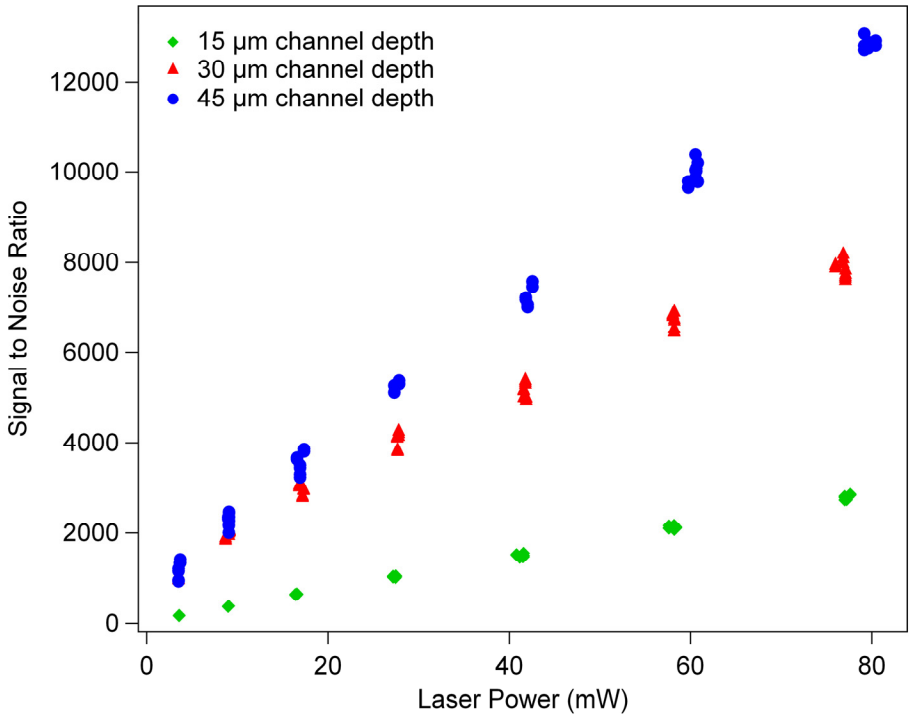

Figure 3-16: The photothermal signal to noise ratios of 50 µM DABSYL-glucosamine for 15, 30, and 45 µm channel depths as a function of laser power. Laser modulation frequency was 20 Hz, and the excitation signal was 100 kHz at 5 V_{pp}.

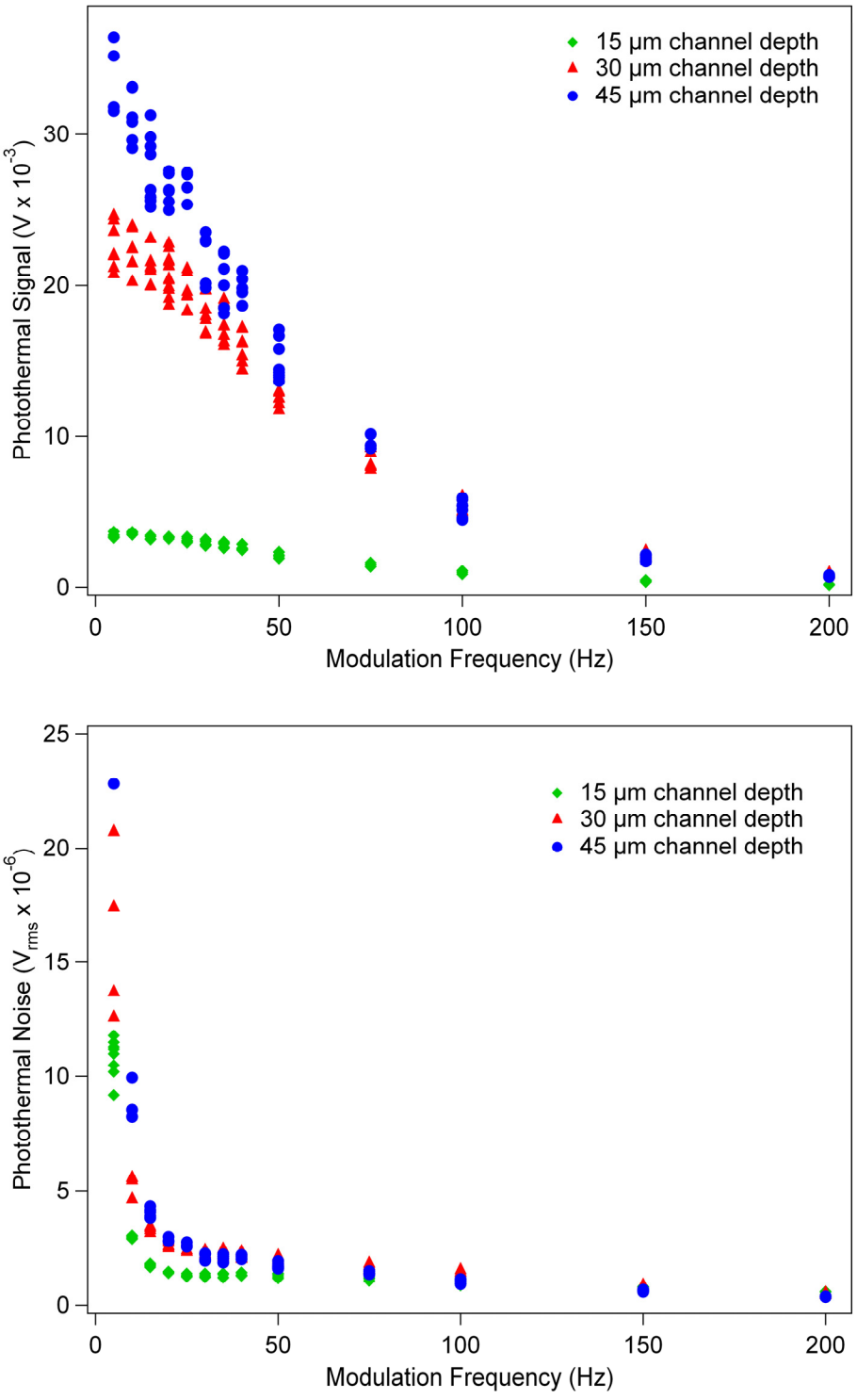

Figure 3-17: The photothermal signal of 50 µM DABSYL-glucosamine (top) and the background noise (bottom) for 15, 30, and 45 µm channel depths as a function of laser modulation frequency. Laser power was 50 mW, and the excitation signal was 100 kHz at 5 V_{pp}.

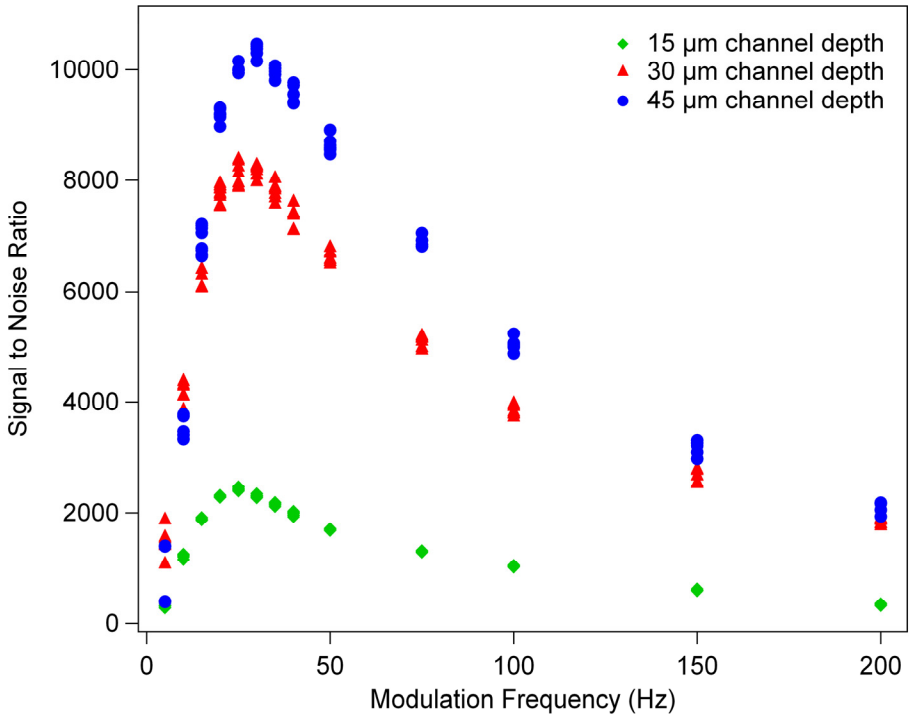

Figure 3-18: The photothermal signal to noise ratios of 50 µM DABSYL-glucosamine for 15, 30, and 45 µm channel depths as a function of laser modulation frequency. Laser power was 50 mW, and the excitation signal was 100 kHz at 5 V_{pp}.

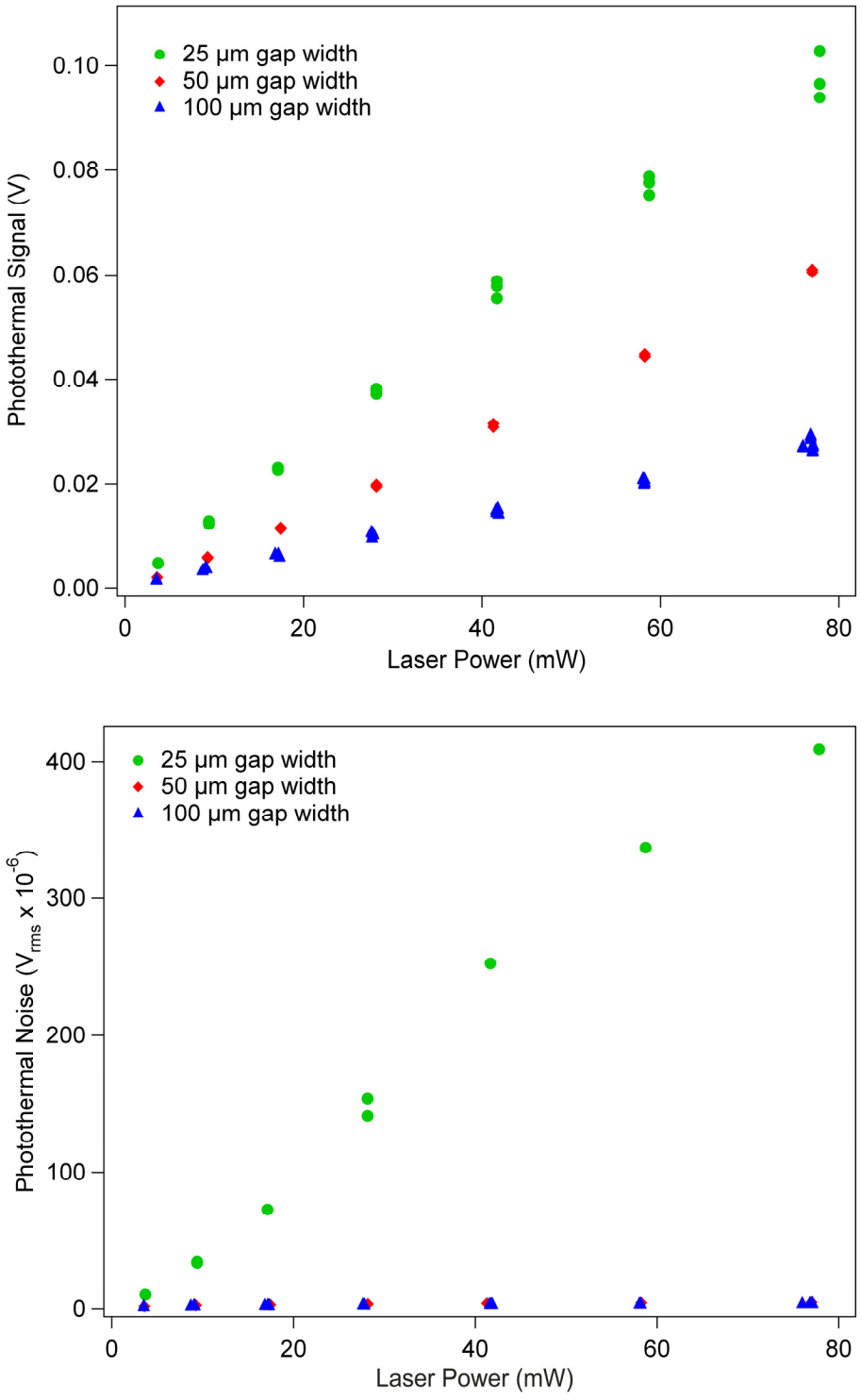

Figure 3-19: The photothermal signal of 50 µM DABSYL-glucosamine (top) and the background noise (bottom) for 25, 50, and 100 µm electrode gap widths as a function of laser power. Laser modulation frequency was 20 Hz, and the excitation signal was 100 kHz at 5 V_{pp}.

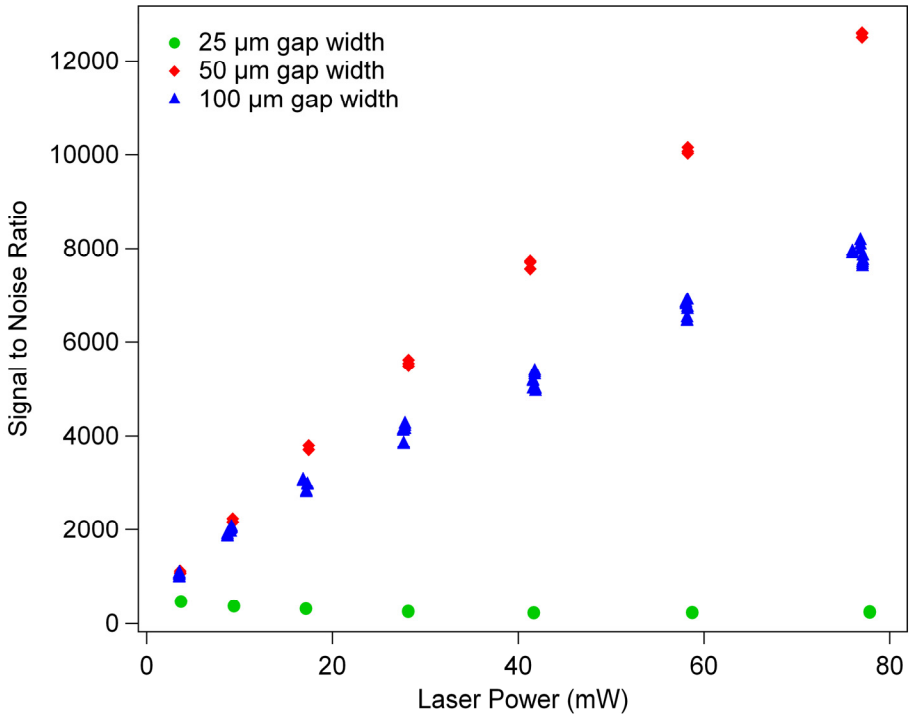

Figure 3-20: The photothermal signal to noise ratios of 50 µM DABSYL-glucosamine for 25, 50, and 100 µm electrode gap widths as a function of laser power. Laser modulation frequency was 20 Hz, and the excitation signal was 100 kHz at 5 V_{pp}.

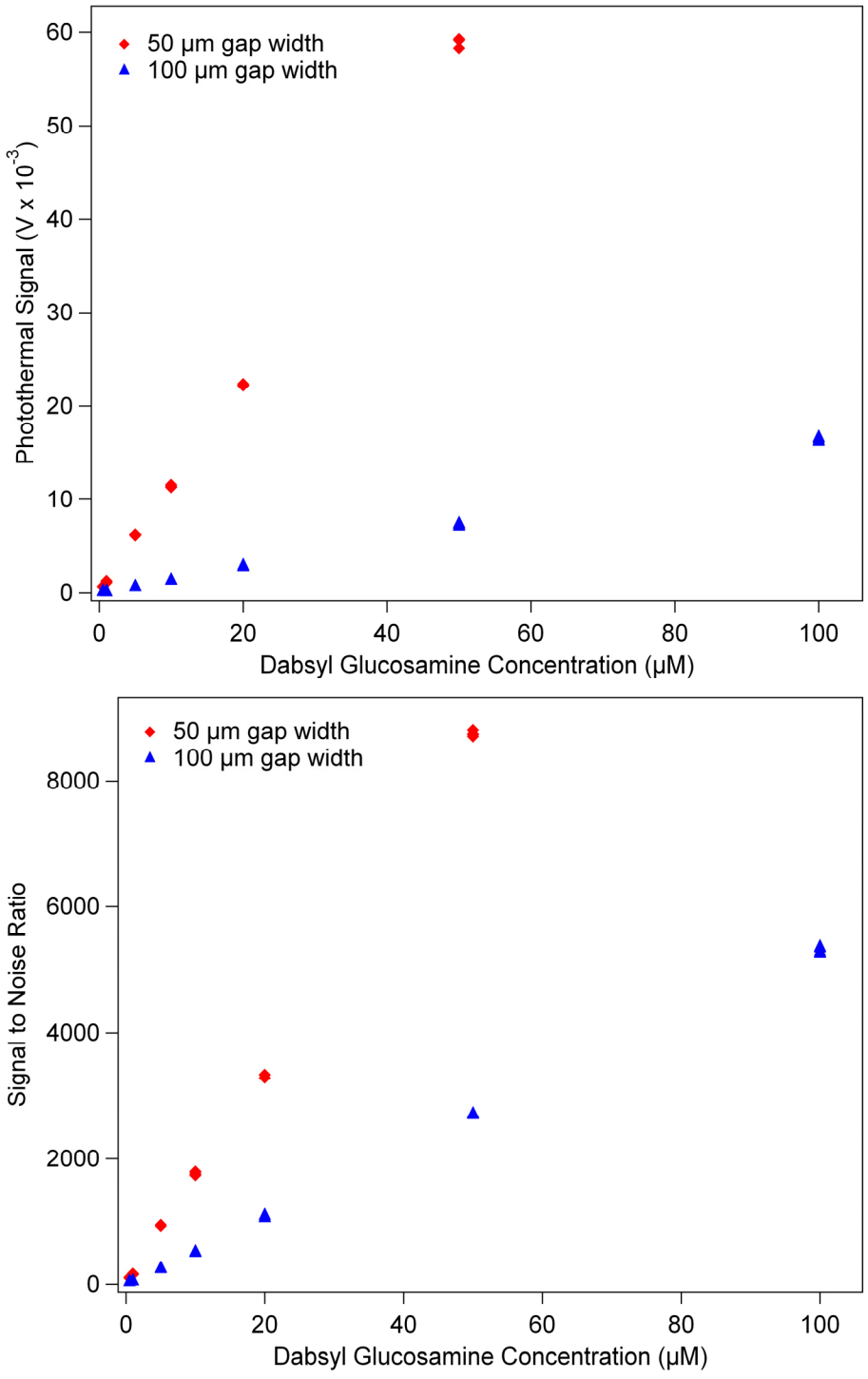

Figure 3-21: The photothermal signal (top) and signal to noise ratios (bottom) of DABSYL-glucosamine for 50 µm and 100 µm electrode gap widths as a function of analyte concentration. Laser modulation frequency was 20 Hz, laser power was 50 mW, and the excitation signal was 100 kHz at 5 V_{pp}.

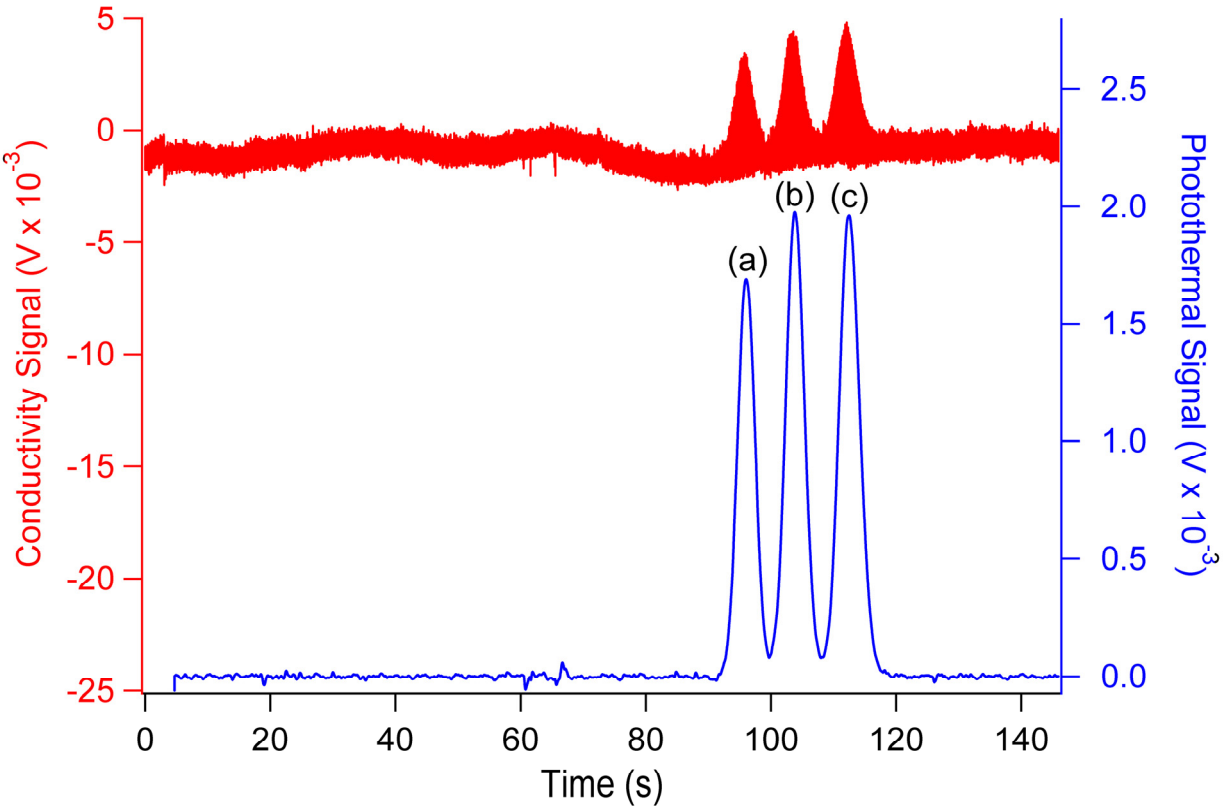

Figure 3-22: A separation of DABSYL-tagged glycine (a), proline (b), and tryptophan (c). *The conductivity trace is in red and the photothermal trace is in blue. The electrophoretic field was 200 V/cm, laser modulation frequency was 20 Hz, laser power was 50 mW, and the excitation signal was 100 kHz at 5* V_{pp}.

3.6 References

(1) Dennis, P. J. *Advancements and Applications of Ionic Conductivity Detection to Microcolumn and Microfluidic Separations*; Doctoral Dissertation, University of North Carolina at Chapel Hill, 2007.

(2) Fadgen, K. E. *Advancements in Detection for Micocolumn Separations*; Doctoral Dissertation, University of North Carolina at Chapel Hill, 2001.

(3) Johnston, S. E. *Applications of Conductivity Detection in Microcolumn Separations*; Doctoral Dissertation, University of North Carolina at Chapel Hill, 2005.

(4) Johnston, S. E.; Fadgen, K. E.; Jorgenson, J. W. *Analytical Chemistry* **2006**, *78*, 5309-5315.

(5) Johnston, S. E.; Fadgen, K. E.; Tolley, L. T.; Jorgenson, J. W. *Journal of Chromatography A* **2005**, *1094*, 148-157.

(6) Madou, M. J. *Fundamentals of Microfabrication*; CRC Press: Washington, DC, 2002.

(7) Bianchi, F.; Wagner, F.; Hoffmann, P.; Girault, H. H. *Analytical Chemistry* **2001**, *73*, 829-836.

(8) Lichtenberg, J.; de Rooij, N. F.; Verpoorte, E. *Electrophoresis* **2002**, *23*, 3769–3780.

(9) Laugere, F.; Guijt, R. M.; Bastemeijer, J.; van der Steen, G.; Berthold, A.; Baltussen, E.; Sarro, P.; van Dedem, G. W. K.; Vellekoop, M.; Bossche, A. *Analytical Chemistry* **2003**, *75*, 306-312.

(10) Harendt, C.; Graf, H.-G.; Hofflinger, B.; Penteker, E. *Journal of Micromechanical Microengineering* **1992**, *2*, 113-116.

(11) Jiao, J.; Lu, D.; Xiong, B.; Wang, W. *Sensors and Actuators A* **1995**, *50*, 117-120.

(12) Firebaugh, S. L.; Jensen, K. F.; Schmidt, M. A. *Journal of Microelectromechanical Systems* **1998**, *7*, 128-135.

(13) Chun, H.; Chung, T. D.; Kim, H. C. *Analytical Chemistry* **2005**, *77*, 2490-2495.

(14) Kim, S. K.; Kim, J. H.; Kim, K. P.; Chung, T. D. *Analytical Chemistry* **2007**, *79*, 7761-7766.

(15) Yu, M.; Dovichi, N. J. *Analytical Chemistry* **1989**, *61*, 37-40.

(16) Jacobson, S. C.; Koutny, L. B.; Hergenroder, R.; Moore, A. W.; Ramsey, J. M. *Analytical Chemistry* **1994**, *66*, 3472-3476.

Chapter 4: Photothermal Absorbance Detection on a Microfluidic Device with UV Excitation

4.1 Introduction

As discussed in Chapter 1, UV absorbance detection is a commonly used and nearly universal detection technique. However, the path length dependence defined in Beer's Law makes absorbance detection difficult to use in microcolumn or microfabricated systems that have very small dimensions.[1-4] Absorbance detection limits have been improved in these systems by using z cells,[5-9] bubble cells,[10,11] multireflection cells,[12-14] waveguides,[15-17] and other methods to increase the path length, but generally at the expense of resolution. More sensitive detection techniques, such as laser induced fluorescence (LIF), are highly selective but require modification or tagging of the analytes to be effective. Therefore, measurement of absorbance via conductivity-based photothermal absorbance detection has been introduced as a viable alternative to standard absorbance detection. By measuring absorbance by monitoring heat generation via conductivity changes, path length associated limitations can be reduced or even eliminated in an ideal system.

Problems with applying photothermal detection to capillary systems led to investigations to incorporate this method in a microfluidic platform. Microfluidic fabrication procedures were used to integrate the conductivity electrodes directly into a device equipped with fluidic channels (Chapter 2). Initial characterization of photothermal detection was carried out using a 488 nm argon ion laser for thermal excitation. As relatively few analytes absorb strongly at this wavelength, analytes tagged with 4-(dimethylamino)azobenzene-4'-

sulfonyl (DABSYL) chloride were used for development . While this system was effective for characterizing the method's basic properties, use of a tag negated any advantage over techniques like LIF. Utilizing a wavelength at which more native molecules are active would improve the practicality of photothermal absorbance detection.

Further modifications were also made to the initial photothermal microfluidic chip (Chapter 3). The initial chip made use of a basic cross design with a 4 cm long separation channel, which was useful for characterization tests but limited in its applicability to separations. To lengthen the channel on the limited space available, a serpentine channel shape, in which the channel alternates across the microchip's length in a series of 180° turns, could be utilized.[18] Low dispersion turns designed to reduce band broadening, as modeled by Griffiths and Nilson,[19] were used to combat induced broadening from non-uniform electric fields and fluid velocities that create the "racetrack" effect. To produce these turns, the channel tapers from the full width approximately three channel widths prior to the turn. The turn itself is about 28% the main channel width. The result is a turn in which the inner and outer arc lengths are nearly equal, reducing band broadening by two to three orders of magnitude. A similar design was used by Ramsey et al.[20] in order to perform two-dimensional separations of protein digests with high efficiency. These turns went from 75 μm in the main channel to 25 μm in the turn with a taper of 225 μm. Spacing between the main channels was 480 μm and the inner diameter of the turn was 580 μm.

The initial microfluidic chip design was also limited due the placement of the detection electrodes directly in the separation voltage field. As has been shown in previous experiments (Chapter 3), the high voltage used to produce electrokinetic flow can cause electrolysis and damage the electrodes. Limiting the electric field strength can prevent this,

but it also limits the separation speed and efficiency. If the electrodes could be completely removed from the electric field, electrolysis would no longer be a concern. One promising possibility is the use of opposing electroosmotic flow to create a buildup of pressure, forcing fluid into an electrically floating third channel. Using electroosmotic pumping in this manner was introduced by the Ramsey research group[21-23] as a method for generating electrospray on a microfluidic device. The device consisted of a single channel that ran to the chip edge and a side channel with a polyacrylamide coating to reduce electroosmotic flow. High voltage was applied to the main channel to induce electrokinetic flow and to the side channel to complete the electrical connection. With no electroosmotic flow in the side channel, fluid from the main channel was pumped out the chip to create the electrospray. The concept of electroosmotic pumping for electrospray was modified for the photothermal microchip. Since the electric field is restricted to the main separation channel and the side channel, placing the electrodes just past the channel intersection would put them in an effectively field-free region while using electroosmosis to direct fluid into the detection cell. The application of these modifications and characterization of UV photothermal absorbance detection of native analytes are discussed in this chapter.

4.2 Experimental

4.2.1 Materials

Guanosine, uracil, tryptophan, rhodamine B, and bovine serum albumin (BSA) were obtained from Sigma (St. Louis, MO). Sulfuric acid (H_2SO_4), sodium hydroxide (NaOH), glacial acetic acid solutions, and borax for borate buffer were purchased from Fisher Scientific (Fair Lawn, NJ). 2',7'–dichlorofluorescein (laser grade) was obtained from Acros

Organics (Geel, Belgium). The PolyE-323 surface coating was synthesized from 1,2-bis(3-aminopropylamino)ethane and epichlorohydrine purchased from Sigma Chemical Co. (St. Louis, MO). Oligonucleotide standards (5, 10, 15, 20, and 30 bases) were ordered from Protea Biosciences, Inc. (Morgantown, WV) and reconstituted in borate buffer. Buffer solutions were made with deionized water (Barnstead Nanopure Diamond Filtration System, Boston, MA). Electrophoresis running solutions were either 1% acetic acid in water (v/v) or 20 mM borate buffer adjusted to pH 8.0.

Quartz substrates used for device fabrication were 4 in x 4 in x 2.2 mm (l x w x h) grade CG wafers coated with a 1200 Å low reflectivity chrome layer and a 5300 Å layer of AZ 1518 photoresist (Telic, Valencia, CA).

4.2.2 Microchip Fabrication

The top substrate of the microfluidic chip was etched in a channel pattern and used for fluid control, while the bottom substrate served as a base layer on which electrodes were fabricated. The chips were made from photoresist/chrome coated quartz plates (Telic, Valencia, CA), which were cut into 1 in x 2 in substrates using a Basic Dicer II (Dicing Technology, Longwood, FL). A photomask with the channel layout was designed using TurboCAD v. 9.2 Student Edition (Novato, CA). The completed designs were sent to The Photoplot Store (Colorado Springs, CO) for printing on a mylar film base with an Accumax ARD7 emulsion layer photoplotter (Kodak, Rochester, NY). The mask was placed emulsion side down directly onto the substrate surface, and a 4 in x 4 in quartz blank was placed over it to ensure good contact between the two. The photoresist was exposed through UV flood exposure with a J200 UV Exposure System (OAI, Milpitas, CA) for 65-75 seconds.

Following exposure, the coated substrate was immersed in MF-319 developer (Microchem Corp., Marlboro, MA) for 45-60 seconds to remove the exposed areas. The substrate was removed from the developer, rinsed with deionized water and dried with pressurized nitrogen gas. The design was then checked using an optical microscope to ensure complete development. The chrome in the exposed areas was removed using chrome etchant (Transene, Danvers, MA) for 5-10 minutes. The substrate was then rinsed with deionized water, cleaned with 2% sulfuric acid, rinsed again with deionized water, and dried with pressurized nitrogen gas.

The channels were isotropically etched into a quartz substrate using 5:1 buffered oxide etchant (Transene, Danvers, MA). Throughout the etching process, the channel depth was monitored using a P-15 profilometer (KLA Tencor, San Jose, CA). The etching process was halted before each check by rinsing in deionized water, cleaning with 2% sulfuric acid to remove residue from the channel surface, rinsing again with deionized water, and drying with pressurized nitrogen gas. Upon reaching the desired depth, the substrate was painted with a thick layer of S1813 photoresist to protect the etched channels. Access holes were drilled at the end of each channel segment using a MB 1000-1 powder blaster (Comco, Inc., Burbank, CA) set to make holes 1-2 mm in diameter. The powder blaster was also used to cut away excess substrate to access the electrode pads once the chip was bonded. The photoresist was then removed with acetone, and the remaining chrome removed with chrome etchant.

The substrate for the electrodes was stripped of photoresist and the chrome layer before applying a fresh layer of S1813 photoresist using a Model 6700 Spincoater (Specialty Coating Systems, Indianapolis, IN). The designs for the electrodes were patterned and etched to 100 nm using the procedure described for the channel fabrication. The metal thin

films composing the electrodes were applied using a Model IBSe Ion Beam Deposition System (South Bay Technologies, San Clemente, CA). A 30 nm thick adhesive layer of chrome (Cr) or titanium (Ti) was applied followed by a 70 nm layer of platinum (Pt). The etching step prior to sputtering acted to embed the metal, resulting in electrodes that were flush with the substrate surface. For all photothermal chips, electrodes were 50 μm wide with a 100 μm gap and were arranged in a three-electrode anti-parallel geometry.

Each substrate was immersed in Nanostrip 2x (Cyantek Corperation, Fremont, CA) for up to 15 min in order to remove any remaining organic residue on the surfaces in preparation for bonding. After rinsing with deionized water, the substrates were sonicated in a 2% Contrad 70 solution for 10 minutes before rinseing again. A hydrolysis bath composed of two parts water, two parts 30% ammonium hydroxide, and one part 30% hydrogen peroxide was prepared and heated to 65-70°C. The substrates were immersed in the hydrolysis bath for 10-15 minutes to activate the quartz surfaces. They were then rinsed with deionized water and sonicated for an additional 10 minutes. After removing from sonication, the electrode substrate was held face up, and deionized water was pooled over its surface. The channel substrate was laid over the electrodes, and the excess water was removed. The channel and electrodes were carefully aligned under an optical microscope, and the substrates were clamped together. The chip was placed in a convection oven set to 95°C to evaporate the remaining water. After 5 minutes, the chip was removed from the oven and examined for good contact around the microfabricated features. Poorly bonded areas were evident through the appearance of interference patterns. If good bonding was observed, the chip was placed back into the 95° oven for an additional 10-20 minutes. The device was then placed into a furnace (Lindberg/Blue, Watertown, WI) for the final bake. The furnace program was set to

ramp from ambient temperature to 90°C over 10 minutes and hold at 90°C for 2 hours to ensure removal of any remaining water. The temperature was then increased to 200°C over 2 hours, held for 1 hour, and ramped to 550°C over 2 hours. The furnace was held at 550°C for 10 hours, after which it was cooled to 95°C over 2 hours. Once bonding was completed, cloning cylinders were applied over the access holes using a UV curable optical adhesive. To prevent fluid leakage through any gaps created by the metal film, a small amount of epoxy was applied at the point the electrodes emerged from under the channel substrate.

4.2.3 Channel Surface Modification

Initial measurements for the laser modulation frequency studies were performed using a chip identical to those described in Chapter 3. The remaining experiments were done with the modified design that placed the detection electrodes in an essentially field free region and pumped fluid with pressure induced by opposing electroosmotic flow from two channels. PolyE-323 was used to add a positively charged surface coating to specific channels in these electroosmotic pumping microchips. Scott Mellors, Ph.D. in the Ramsey research group in the Department of Chemistry at the University of North Carolina at Chapel Hill synthesized the polymer following the procedure described by Hardenbourg et al.[24,25] Equimolar amounts of 1,2-bis(3-aminopropylamino)ethane and epichlorohydrine were combined in 20 mL of deionized water while stirring at room temperature. The flask was then sealed and continuously stirred at room temperature for 48 hours until the reaction mixture thickened. The mixture was diluted to five times the original volume, and the equilibration reaction was continued for 1 week. The finished polymer solution was stored at 8°C.

Prior to coating, all channels were flushed with 1N sodium hydroxide for 3 minutes to clean and hydrolyze the surface. The channels were then rinsed for 5 minutes with deionized water. Reservoirs for the channels that would not be coated were filled with deionized water, and the reservoirs for the channels to be coated channels were filled with a 15% (by mass) solution of PolyE-323 adjusted to pH 7 with 1 M acetic acid. Vacuum was applied to the separation channel end, and the solutions were flushed through the channels for approximately 1 hour. The channels were then flushed with 50 mM ammonium acetate or deionized water for 5 minutes to remove excess polymer. At this point, the uncoated channels were rinsed with NaOH and deionized water to remove any polymer that had diffused into them, and the chip was flushed with the desired running buffer. A schematic diagram of the coated chip outlining the fluid flow and electric field is shown in Figure 4-1.

4.2.4 Electrophoresis Setup

An in-house built power supply with four high voltage output modules (10A12-P4 maximum +4 kV or 25A12-N4 maximum -10 kV modules, UltraVolt, Ronkonkoma, NY) was used to initiate electrokinetic flow. Platinum wires were used to apply the voltages to fluid reservoirs and controlled through the analog output of a USB-6229 DAQ board (National Instruments, Austin, TX) by custom software written in LabVIEW ((National Instruments, Austin, TX). Appropriate running voltages were determined using a solution of rhodamine B or fluorescein in the running buffer of the sample reservoir. Gated injections[26] were performed by altering the applied voltages to force fluid from the sample reservoir to flow into the separation channel. The fluid flow was viewed through a TE300 inverted

microscope (Nikon, Melville, NY) equipped with a 20X objective, a high pressure mercury lamp, and a NTE/CCD-512-EBFT camera (Roper Scientific, Trenton, NJ).

4.2.5 Electronic Setup

A diagram of the photothermal system is shown in Figure 4-2. The output of two DS345 digital function generators (Stanford Research Systems, Sunnyvale, CA) were applied to the excitation and reference electrodes in order to provide the AC excitation signal. The two function generators were set in a master-slave configuration, using the 10 MHz output of one as the time base of the other. The phase and voltage were adjusted in order to balance the function generators precisely 180° out of phase with each other, using destructive interference to provide zero background conductivity at the detection electrode. The excitation signal passed through a 3 kV, 100 pF radial disc capacitor (Panasonic-ECG, Secaucus, NJ) prior to and after the detection cell. This isolates the excitation electronics from the DC electrophoresis running voltage. Connections to the microchip electrode pads were made with an aluminum pad connected to a 316 stainless steel compression spring (Small Parts Inc., Miami Lakes, FL), which was soldered to the end of a banana connection in an in-house machined polycarbonate microchip holder mounted on an x-y-z translational stage. Signal from the detection electrode was amplified via an OPA602 operational amplifier (Texas Instruments, Dallas, TX) in a current-to-voltage circuit with a 1 MΩ feedback resistor (Multicomp, Chicago, IL), thus providing a total gain of 10^6 V/A. Surface-mounted 1000 pF capacitors (Newark Electronics, Chicago, IL) added to the circuit removed any high frequency noise from the power supply or feedback loop of the operational amplifier. A grounded aluminum box provided shielding for the electronic circuit. A Model

1301 Power Supply (Global Specialties, New Haven, CT) at ±15 V provided power for the operational amplifier.

The output from the chip was further amplified and filtered with two SR810 digital lock-in amplifiers (Stanford Research Systems, Sunnyvale, CA) arranged in series. The first lock-in amplifier was referenced to the master DS345 function generator and gives the standard conductivity signal for reference purposes. The output from this lock-in was then input to the second lock-in amplifier, which was referenced to the optical modulation frequency using the "*f*" output of a MC1000A Optical Chopper System (ThorLabs, Newton, New Jersey). The first lock-in was set to have a 1 ms time constant with a 24 dB/octave slope (bandwidth = 78 Hz) with AC coupling, and the second lock-in amplifier was set to have a 100 ms time constant with a 24 dB/octave slope (bandwidth = 0.78 Hz) with DC coupling. Line and 2x line filters were used on both lock-in amplifiers. The sensitivity was set at 1 mV for the first lock-in during all experiments and varied for the second to maximize photothermal sensitivity.

Data collection and control of both the function generators and the lock-in amplifiers were maintained with a USB-6229 DAQ card (National Instruments, Austin, TX) and custom software written in LabVIEW (National Instruments, Austin, TX) on a personal computer. Data analysis was performed using Igor Pro (Wavemetrics, Lake Oswego, OR).

4.3.6 Optical setup

Photothermal excitation was provided by a Verdi 532 nm laser with an attached MBD266 doubler (Coherent, Santa Clara, CA) to provide a beam of 266 nm UV light. A beam splitter prior to the doubler was used to moderate the total input to the MBD266. The

maximum UV power used in these experiments was approximately 500 mW incident on the chip. The beam was modulated using a MC1000A Optical Chopper System with a 2-slot blade (ThorLabs, Newton, New Jersey), which provides frequencies between 1 Hz and 99 Hz. The beam was cleaned with a spatial filter consisting of an F/5 singlet lens, a 100 μm pinhole (Melles Griot, Albuquerque, NM), and a F/2 singlet lens. A mirror with UV-enhanced reflective metal coating was used to direct the beam up through a fused silica singlet lens to the microfluidic chip. The elliptical beam was focused to a spot size of about 20 μm x 70 μm at the microchip channel, and was oriented such that the longest dimension was parallel to the electrode (Figure 4-3). All lenses and mirrors were fabricated of fused silica and intended for UV light manipulation (ThorLabs, Newton, NJ). The mirror was rated to reflect approximately 80% of the incident light at 266 nm wavelength. Positioning of the beam in relation to the microchip electrodes was observed using a PL-A741 machine vision camera (PixeLINK, Ottawa, ON). To provide additional focusing and reduce the intensity of the laser light, an F/2 fused silica singlet lens (ThorLabs, Newton, NJ) and two neutral density filters (FNQ057 and FNQ065, Melles Griot, Albuquerque, NM) were placed before the camera.

4.3 Results & Discussion

4.3.1 Laser Modulation Frequency Studies

The laser modulation frequency studies were performed using the standard electrokinetic cross chip used in the studies described in Chapter 3. Modulation frequency studies were performed using 100 mW laser power with 100 kHz and 5 V_{pp} conductivity excitation. The initial measurements were taken with 100 μM guanosine, which was used as

the standard analyte for all detector characterization studies using UV excitation. The photothermal response at higher frequencies behaved as expected given the studies described in Chapter 3. However, a maximum signal was observed at approximately 20 Hz, below which the signal decreased. In Chapter 3, the leveling of the signal at lower frequencies was attributed to heat dissipation, but this would not explain a reduction in signal. The unexpected decrease in the photothermal response using guanosine at lower modulation frequencies led to tests with several other analytes, including fluorescein, caffeine, tryptophan, and BSA. Figure 4-4 shows the photothermal signal and the background noise for 100 μM guanosine at 50 mW and 100 mW, 100 μM fluorescein at 100 mW, and 50 μg/mL BSA at 100 mW plotted with respect to modulation frequency. All analytes studied follow the trends expected at the higher frequencies, but both fluorescein and guanosine (50 mW) also showed decreased signal for frequencies below a certain point. The two guanosine data sets were compared and showed a slight shift in the signal maximum from 20 Hz with 100 mW laser power to approximately 15 Hz at 50 mW laser power, which would be explained by a dependence on the extent of light exposure. Guanosine and fluorescein absorb at 266 nm, and both show a signal maximum near 20 Hz with 100 mW laser power. At the lower frequencies, the response for BSA gradually reached a level point, similar to what was observed in the studies in Chapter 3, but did not decrease. This might be related to the lower concentration of the BSA compared to that of the other analytes, but there was no definitely determined cause for the difference. The decrease in the photothermal signal of the smaller analytes led to initial theories of analyte photobleaching or thermal decomposition by the longer exposure periods to the laser light. Figure 4-4 also shows the noise observed during these studies. The MC1000A Optical Chopper System with a 2 slot blade (ThorLabs,

Newton, New Jersey) was more stable than the SR540 optical chopper (Stanford Research Systems, Sunnyvale, CA) used in the visible wavelength studies, resulting in lower noise values. A modest increase in the noise at lower frequencies produced a maximum signal to noise ratio near 30 Hz for the smaller analytes(Figure 4-5).

To further understand the decreased signal seen at low modulation frequencies in these studies, the output from the first lock-in amplifier, or the conductivity signal, was studied. Figure 4-6 compares the conductivity signal waveform at 5 Hz for 50 μM DABSYL-glucosamine using 50 mW of 488 nm light and 100 μM guanosine using 100 mW of 266 nm light. The conductivity trace shape observed using visible light was the expected square wave shape, as was the background signal for the UV light data. However, while the background conductivity signal using 266 nm light also had this shape, the trace taken as the analyte passed the detector had an irregular shape. It was noted that this irregular shape was present both when the analyte was exposed to the light and when the light was blocked by the chopper blade. Photobleaching might have explained the abnormal shape when the laser was "on," but not when the beam was blocked. Another contributing factor to the irregular shape may have been related to the means of driving fluid flow. The studies in Chapter 3 were performed with pressure driven flow, which relied on an external pressure source to drive the fluid, but these studies used electrokinetic flow, which was sensitive to the conditions within the channel. As the analyte traversed the detection region, the localized temperature changes at the low chopping frequencies may have disrupted the electroosmotic flow and the recorded signal. Figure 4-7 displays plots of conductivity traces at 20, 10, 5, and 1 Hz for 100 μM guanosine. The trace for 20 Hz was similar to the visible light trace, but below 10 Hz, the signal began to deviate from the expected square shape. As a comparison of the signal

shapes for different analytes, Figure 4-8 shows the conductivity trace for 1 Hz modulation of guanosine, fluorescein, caffeine, tryptophan, and BSA. The conductivity trace shape varied with the analyte, indicating the irregularities were contingent on the analyte's behavior. Most of the conductivity traces in Figure 4-8 are relatively similar in shape, but the shape of the fluorescein plot was slightly different, and aside from the initial dip at the front of each phase of the wave, it almost follows the expected shape discussed. The gradual leveling off without the subsequent drop followed the expected pattern of gradual heating until the point where excess heat was being released from the system. The magnitude of this plot is somewhat lower than that of the other four as well, perhaps indicating a relationship between overall temperature changes with each "on" or "off" phase and the irregular shape. The trace for BSA had the lowest amplitude abnormalities, possibly explaining why it best fits the frequency-signal pattern observed in Chapter 3. Despite the possible explanations, no precise cause of the irregular behavior was determined.

4.3.2 Laser Power Studies

All subsequent studies were performed using the microchip design incorporating pressure driven flow through the detection region (Figure 4-9). Previous experimentation has shown a linear increase in photothermal signal with increasing laser power input (Chapter 3). However, these studies have been limited to incident laser powers of less than 100 mW due to limitations with the lasers used. Figure 4-10 displays the signal response of a 100 μM sample of guanosine at powers up to 500 mW. While the plot appears linear at the lower powers, the overall result is a non-linear increase in signal with increasing laser power. This may indicate that the chip itself was being heated at the higher powers. Despite the high

energy input, no indication of microchip breakdown or solution volatilization was observed. The background noise was also found to increase at the higher powers, probably due to slight light scatter, producing a curve in the signal to noise plot (Figure 4-11). Although higher laser powers did produce better signal to noise values, a lower power of 200 mW was chosen as the standard for other experiments in order to prolong the lifetime of the optics in the frequency doubling module.

To demonstrate the importance of a stable laser source, the laser power plots in Figure 4-12 were taken using an older model MBD266 that was rated to a maximum 2 W input from the Verdi laser system. The Verdi laser, which is most stable above 50% of its maximum power, was restricted to a less stable output, and inputs to the MBD266 that produced outputs of above 200 mW tended to overload its internal sensors. This instability also resulted in noise values approximately 70% higher than what was seen when using the newer, higher rated MBD266 used to collect all other data presented here. The data for Figure 4-12 was taken using 100 μM fluorescein as the analyte, which absorbs similarly to guanosine at 266nm, using 20 Hz modulation and an excitation signal of 100 kHz and 5 V_{pp}.

4.3.3 Separation Field Studies

Basic electrophoretic theory states that the separation efficiency can be increased by increasing the electrophoretic mobility and separation speed, since the primary factor in decreasing resolution is axial diffusion.[4] Previous studies using the standard cross-channel design placed the detection electrodes within the field produced by the separation voltage. If too high, the voltage drop across the metal films of the electrodes could result in chrome oxidation or bubble formation due to electrolysis, both of which quickly destroy the

electrodes. Thus, the applied field strength had to be limited to 200 V/cm or lower. The electroosmotic pumping design, which makes use of opposing electroosmotic flow at the junction of two channels to force fluid into a third, provided a convenient field-free region in which to place the detection electrodes. As a result, higher field strengths could be applied without fear of damaging the electrodes through electrolysis.

Figure 4-13 shows the separation of three simple analytes at increasing field strength. All experiments were conducted using 200 mW laser light modulated at 20 Hz modulation and a 100 kHz, 5 V_{pp} conductivity excitation signal. The cross for gated injections and the 13.5 cm long separation channel were coated with PolyE-323, and the side channel was left bare. The injection length for each run was varied in order to inject the same amount of sample. Background noise was found to increase linearly with increasing field strength (Table 4-1), and a slight decrease in peak resolution was observed at the higher applied voltages. One contributing factor to the increased noise and background and the decreased resolution may have been Joule (resistive) heating.[27] The increased noise may have also been related to instabilities in the high voltage modules, since, although the electrodes were in a nominally field free region, some of electric field did extend into the detection channel. As with other photothermally detected separations, the optimal separation field strength will be contingent on the desired resolution, detection limits, and time constraints. For the purposes of these studies, an electric field strength of approximately 300 mV/cm was chosen as the standard.

4.3.4 Limit of Detection Studies

The detection limits for guanosine and BSA were studied as models for detection of a simple molecule and an intact protein, respectively. All measurements were taken using 200 mW laser power modulated at 20 Hz, a 300 V/cm separation field, and a 100 kHz, 5 V_{pp} conductivity excitation signal. Five second injections were performed to insert a front of analyte into the separation channel, creating a flat-topped peak for precise measurement. Signal to noise ratio plots for both analytes are shown in Figure 4-14. A series of analyte solutions with concentrations from 1-100 μM were used for guanosine. The concentration range studied for BSA was between 1 and 50 μg/mL (approximately 14 nM to 700 nM). Above this concentration, the photothermal response for BSA was no longer linear. The limit of detection at a signal to noise ratio equal to 3 was calculated to be 150 nM for guanosine and 230 ng/mL (approximately 3.3 nM) for BSA. It should be noted that this detection limit was obtained at 266 nm, which is not an optimal absorbance wavelength for BSA. A wavelength of 280 nm is more often used for absorbance detection of proteins as it is near the peak absorbance of the aromatic amino acids tryptophan, tyrosine, and phenylalanine.[28]

To compare the detection limit of guanosine to a conventional UV/Vis spectrophotometer, a simple calculation using Beer's Law ($A=\epsilon bc$) can be performed. Assuming a path length of 30 μm, the channel depth, and using the molar absorptivity values for guanosine at 266 nm (12,100 M^{-1} cm^{-1}), the absorbance would be equivalent to approximately 5.6 μAbs. These limit of detection values are comparable to values for DABSYL-glucosamine at 488 nM using the 100 μM gap electrodes, taking into account the slightly higher background noise (2-3 times that observed with the visible laser) associated

with the UV laser. Better laser focusing with a UV transparent microscope objective rather than the current singlet lens and closer spaced electrodes could further improve the detection limits.

4.3.5 Native Analyte Separations

Several electrophoretic separations were performed using a long-channel (13.5 cm) electroosmotic pumping chip. These long channels were fabricated with a serpentine channel design with asymmetric turns as described by Ramsey et al.[20] When etched, the main channels were 125 μm wide and tapered to 85 μm in the turns. The main channels were separated by 430 μm, and the turns had an inner diameter of 520 μm. A separation of 100 μM uracil, 50 μM guanosine, and 100 μM tryptophan in 20 mM borate buffer was done with a 300 V/cm separation field, 200 mW laser light modulated at 20 Hz, and 100 kHz, 5 V_{pp} conductivity excitation signal (Figure 4-15). The separation of a 1 second injection displayed baseline resolution between uracil and guanosine and partial resolution of guanosine and tryptophan. Uracil was selected as the dead time marker for the system, and eluted 71.9 seconds into the run for the 13.7 cm channel, indicating an electroosmotic flow rate of 0.19 cm/s. Assuming a rectangular cross section of 30 μm x 125 μm for the channel, approximately 710 fmol of uracil, 360 fmol guanosine, and 700 fmol tryptophan were injected into the chip. The resulting signal to noise ratios were 370, 780, and 710 for uracil, guanosine, and tryptophan, respectively.

Several oligonucleotide standards were obtained from Protea Biosciences, Inc. (Morgantown, WV) in order to demonstrate the applicability to a more real-world sample. The samples were intended to be used as mass spectrometer standards, and were rated to be

highly pure. Sequences for the standards are shown in Table 4-2. Individual 1 nmol samples were each reconstituted in 500 μL of borate buffer to provide a concentration of 2 μM for each analyte. A 2 μM sample of guanosine was used as a reference to determine detector sensitivity. An overlay of 1 second injections of individual analytes is shown in Figure 4-16. The resulting "separation" demonstrated near baseline resolution for all six analytes. The downward spike at 62 seconds was caused by the presence of excess salts from the analyte samples and marks the separation dead time. Using that time to calculate the volume of sample solution injected (~ 8 nL), each peak represents approximately 20 fmol of analyte. The elution times, peak heights, peak areas, signal to noise ratios, and estimated limits of detection (LOD) are reported in Table 4-3. The estimated LODs were calculated assuming a limiting S/N equal to 3. A separation of the combined six analytes was attempted, but interactions among the single-stranded oligonucleotides prevented resolution of all but guanosine and the 5-base standard.

4.4 Conclusions

Further modification and optimization of the photothermal conductivity detection microdevice and its applications were discussed in this chapter. Addition of a side channel prior to the detection region and positive surface coating on either the main channels or the side channel (the opposite channel being bare silica) caused electroosmotically generated pressure that induced flow through the detection region. Since the detection channel exit was floating electrically, no DC voltages were dropped across the electrodes. Without the electrophoresis voltage directly interacting with the electrodes, concerns about metal film oxidation or electrolysis were eliminated. Conversely, the background photothermal signal

and noise recorded by the lock-in amplifiers increased directly with the electric field strength, reducing signal to noise values and resolution in higher separation fields.

Since the detector electronics and the detection cell geometry did not change from the studies in Chapter 3, the electronic behavior was assumed to be the same for detection at 266 nm as that observed in Chapter 3 for 488 nm. The detector response to alterations in laser power and modulation frequency was studied extensively. The relationship between the signal and the laser power was essentially linear, curving slightly at higher laser powers and perhaps indicating increased substrate heating. Photothermal signals for up to 500 mW were recorded, and no chip breakdown or solution volatilization was observed.

Altering the modulation frequency via the chopper produced the expected results for frequencies above 30 Hz, but a maximum signal output was observed at 20 Hz for guanosine, below which the signal decreased. The behavior of several other native analytes was observed at lower frequencies, and the maximum signal was found to be dependent on the analyte. The reduction in signal for several analytes below 20 Hz was attributed to an irregular wave shape in the conductivity trace. Photobleaching or thermal decomposition was the suspected culprit, but neither explained the waveform's nearly symmetrical shape. The magnitude of the temperature change may have induced convection or affected the electroosmotic flow in the detection region to cause the irregular shape, but no definite cause was determined.

Limits of detection were found to be comparable to those observed for DABSYL-tagged glucosamine under similar conditions using visible light excitation. The limit of detection at a signal to noise ratio equal to 3 was determined to be 150 nM for guanosine and 230 ng/mL (approximately 3.3 nM) for BSA. Using Beer's Law and treating the

photothermal detector as a standard UV/Vis absorbance detector, the absorbance was calculated to be equivalent to approximately 5.6 μAbs for guanosine. This value was slightly higher than the equivalent absorbance values observed with the 488 nm laser, but the higher energy UV laser tended to display more inherent instability, explaining these observations.

The photothermal absorbance detector was also used to observe separations of native analytes. A separation of simple molecules was successful and provided good signal to noise values for femtomolar amounts of analyte. Since the individual nucleotide bases absorbed strongly at 266 nm, a "separation" of several short oligonucleotides was demonstrated. Limits of detection for the individual oligonucleotides were calculated, with the 30-base standard (highest absorbing) having a limit of 23 nM.

These experiments demonstrate the advances in photothermal absorbance detection to this point. The objective of highly sensitive detection of native analytes in a small path length detection cell was achieved, and the detector was fully characterized. Currently, the photothermal detector meets or exceeds the sensitivity of 1-cm path length UV absorbance detectors. All tests run herein were done using basic capillary zone electrophoresis for analyte migration and separation, but countless other applications remain open for exploration. A number of other electrophoresis-based techniques, including capillary gel electrophoresis which would provide separation for larger oligonucleotides than those examined here, could be applied to the device and would benefit from the high sensitivity detection. Application of the conductivity based photothermal absorbance detector to liquid chromatography will be discussed in the next chapter.

4.5 Tables and Figures

Table 4-1: Photothermal background and noise values for a sampling of electrophoretic field strengths on the electroosmotic pumping chip.

Electric field (V/cm)	Injection Time (s)	Photothermal Background (mV)	Noise (μV_{rms})
58	5	13.1	1.6
120	2.5	13.4	2.9
170	1.67	13.5	4.2
290	1	13.9	7.1
410	0.71	14.2	9.9
520	0.56	14.9	13
580	0.5	14.5	14

Table 4-2: Sequences of the oligonucleotide standards

Number of Bases	Sequence
5	AGCTA
10	TCAGTCAACT
15	GTTTCCATTTAGTCA
20	ACATTCTTCATAGCATTTTA
30	CAATCCACTACAACTACATGTGTAACAGAA

Table 4-3: Data for the separation of oligonucleotide standards.

Analyte	Migration Time (s)	Peak Height (mV)	Peak Area (mV·s)	S/N	Estimated LOD (nM)
Guanosine	79.7	0.184	0.311	35	170
5-base	109.4	0.589	1.03	110	55
10-base	123.7	0.871	1.59	160	37
15-base	129.2	1.04	2.08	190	31
20-base	134.5	1.30	2.72	240	25
30-base	146.6	1.39	5.58	260	23

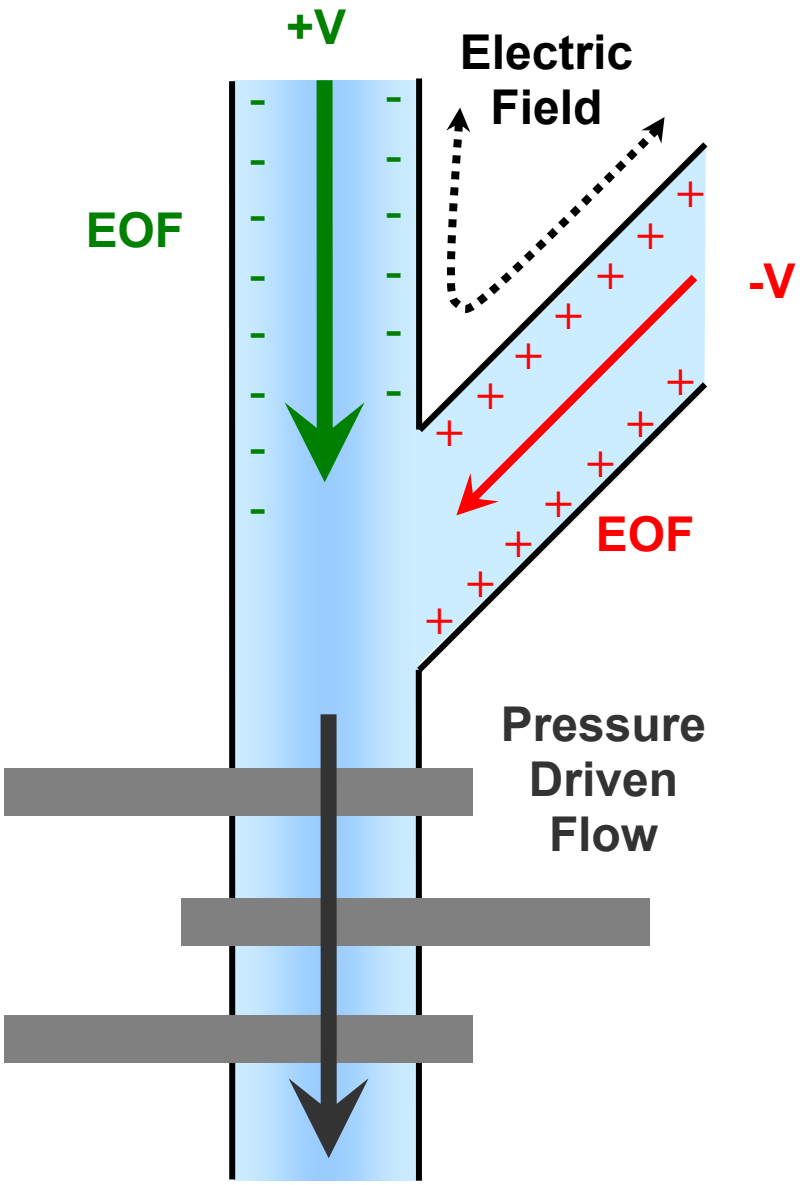

Figure 4-1: Schematic diagram showing the electric field and fluid flow within a microchip making use of opposing electroosmotic flow (EOF) to create pressure driven flow through the detection region.

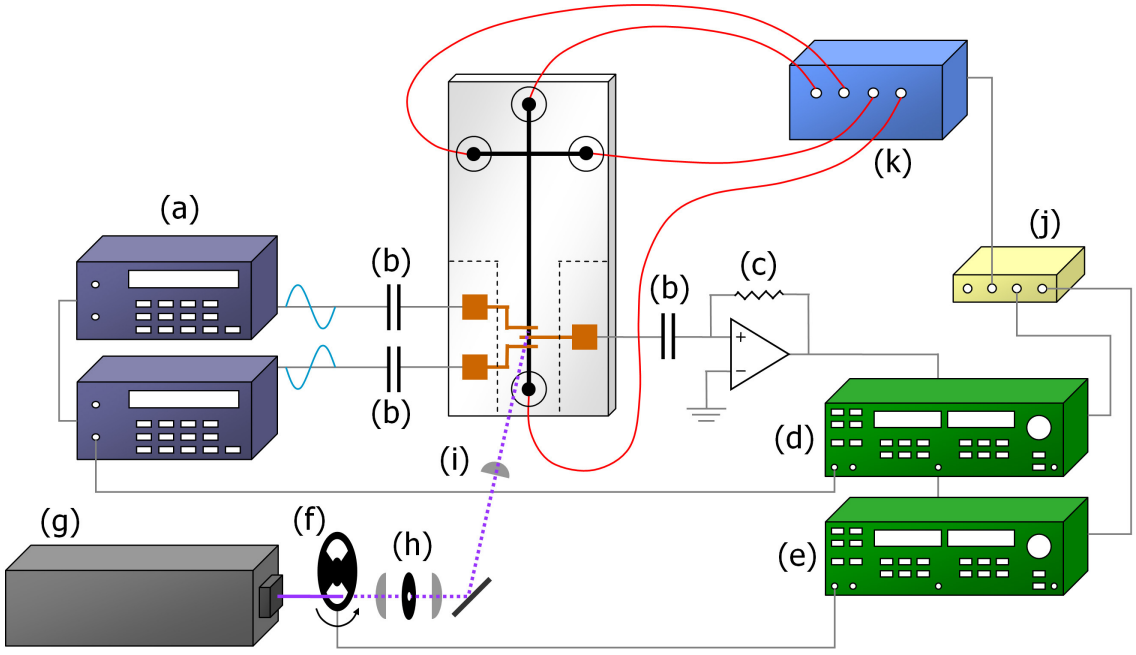

Figure 4-2: Schematic of the microchip photothermal setup, with the microchip containing the separation channels and electrodes shown at the center. Individual components are (a) two phase-locked function generators, (b) high voltage capacitors for isolation of AC components from the DC electrophoretic running voltage, (c) feedback resistor, (d) conductivity lock-in amplifier, and (e) photothermal lock-in amplifier, (f) optical chopper, (g) laser, (h) spatial filter, (i) singlet lens for beam focusing, (j) USB DAQ, and (k) high voltage power supply. The reference for the conductivity lock-in amplifier is supplied by one function generator, and the reference for the photothermal lock-in amplifier is supplied by the optical chopper.

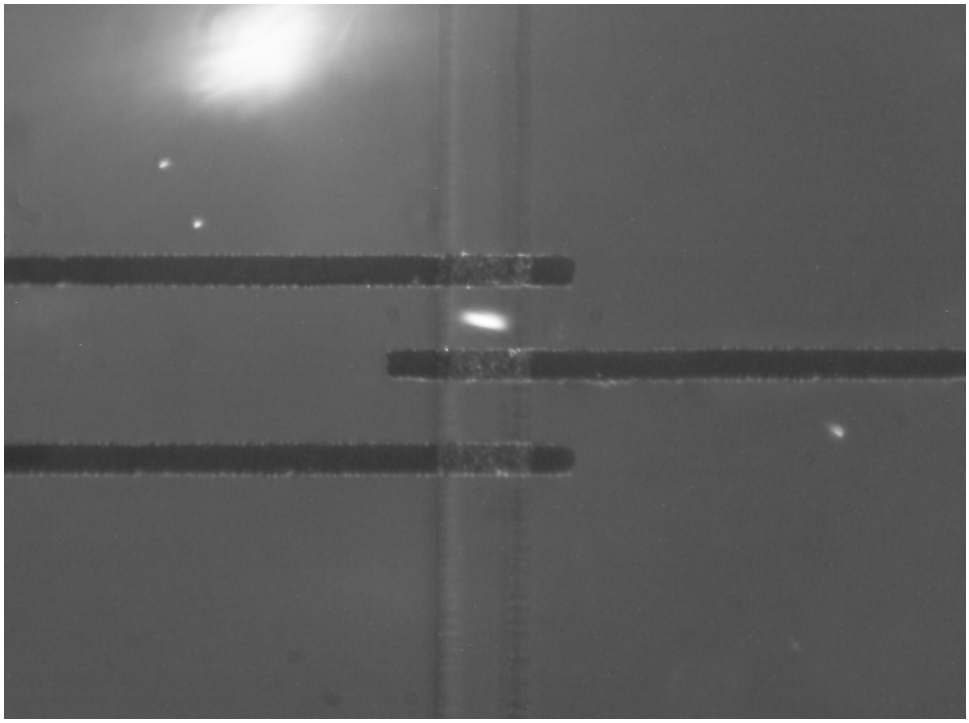

Figure 4-3: Magnified view of the metal electrodes and UV laser spot, which is visible due to fluorescein in the channel. Electrodes are 50 µm wide with a 100 µm gap, and the channel is 125 µm wide.

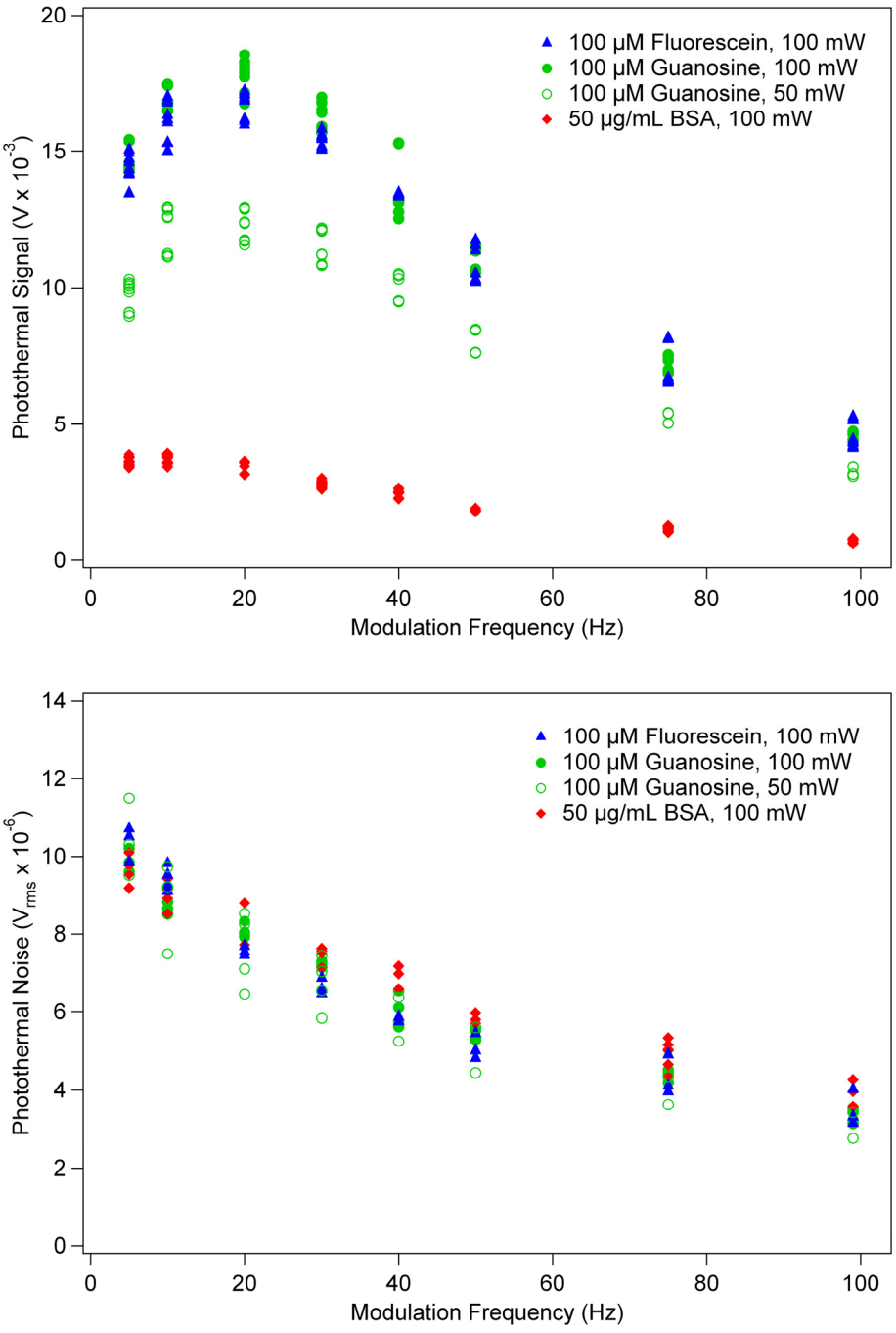

Figure 4-4: The photothermal signal of several analytes (top) and the background noise (bottom) plotted against the laser modulation frequency. The laser power was 50 mW or 100 mW with a 100 kHz, 5 V_{pp} excitation signal.

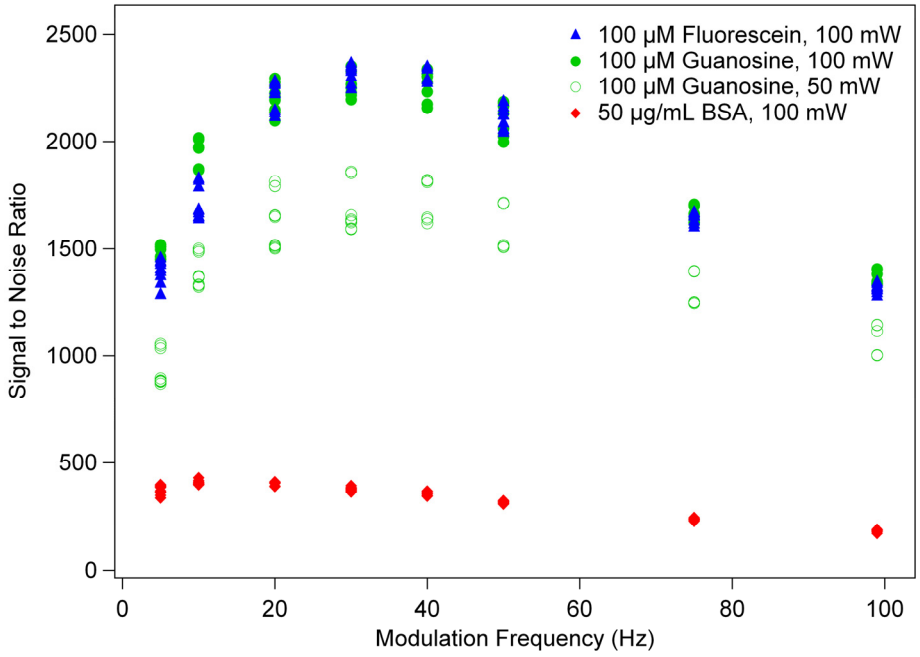

Figure 4-5: The signal to noise ratio of several analytes plotted against laser modulation frequency. The laser power was 50 mW or 100 mW with a 100 kHz, 5 V_{pp} excitation signal.

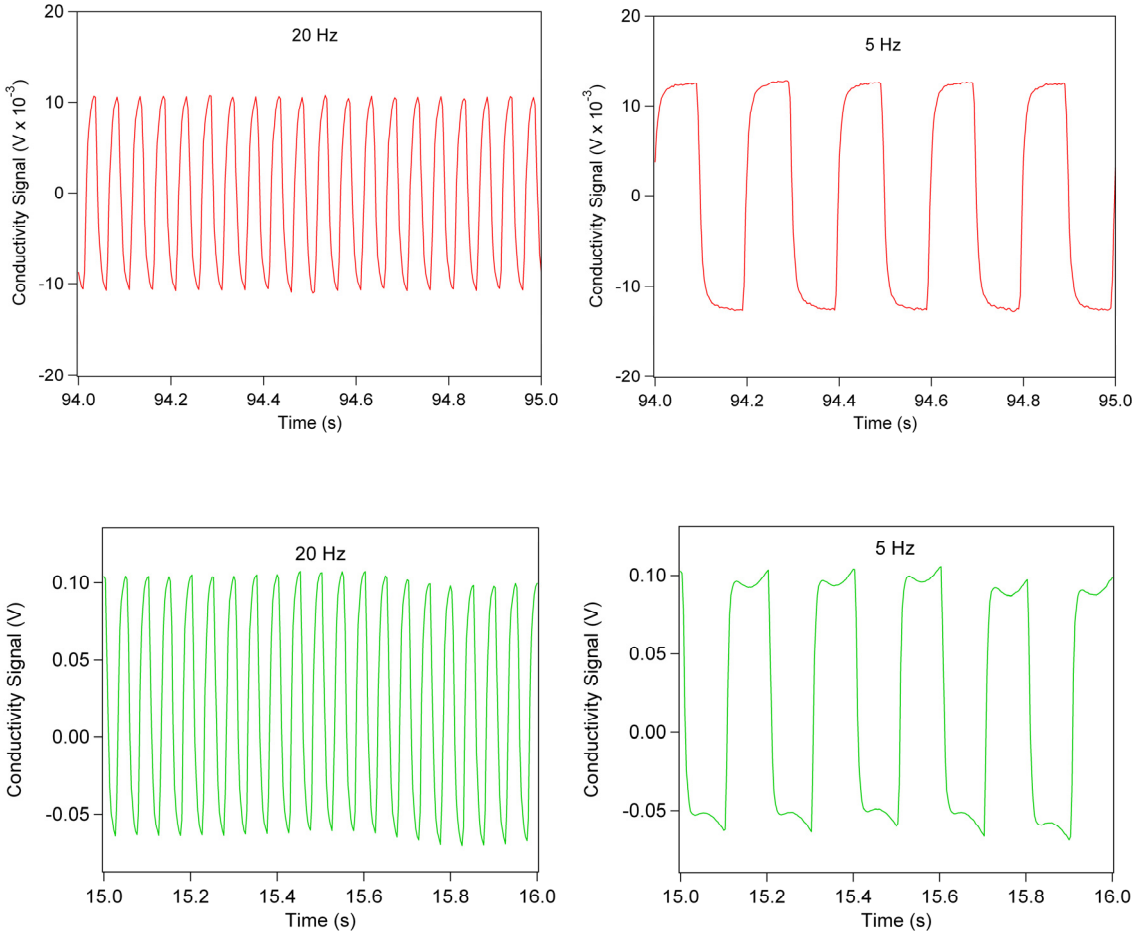

Figure 4-6: Comparison of the conductivity signal waveform at 20 Hz and 5 Hz for (top) 50 µM DABSYL-glucosamine using 50 mW of 488 nm light and (bottom) 100 µM guanosine using 100 mW of 266 nm light.

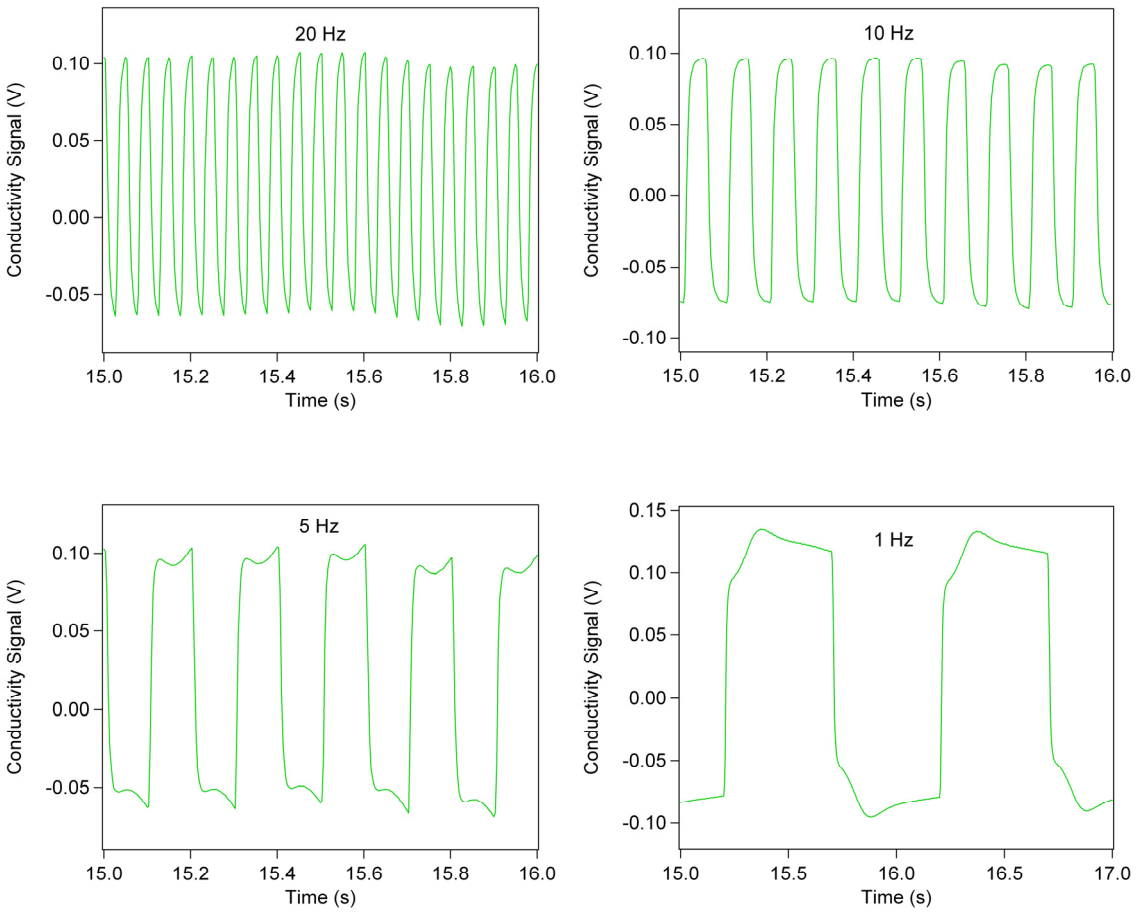

Figure 4-7: The conductivity trace for guanosine at (z) 20, (b) 10, (c) 5, and (d) 1 Hz. The laser power was 100 mW with a 100 kHz, 5 V_{pp} signal.

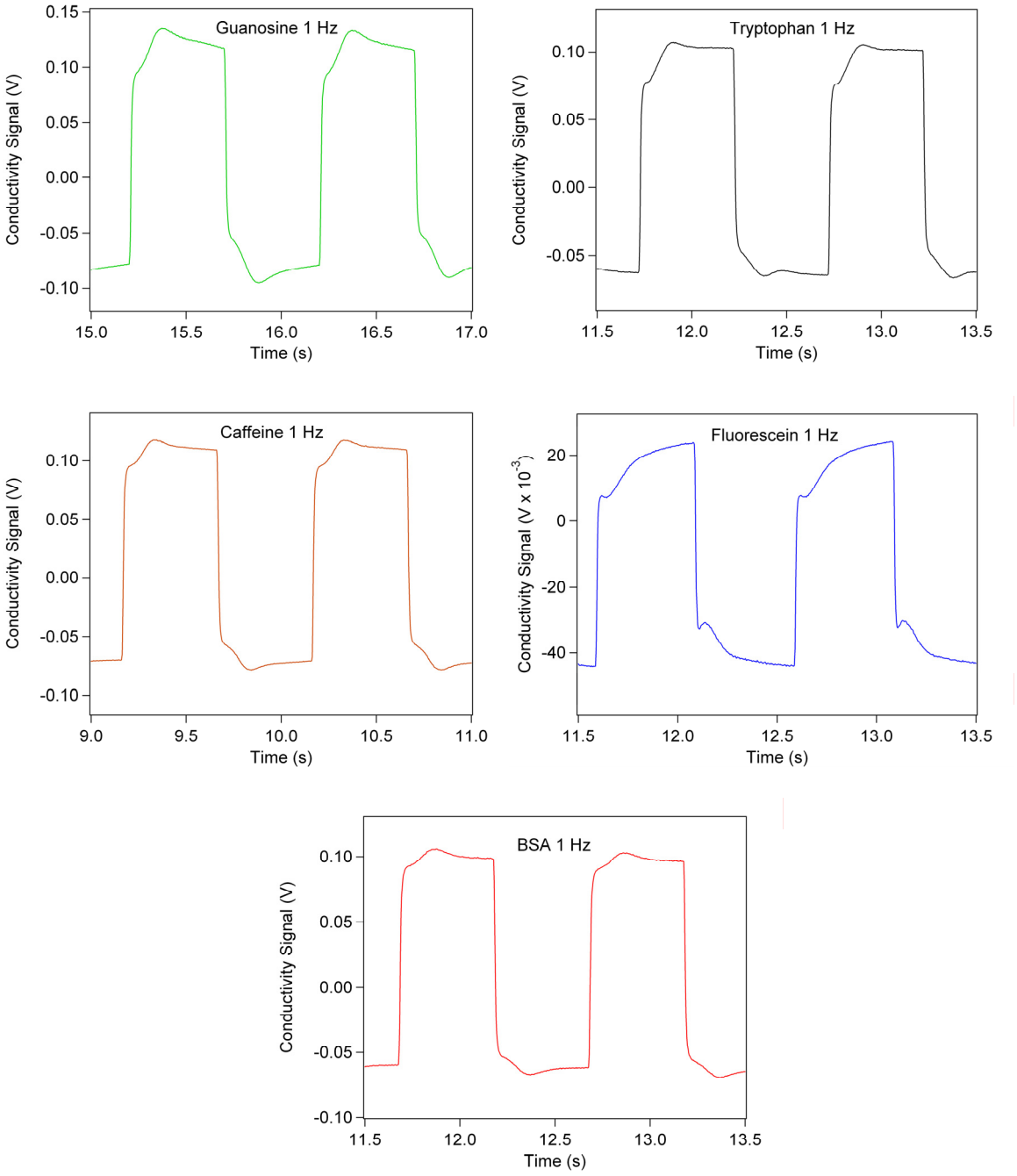

Figure 4-8: The conductivity trace for 1 Hz modulation of guanosine (a), fluorescein (b), caffeine (c), tryptophan (d), and BSA (e). The laser power was 100 mW with a 100 kHz, 5 V_{pp} excitation signal.

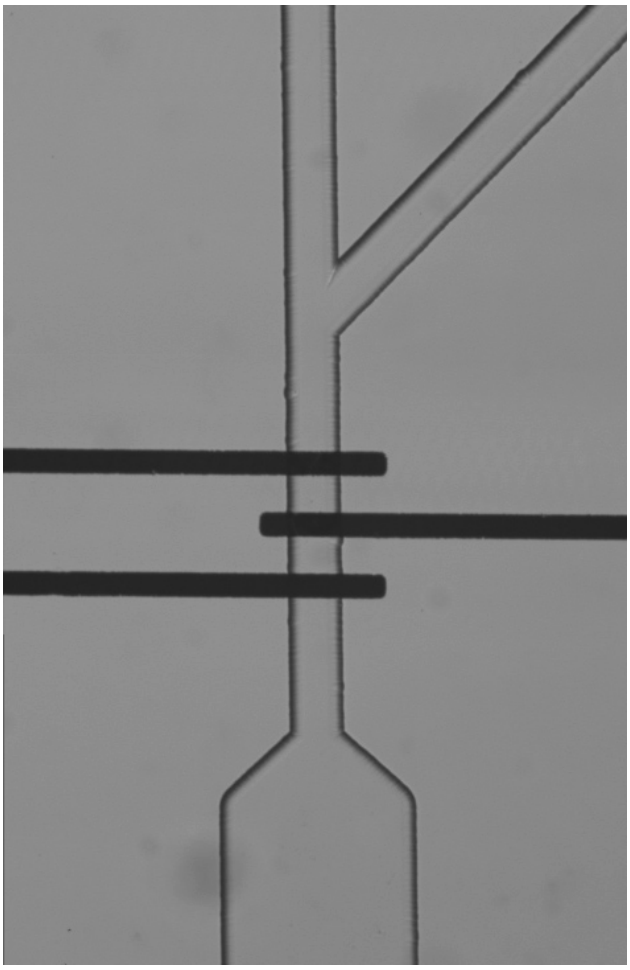

Figure 4-9: Design of the electroosmotic pumping chip. Electroosmotic flow is strong from the separation channel (top) and weak from the side channel. The flowing fluid is forced through the detection region, after which the channel widens to reduce flow resistance.

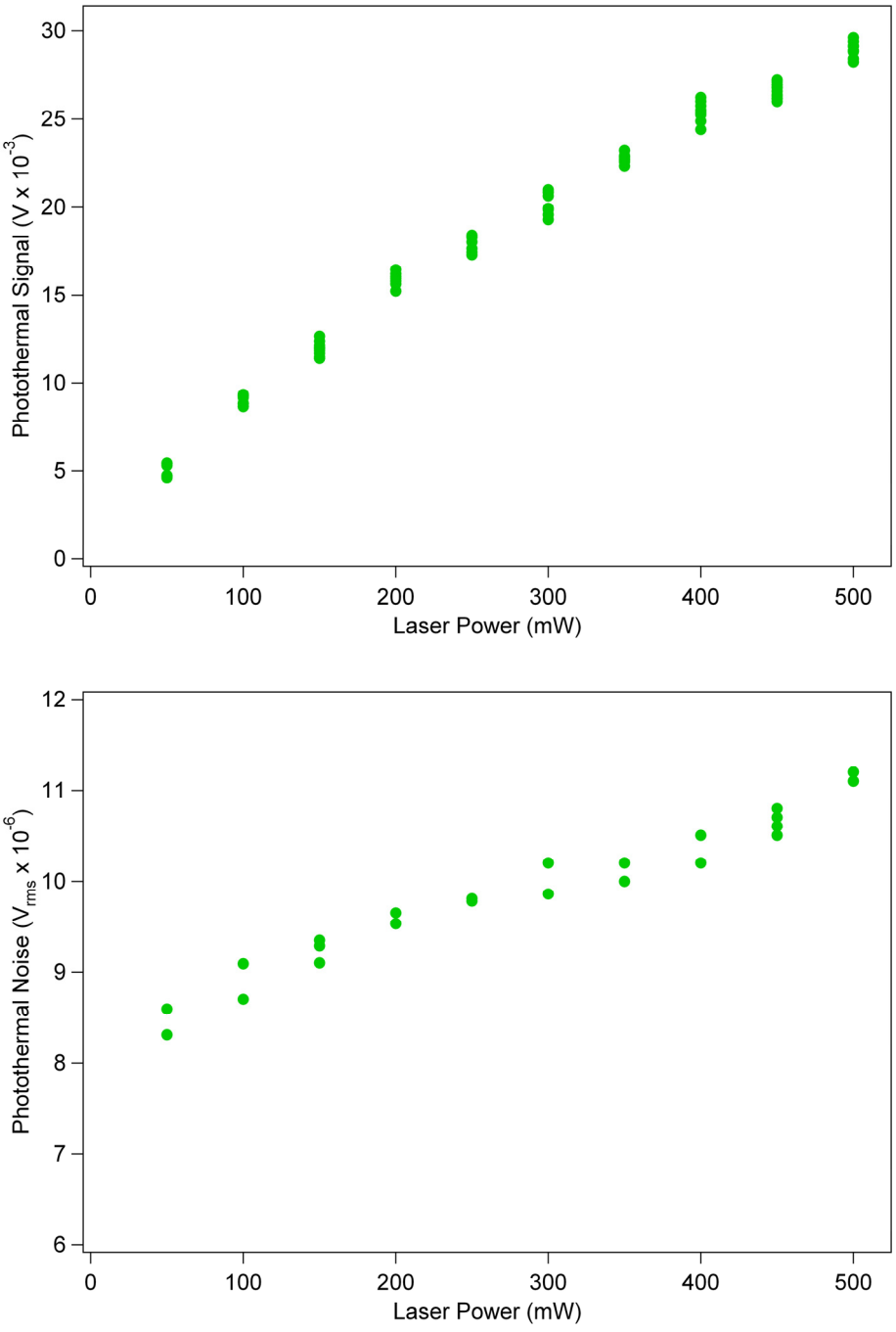

Figure 4-10: The photothermal signal of 100 µM guanosine (top) and the background noise (bottom) plotted against laser power. The laser modulation frequency was 20 Hz with a 100 kHz, 5 V_{pp} excitation signal.

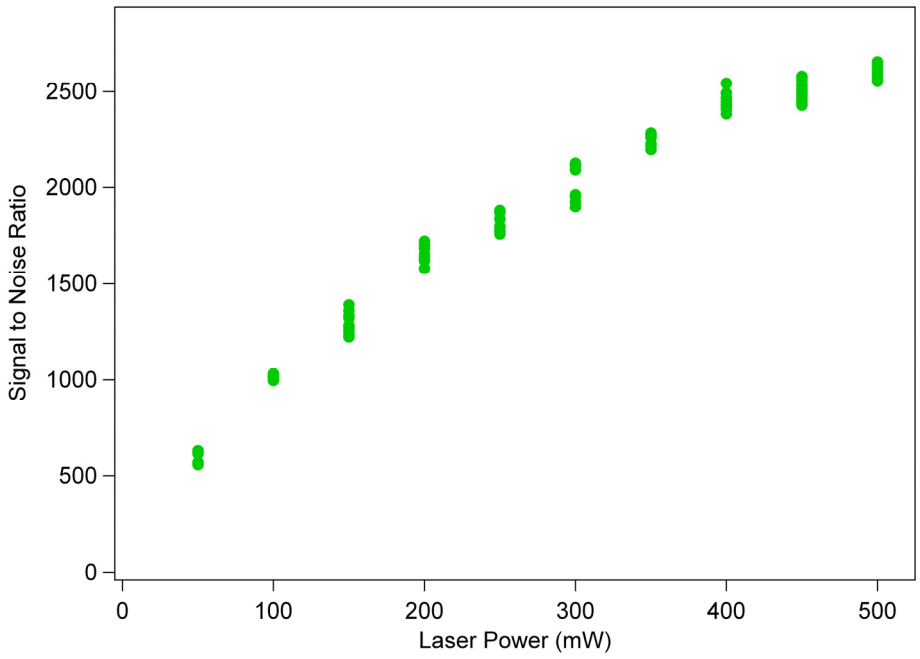

Figure 4-11: The signal to noise ratio of 100 µM guanosine plotted against the laser power. Laser modulation frequency was 20 Hz with a 100 kHz, 5 V_{pp} excitation signal.

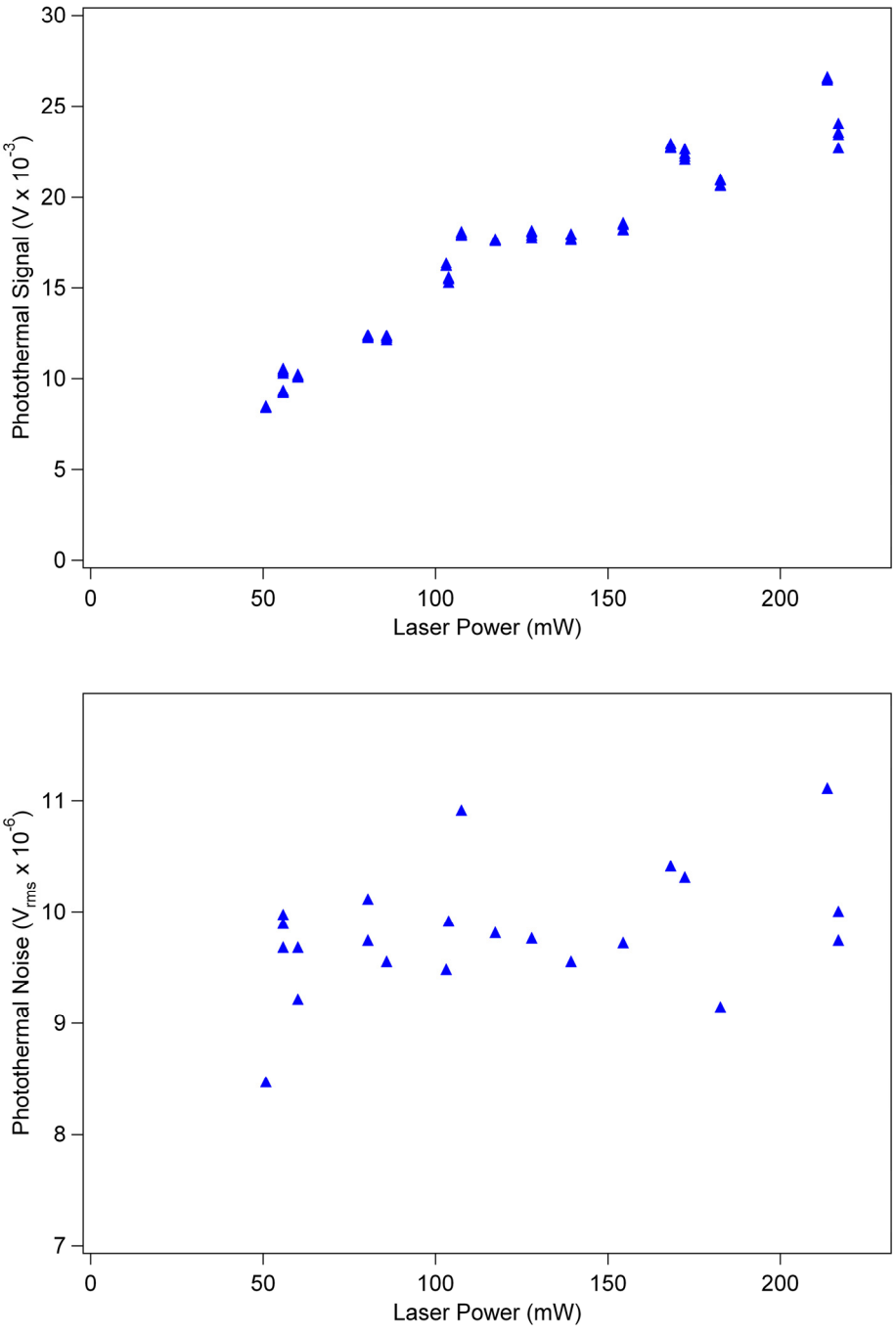

Figure 4-12: The photothermal signal of 100 µM fluorescein (top) and the background noise (bottom) plotted against laser power of an older model MBD266. The scatter in both plots demonstrates the importance of laser stability. The laser modulation frequency was 20 Hz with a 100 kHz, 5 V_{pp} excitation signal.

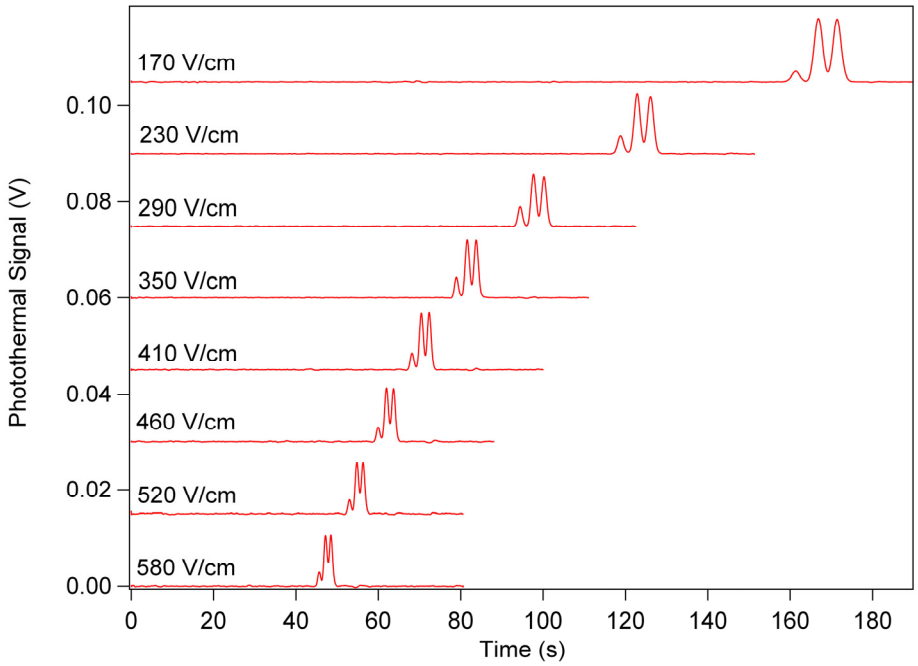

Figure 4-13: A separation of three simple analytes(100 µM uracil, 50 µM guanosine, and 100 µM tryptophan) at the indicated field strengths. Laser power was 200 mW at 20 Hz modulation with a 100 kHz, 5 V_{pp} excitation signal.

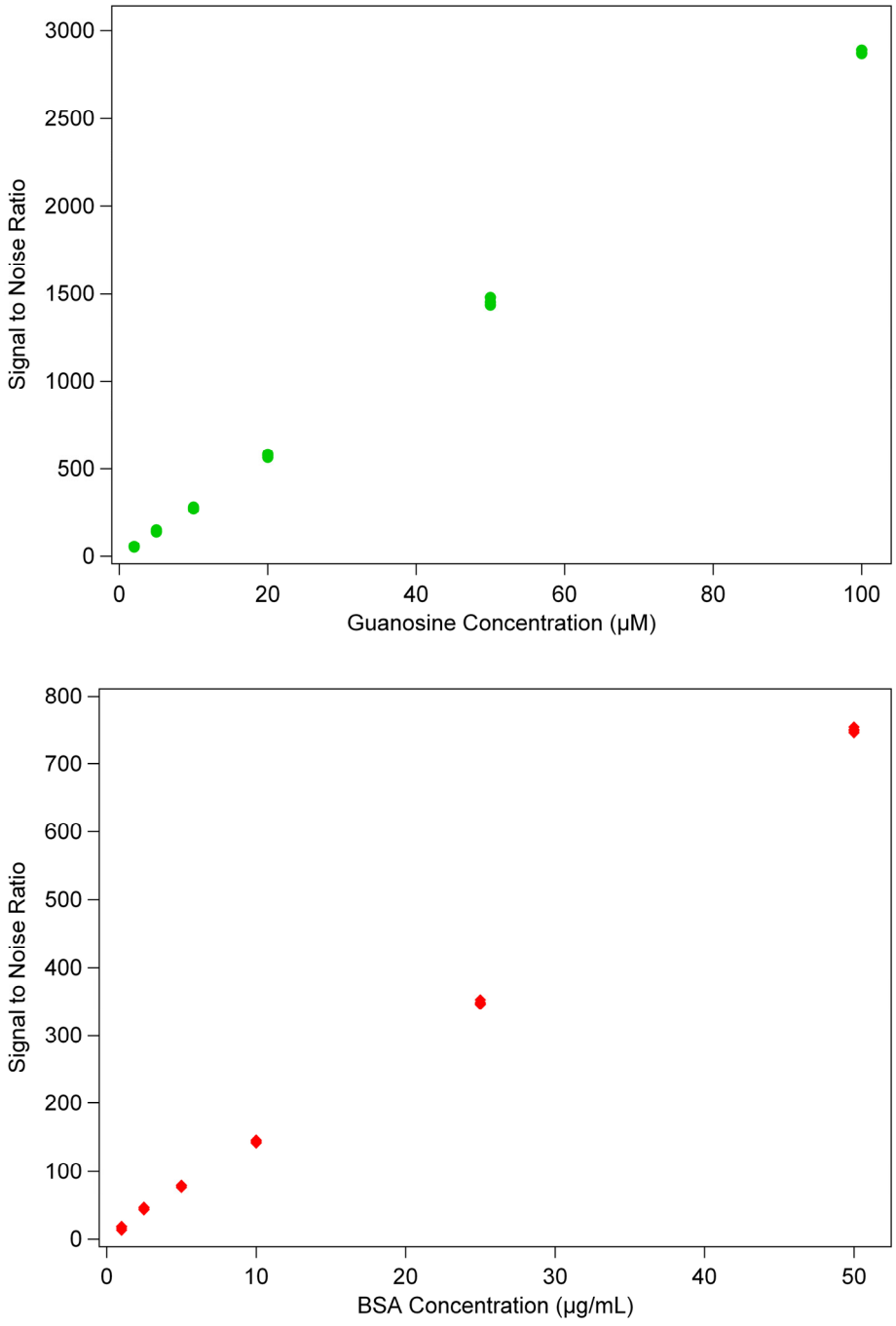

Figure 4-14: Plots of photothermal signal to noise of guanosine (top) and BSA (bottom) with respect to analyte concentration. The laser power was 200 mW at 20 Hz modulation with a 100 kHz, 5 V_{pp} excitation signal. Limits of detection were 150 nM for guanosine and 230 ng/mL (approximately 3.3 nM) for BSA.

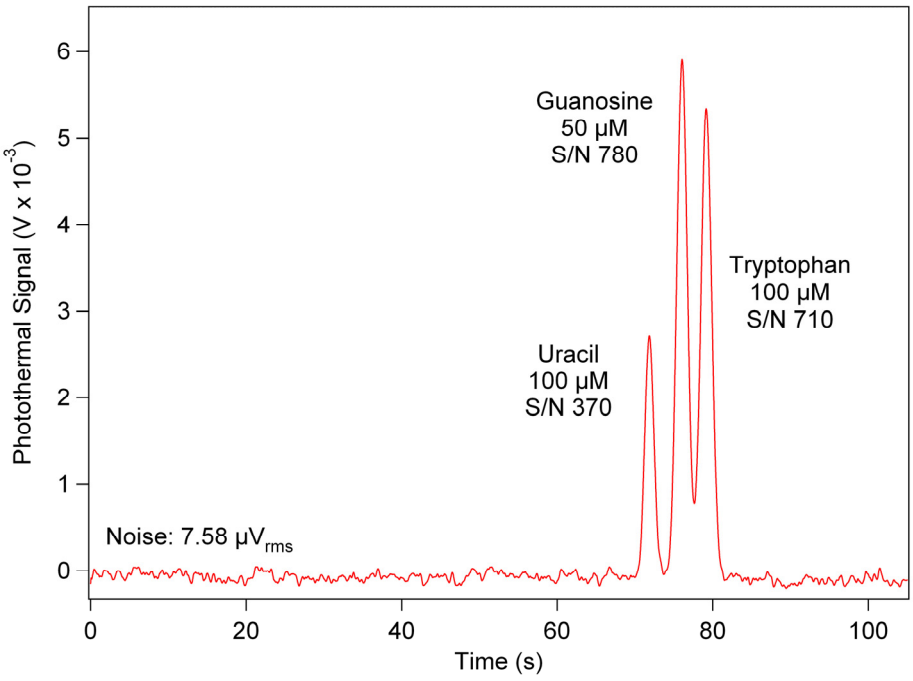

Figure 4-15: A separation of simple native analytes: 100 µM uracil, 50 µM guanosine, and 100 µM tryptophan. Laser power was 200 mW at 20 Hz modulation, using 300 V/cm electric field and 100 kHz, 5 V_{pp} excitation.

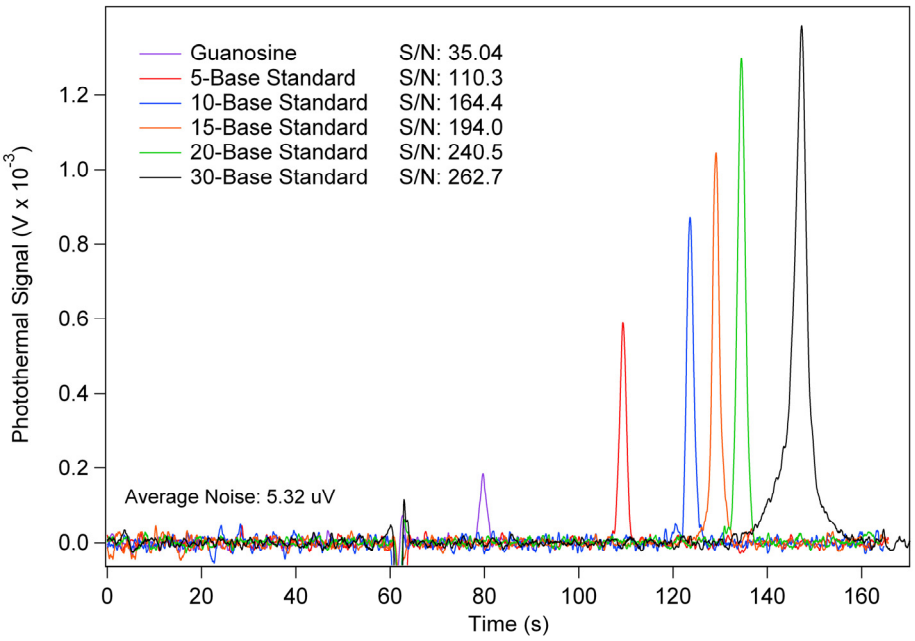

Figure 4-16: Overlaid "separation" of 2 µM concentrations of guanosine and 5 oligonucleotide standards (5, 10, 15, 20, and 30 bases long). The downward spike at 62 seconds indicates the dead time of the system. Laser power was 200 mW at 20 Hz modulation, using 300 V/cm electric field and 100 kHz, 5 V_{pp} excitation.

4.6 References

(1) Lindberg, P.; Hanning, A.; Lindberg, T.; Roeraade, J. *Journal of Chromatography A* **1998**, *809*, 181-189.

(2) Culbertson, C. T.; Jorgenson, J. W. *Journal of Microcolumn Separations* **1999**, *11*, 652-662.

(3) Götz, S.; Karst, U. *Analytical and Bioanalytical Chemistry* **2007**, *387*, 183–192.

(4) Harris, D. C. *Quantitative Chemical Analysis*; 6 ed.; W. H. Freeman and Company: New York, NY, 2003.

(5) Bruin, G. J. M.; Stegeman, G.; Asten, A. C. V.; Xu, X.; Kraak, J. C.; Poppe, H. *Journal of Chromatography* **1991**, *559*, 163-181.

(6) Moring, S. E.; Reel, R. T. *Analytical Chemistry* **1993**, *65*, 3454-3459.

(7) Chervet, J. P.; Soest, R. E. J. V.; Ursem, M. *Journal of Chromatography* **1991**, *543*, 439-449.

(8) Kahle, V. *Biomedical Chromatography* **1999**, *13*, 93–94.

(9) Daridon, A.; Fascio, V.; Lichtenberg, J.; Wütrich, R.; Langen, H.; Verpoorte, E.; Rooij, N. F. d. *Fresenius Journal of Analytical Chemistry* **2001**, *371*, 261–269.

(10) Heiger, D. N.; Kaltenbach, P.; Sievert, H.-J. P. *Electrophoresis* **1994**, *15*, 1234-1247.

(11) Xue, Y.; Yeung, E. S. *Analytical Chemistry* **1994**, *66*, 3575-3580.

(12) Salimi-Moosavi, H.; Jiang, Y.; Lester, L.; McKinnon, G.; Harrison, D. J. *Electrophoresis* **2000**, *21*, 1291-1299.

(13) Wang, T.; Aiken, J. H.; Huie, C. W.; Hartwick, R. A. *Analytical Chemistry* **1991**, *63*, 1372-1376.

(14) Mishra, S. K.; Dasgupta, P. K. *Analytica Chimica Acta* **2007**, *605*, 166-174.

(15) Petersen, N. J.; Mogensen, K. B.; Kutter, J. P. *Electrophoresis* **2002**, *23*, 3528–3536.

(16) Mogensen, K. B.; Eriksson, F.; Gustafsson, O.; Nikolajsen, R. P. H.; Kutter, J. P. *Electrophoresis* **2004**, *25*, 3788–3795.

(17) Mogensen, K. B.; Petersen, N. J.; Hübner, J.; Kutter, J. P. *Electrophoresis* **2001**, *22*, 3930-3938.

(18) Jacobson, S. C.; Hergenroder, R.; Koutny, L. B.; Warmack, R. J.; Ramsey, J. M. *Analytical Chemistry* **1994**, *66*, 1107-1118.

(19) Griffiths, S. K.; Nilson, R. H. *Analytical Chemistry* **2001**, *73*, 272-278.

(20) Ramsey, J. D.; Jacobson, S. C.; Culbertson, C. T.; Ramsey, J. M. *Analytica Chimica Acta* **2003**, *73*, 3758-3764.

(21) Ramsey, R. S.; Ramsey, J. M. *Analytical Chemistry* **1997**, *69*, 1174-1178.

(22) Mellors, J. S.; Gorbounov, V.; Ramsey, R. S.; Ramsey, J. M. *Analytical Chemistry* **2008**, *80*, 6881–6887.

(23) Lazar, I. M.; Ramsey, R. S.; Jacobson, S. C.; Foote, R. S.; Ramsey, J. M. *Journal of Chromatography A* **2000**, *892*, 195-201.

(24) Hardenborg, E.; Zuberovic, A.; Ullsten, S.; Soderberg, L.; Heldin, E.; Markides, K. E. *Journal of Chromatography A* **2003**, *1003*, 217-221.

(25) Ullsten, S.; Zuberovic, A.; Wetterhall, M.; Hardenborg, E.; Markides, K. E.; Bergquist, J. *Electrophoresis* **2004**, *25*, 2090–2099.

(26) Jacobson, S. C.; Koutny, L. B.; Hergenroder, R.; Moore, A. W.; Ramsey, J. M. *Analytical Chemistry* **1994**, *66*, 3472-3476.

(27) Tang, G. Y.; Yan, D. G.; Yang, C.; Gong, H. Q.; Chai, C. J.; Lam, Y. C. *Journal of Physics: Conference Series* **2006**, *34*, 925–930.

(28) Zhu, L.; Lee, C. S.; DeVoe, D. L. *Lab on a Chip* **2006**, *6*, 115–120.

Chapter 5: Photothermal Absorbance Detection for Microfluidic Liquid Chromatography

5.1 Introduction

5.1.1 Basic Liquid Chromatography Theory and Common Detection Methods

High performance liquid chromatography (HPLC) has become arguably the most widely used analytical technique for the separation of complex mixtures. This method has been developed extensively over the last few decades, with most improvements centering on the nature of the liquid chromatography column. Specifically, the spherical particles used to support the stationary phase (SP) have become significantly smaller, with commercially available particles having diameters of a few micrometers or smaller. The reduction in particle size has resulted in significant improvements in efficiency and run time.[1]

The behavior of a liquid chromatography (LC) column is often described in terms of the height equivalent of a theoretical plate, or H. This parameter is calculated from the spatial variance (σ_L^2) of an eluted peak as defined by the peak's width, assuming a Gaussian peak shape, and the length (L) that it travels through the column:

$$H = \frac{\sigma_L^2}{L} \tag{5-1}$$

Therefore, the separation efficiency is defined according to the number of theoretical plates (N), which is equal to the column length divided by the plate height:

$$N = \frac{L}{H} = \frac{L^2}{\sigma_L^2} \tag{5-2}$$

The total variance experienced by a traveling sample peak is caused by a number of independent factors. Variances from independent sources are by definition additive, as are the variables that rely on it. Therefore, the total plate height is defined by the sum of individual variances divided by the column length:

$$H = \frac{\sigma_A^2}{L} + \frac{\sigma_B^2}{L} + \frac{\sigma_C^2}{L} + \ldots = H_A + H_B + H_C + \ldots \quad (5\text{-}3)$$

In general, most of the variance in a LC separation can be defined by three factors based on their dependence on the linear velocity of the mobile phase (u). This reduces equation 5-3 to its more familiar form, the van Deemter equation:

$$H = A + \frac{B}{u} + Cu \quad (5\text{-}4)$$

where *A, B,* and *C* are the van Deemter coefficients. The coefficient *A* is often called the eddy diffusion term and represents the multiple flow paths through which an analyte molecule may move in a packed bed. The coefficient *B* represents the longitudinal diffusion of the analyte within the mobile phase (MP). The coefficient *C* is called the resistance to mass transfer term, and it is defined as all factors that become worse with increased velocity. A plot of the van Deemter equation consists of a curved line that has one minimum, the minimum plate height or H_{min}, representing the highest efficiency of the column when run at the corresponding optimum velocity, u_{opt}.

Unfortunately, the most efficient column is only useful if the efficiency is maintained within the peripheral components necessary for a conventional HPLC system. Dead volume, or the void space within the system, is the primary cause for lost efficiency in a separation. Excess dead volume can lead to dilution of the initial sample or the separated bands, leading to wider analyte bands, inefficient separations, and less sensitive detection. The most

common sources of dead volume include the injection valve, the various fittings and connections between the components, and the detector. These are minimized by the use of low dead volume parts, but are still present.

Detection methods for LC are similar to those discussed in Chapter 1 for use with capillary electrophoresis (CE), with some of the most common being UV/Vis absorbance detection, electrochemical detection, fluorescence detection, and mass spectrometry (MS). Absorbance detection is one of the most common for monitoring peak elution, but requires extended path lengths that can add significant dead volume to a system, reducing resolution and sensitivity. Electrochemical and fluorescence detection are also common and highly sensitive, but as stated in previous chapters, are highly selective and often require analyte tagging. Mass spectrometry, though not as sensitive as electrochemical or fluorescence detection, is one of the most powerful detection techniques as it can provide precise qualitative data about the analyte molecules.

5.1.2 Liquid Chromatography in Microfluidics

Electrophoresis is by far the most common separation method utilized in microfluidic devices due to its simplicity of implementation and high resolution attainable over relatively short column lengths.[2] In comparison, liquid chromatography (LC) is much less prevalent on a microfluidic platform, despite its ubiquitous use in traditional systems. While completing an electrophoretic microchip requires little more than etched channels and a high voltage power supply, the added difficulties of packing a bed of stationary phase (SP) particles in an often complex chip and the relatively large pumps used in LC can make it unappealing.[3]

Despite the additional difficulties of LC microfluidics, the technique is highly useful, and its incorporation into a micro total analysis system (μTAS) has been widely studied.[1,4]

One of the first examples of microchip LC was presented by Manz et al. in 1990.[5] Their design made use of an open-tubular column fabricated into a 5 mm x 5 mm silicon chip and was run using conventional LC pumps and valves. The column itself was a 15 cm long spiral design with a cross section of 6 μm x 2 μm giving a total inner volume on the nanoliter scale. Following etching of the silicon wafer, the surface was treated to create a 30 nm layer of silicon oxide. A conductometric detector was composed of thin film platinum electrodes sputtered onto a glass substrate that acted as the cover plate. The two halves of the device were electrostatically sealed by applying 400°C heat and 0.5 kV for a set period of time. An access hole was drilled through the center of the device to act as a connection point for the external LC components. The performance of the device was not experimentally tested, but had a simulated separation efficiency of 8000 plates with a 1 minute run time or 25,000 plates with a 5 minute run time.

An alternative to traditional liquid chromatography is capillary electrochromatography (CEC).[6] In this technique, electroosmotic flow is used to "pump" the mobile phase through the analytical column, eliminating the need for large, external pumps, valves, and high pressure fittings. The electroosmotic "pump" has the additional advantage of having a virtually flat flow profile as opposed to the parabolic flow profile of pressure driven flow. Such a device also eliminates the need for physical valves, and can be run in the same manner as a device built for electrophoretic separations. Jacobson et al. describe an open channel device that makes use of this technique. The channels were etched to be 5.6 μm deep and 66 μm wide at half the depth, providing a high aspect ratio in order to increase

the surface area for interaction between the octadecylsilane (C18) stationary phase and the mobile phase. The device was used to separate a number of fluorescent dyes, which were monitored via direct fluorescence. Electroosmotic flow rates were studied between 0.13 and 0.78 mm/s in order to determine the fluid flow behavior and band resolution of the system. While some band broadening was observed due to the trapezoidal shape of the channels and the turns required to fit a long channel in the limited area of the chip, plate heights as small as 4.1 μm were acheived for both retained and unretained analytes. This research group modified a version of the device to combine the open channel CEC with on-chip solvent programming.[7] Separations were done under both isocratic and gradient conditions with a high degree of control.

Many microfluidic devices make use of open-tubular designs, not only for reversed phase chromatography discussed previously, but also for ion-exchange chromatography,[8] chiral separations by membrane chromatography,[9] and others.[4,10] However, for liquid chromatography, open-tube systems have several disadvantages. In general, they are intrinsically less efficient than packed beds due to the smaller available surface area for phase interactions. In order to reduce mass transfer times, they require small cross-sectional channels that easily clog and severely limit the amount of analyte that can be introduced to the system. In traditional packed-bed chromatography, spherical particles act as a support for the stationary phase, create large surface areas to increase interaction between the stationary and mobile phases, and form a network of channels that act to distribute the mobile phase and analyte evenly across the width of the column to reduce peak dispersion.

While packed bed chromatography would be more favorable in a number of ways, one of the difficulties of packing a microchip with loose particles is trapping them into a

dense bed. Following up on their previous work, Manz et al. fabricated a similar device with an incorporated split injector, a packed bed of C18 particles held in place with a frit, and an optical detector.[4] The device was used to separate fluorescent dyes in 3 minutes with 200 theoretical plates. Weirs, or channel segments etched to be no deeper than the particle diameter, are also a common method for trapping stationary phase particles. An example of a packed bed chromatographic chip was discussed by Oleschuk et al.[3] In this device, a chamber bound on either side with two weirs was electrokinetically filled with 1.5 to 4 μm C18 coated silica particles. The 1.0 μm deep weirs prevented the particles from escaping the chamber while fluid flow was uninhibited. The device was initially used for solid phase extraction, but was also used for electrochromatography yielding a plate height of 2 μm.

As an interesting alternative to open channels or packed beds, He et al.[11] produced an etched nanocolumn for electrochromatography. The devices described could conceptually work with traditional pressure driven flow, but the device's small size required pressures below the capabilities of commercially available HPLC pumps available at the time. The chip design was etched into a quartz wafer and consisted of an array of micron-sized support structures that mimic particles in a traditional packed column. Anisotropic etching via parallel plasma reactive ion etching was used to provide high aspect ratios. A number of feature geometries and sizes were tested, including diamonds, circles, rectangles, and hexagons. Also studied were fluid inlet geometries and structures at the "walls" of the separation channel. These "wall" structures were especially of interest as heterogeneous packing in columns can adversely affect the separation efficiency. The channels were coated with a reversed phase stationary phase. The resulting separations used laser induced fluorescence (LIF) detection. Using a 4.5 cm long channel with 5 μm x 5 μm x 10 μm posts

separated by 1.5 μm wide channels, plate heights of as low as 0.58 μm were attained. The same group used a similar device to separate a mixture of tryptic peptides from ovalbumin.[12] The separation was run under isocratic and gradient elution conditions. Interestingly, better separation resolutions were obtained under isocratic conditions than in gradient mode. Further modifications to this type of structure included using PDMS as the substrate[13] and surface modification of the PDMS for peptide separations.[14]

An increasingly popular stationary phase for microfluidic devices are porous polymer monoliths (PPM). These structures are relatively simple to prepare *in situ* and can be made with a variety of surface chemistries. To form the PPM, a solution of the desired monomer is flushed through the channel and exposed to UV light to induce polymerization. A photomask can be used to confine the polymerized monolith to certain areas of the microchip. Channel or capillary surfaces can also be modified to provide bonding sites for the monolith, locking the structures in place without need for weirs or frits. Polymer monoliths have been previously used in capillary-based systems,[15,16] and have become increasingly common in microfluidic devices over the last decade.[17-20] Ngola et al.[18] discussed the development of a number of acrylate-based polymers used as PPM. The monomers can be varied extensively, altering the hydrophobicity and pore size depending on the desired separation. Using monolith-filled microchips run under electrochromatographic conditions, efficiencies in excess of 150,000 plates/m were attained. In the same research group, Throckmorton et al.[19] made use of monoliths to perform reversed phase separations of fluorescently labeled peptides and amino acids detected by LIF. The separation was reported to be highly reproducible, with relative standard deviations (RSD) of less than 3% for the retention times. The separations were also very well resolved, with efficiencies up to

600,000 plates/m. Finally, it was demonstrated that the monolith could be removed by thermal incineration so that the microchip could be reused with a fresh stationary phase.

As previously stated, the large inlet pressures required in liquid chromatography present significant difficulties for microfabricated devices. To withstand the high pressures associated with standard HPLC, Liu et al.[20] created a novel needle-based interface that survived internal pressures above 2900 psi. For this connection, a polished needle was inserted into a polymer chip and annealed over 4 hours to hold it in place. A polymethacrylate monolith was used as the stationary phase to separate several model peptides. The device also incorporated a trap column to further clean and enrich the sample. The trap column also helped to reduce the injected sample volume, improving the separation performance and the fluorescence detection limits.

Desmet et al. devised a means of circumventing inlet pressure limitations through "shear driven" chromatography (SDC).[21-26] The device consisted of a channel split axially into two halves, one of which was much longer than the other. The microchip was not bonded like standard microfluidic devices, but held in place in a construction with a movable wall. The longer channel plate was dragged past the shorter channel, creating shear force that moved fluid through the channel. The channels could be fabricated with depths as low as 100 nm to perform separations at very high speeds (up to 2 cm/s). For comparison, a corresponding pressure driven system was calculated to require pressures of over 30 kbar to achieve the same flow rate in such a small channel. The initial separations done with this method were performed in relatively deep channels, 8 to 20 μm in depth, packed with 4 μm HPLC beads.[23] The device was extensively characterized under different flow rates, and the resulting Van Deemter curves yielded an efficiency of 90,000 plates/m at the optimal

velocity.[24] In a more recent publication, the same group discussed an open channel reversed phase separation in a 120 nm deep channel with fluorescence detection.[26] A separation of coumarin dyes was performed in 0.85 seconds with a separation speed of 10 mm/s, and an efficiency of over 230,000 plates/m was achieved. However, the extremely small separation channel limited the sample injection volume to the picoliter range, making detection difficult.

With the continuing development of many types of liquid chromatography microfluidic chips, there has been increased interest in devices that integrate the necessary components for stand-alone operation.[27-30] By incorporating components such as valves, trap columns, splitters, analytical columns, and detectors or electrospray tips into the same device, the dead volume due to the various junctions is reduced and the reproducibility increased. In bench-top LC systems, the multitude of parts makes detection and troubleshooting of leaks or blockages difficult. An integrated microfluidic device not only eliminates the possibility of leaks but is also easily replaced if channels become blocked.

One such integrated device was introduced by Yin et al.[27] The device was fabricated from laminated polyimide films with laser-ablated channels, frits, and access ports. The device was fabricated with a laser ablated electrospray tip to interface with a mass spectrometer for sample detection. Prior to bonding the device, the patterned electrical contacts were sputtered on the internal side of one of the substrates in order to directly contact the solution once the device was completed. This method is more in line with conventional electrospray tips, unlike the electroosmotic pumping method developed in the Ramsey group[31,32] that was discussed in Chapter 4. Once the device was assembled, the sample enrichment channel was packed with conventional 5 μm C18 particles, and the analytical channel was packed with 3.5 μm C18 particles. The microchip design included

ports for a two-position rotary switching valve, and the mechanical components were mounted on the chip's holding stage. Separations of tryptic protein digests were performed under gradient conditions at flow rates between 100 and 300 nL/min. Separations with subfemtomole sensitivity were achieved while the chip proved to be robust and reliable under the conditions studied.

In this chapter, the use of conductivity-based photothermal absorbance detection in conjunction with liquid chromatography is discussed. All tests were performed with a traditional HPLC pump and valve system for expedient testing of photothermal detection with liquid chromatography. The initial runs were performed with a commercially available packed column connected to the microchip photothermal detector via surface-mounted ports. As an end-column detector, there is little remaining pressure in the line, and high-pressure connections are unnecessary. Several separations of small molecules were performed under isocratic and gradient elution and compared to a conventional UV detector. A photothermal detection microchip with an incorporated packed bed of reversed phase particles was also fabricated for testing. A separation of several peptides was done with baseline resolution, and detection limits in the tens of femtomoles were achieved.

5.2 Experimental

5.2.1 Materials

Guanosine, uracil, tryptophan, thymidine, rhodamine B, and bovine serum albumin (BSA) were obtained from Sigma (St. Louis, MO). HPLC grade methanol, acetonitrile, sulfuric acid (H_2SO_4), sodium hydroxide (NaOH), glacial acetic acid solutions, and borax for borate buffer were purchased from Fisher Scientific (Fair Lawn, NJ). The 2',7'–

dichlorofluorescein (laser grade) was obtained from Acros Organics (Geel, Belgium). Buffer solutions were made with deionized water (Barnstead Nanopure Diamond Filtration System, Boston, MA). Electrophoresis running solutions were either 1% acetic acid in water (v/v) or 20 mM borate adjusted to pH 8.0.

Quartz substrates used for device fabrication were 4 in x 4 in x 2.2 mm (l x w x h) grade CG wafers coated with a 1200 Å low reflectivity chrome layer and a 5300 Å layer of AZ 1518 photoresist. Also used were 4 in x 4 in x 0.9 mm (length x width x thickness) white crown (B-270) glass grade PG wafers coated with 1200 Å film of low reflectivity chrome and 5300 Å of AZ 1518 photoresist (Telic, Valencia, CA). Quartz cover slips for thin substrates were purchased from SPI Supplies (West Chester, PA). C18 coated 5 μm Symmetry particles with 15 nm pore size were obtained from Waters Corp. (Milford, MA).

5.2.2 Microchip Fabrication

The top substrate was etched with a single 2.5 cm long channel and was made from photoresist/chrome coated quartz glass (Telic, Valencia, CA) or 1 in x 1 in x 200 μm quartz cover glass (SPI Supplies, West Chester, PA). The quartz cover glass was sputtered with a 400 μm chrome layer using a Model IBSe Ion Beam Deposition System (South Bay Technologies, San Clemente, CA) and spin coated with S1813 photoresist using a Model 6700 Spincoater (Specialty Coating Systems, Indianapolis, IN). The channel substrates were cut into 1 in x 0.5 in pieces using a Basic Dicer II (Dicing Technology, Longwood, FL). A straight channel photomask was designed using TurboCAD v. 9.2 Student Edition (Novato, CA). The completed designs were sent to The Photoplot Store (Colorado Springs, CO) for printing on a mylar film base with an Accumax ARD7 printed emulsion layer (Kodak,

Rochester, NY). The mask was placed emulsion side down directly onto the substrate surface, and a 4 in x 4 in quartz blank was placed over it to ensure good contact between the two. The photoresist was exposed through UV flood exposure using a J200 UV Exposure System (OAI, Milpitas, CA) for 65-75 seconds. Following exposure, the coated substrate was immersed in MF-319 developer (Microchem Corp., Newton, MA) for 45-60 seconds to remove the exposed areas. The substrate was removed from the developer and rinsed with deionized water and dried with pressurized nitrogen gas. The design was then observed under a microscope to ensure complete development. The chrome mask in the channel design was removed using chrome etchant (Transene, Danvers, MA) for 5-10 minutes. The substrate was then rinsed with deionized water, cleaned with 2% sulfuric acid, rinsed again with deionized water, and dried with pressurized nitrogen gas.

The channels were etched isotropically into the quartz substrate using 5:1 buffered oxide etchant (Transene, Danvers, MA). Throughout the etching process, the channel depth was monitored using a P-15 profilometer (KLA-Tencor, San Jose, CA). The etching process was halted before each check by rinsing in deionized water, cleaning with 2% sulfuric acid to remove residue from the channel surface, rinsing again with deionized water, and drying with pressurized nitrogen gas. After reaching a 30 μm depth (125 μm wide), the substrate was coated with a thick layer of S1813 photoresist to protect the channel. Access holes were drilled at the channel ends using a MB 1000-1 powder blaster (Comco, Inc., Burbank, CA) set to make holes 1 mm in diameter for the 2.2 mm thick substrate or 0.4 mm for the coverslip substrate. Access hole size was monitored carefully for the LC studies in order to minimize dead volume in the chip-capillary junctions. The photoresist was then removed with acetone, and the remaining chrome mask removed with chrome etchant.

The substrate for the electrodes was stripped of photoresist and the chrome layer before applying a fresh layer of S1813 photoresist via spincoating. The designs for the electrodes were patterned and etched to 100 nm according to the procedure above. The metal thin films composing the electrodes were applied using a Model IBSe Ion Beam Deposition System (South Bay Technologies, San Clemente, CA). A 30 nm thick adhesive layer of chrome was applied followed by a 70 nm layer of platinum. The etching step prior to sputtering acted to embed the metal, resulting in electrodes that were flush with the substrate surface. All electrodes were 50 μm wide with a 100 μm gap.

To prepare for bonding, the completed microchip components were immersed in Nanostrip 2x (Cyantek Corperation, Fremont, CA) for up to 15 min in order to remove any remaining organic residue on the surfaces. After rinsing with deionized water, the substrates were sonicated in a 2% Contrad 70 solution for 10 minutes, removed, and rinsed again. A hydrolysis bath composed of two parts water, two parts 30% ammonium hydroxide, and one part 30% hydrogen peroxide was prepared and heated to 65-70°C. The substrates were immersed in the hydrolysis bath for 10-15 minutes to activate the quartz surfaces. They were then rinsed with deionized water and sonicated for an additional 10 minutes. After removing from sonication, the electrode slide was held face up, and deionized water was pooled over its surface. The channel substrate was laid over the electrodes, and the excess water was wiped off the surfaces. The channel and electrodes were carefully aligned under a microscope, and the substrates were clamped together. The chip was placed in a convection oven set to 95°C to evaporate the remaining water. After 5 minutes, the chip was removed from the oven and visually examined for good contact around the microfabricated features. Poorly bonded areas were evident through the appearance of interference patterns. If good

bonding was observed, the chip was placed back into the oven for an additional 10-20 minutes. The device was then placed into a furnace (Lindberg/Blue, Watertown, WI) for bonding. The furnace program was set to ramp to 90°C over 10 minutes, held at 90°C for 2 hours to ensure removal of any remaining water, increased to 200°C over 2 hours and held for 1 hour, and ramped to 550°C over 2 hours. The furnace was held at 550°C for 10 hours, after which it was cooled to 95°C over 2 hours. Once bonding was completed, a surface mounted N-131-01 ¼-28 port (Upchurch Scientific, Oak Arbor, WA) was applied over the entrance of the 2.2 mm unpacked chip using a UV curable optical adhesive (Norland, Cranbury, NJ). The fitting held a 20/360 (i.d/o.d) fused silica capillary (Polymicro Technologies, Phoenix, AZ) in 380 i.d., 1/16 o.d. polyetheretherketone (PEEK) tubing segment. An in-house machined steel clamp and a N-129H NanoPort fitting (Upchurch Scientific, Oak Arbor, WA) provided pressure resistant seals between the thin-substrate packed microchip and a 20/360 fused silica capillary. The channel exits were left open. To prevent fluid leakage through any gaps created by the metal film, a small amount of epoxy was applied at the point the electrodes emerged from under the channel substrate.

5.2.3 HPLC Setup

The setup for liquid chromatography with photothermal detection is shown in Figure 5-1. A Waters Micromass CapLC pump (Waters Corp., Milford, MA) was used for all liquid chromatography experiments. The pump was controlled through a USB-6229 DAQ card (National Instruments, Austin, TX) using MassLINX software (Waters Corp., Milford, MA). Tubes from the aqueous and organic mobile phases were joined at a 1/16 in T-junction (Valco Instruments Co. Inc., Houston, TX). A 20/360 fused silica capillary ran from the

junction to a VICI 8-port injection valve (Valco Instruments Co. Inc., Houston, TX). The injection valve was arranged with a 1 µL sample injection loop and connections leading to the pump, to the chromatography column, and two to waste. A commercially available 320 µm inner diameter (i.d.), 15 cm long Waters chromatography column with 5 µm porous Symmetry C18 particles (Waters Corp., Milford, MA) was used for HPLC separations with end-column photothermal detection. The column was connected to the photothermal chip via a 20 cm segment of 20 µm i.d. capillary held in place with a sleeve of 1/16 in polyetheretherketon (PEEK) tubing with a 380 µm i.d. The junctions were surface mounted N-131-01 ¼-28 port with a N-131-02 10-32 x ¼-28 NanoPort insert and P-844X VacuTight Headless fitting with ferrule (Upchurch Scientific, Oak Arbor, WA). All fused silica capillary was purchased from Polymicro Technologies (Phoenix, AZ).

5.2.4 Particle Packing on a Microfluidic Chip

To hold the packed bed in place, a shallow weir was added to the channel during the etching process. A 0.5-1.1 mm wide spot of photoresist was placed across the channel after it had reached a depth of 6-10 µm and dried in a convection oven at 95°C. Channel etching continued as before, leaving the shallow weir. During the packing process, particles were caught by the weir, forcing the bed to form before it (Figure 5-2).

The 5 µm diameter C18 Symmetry (15 nm pore size) particles (Waters Corp., Milford, MA) were mixed as a slurry at 10 mg/mL in acetone. The slurry was placed in an in-house machined pressure bomb and helium flow gas was applied at approximately 500 psi. The slurry was forced through a 100 µm i.d. fused silica capillary connected to the microchip via an in-house machined steel clamp and fitting. The weir prior to the chip's detection

electrodes acted to catch the moving particles and initiate packing of the particle bed in the channel. Packing was monitored under a microscope. Once the packed bed had filled the chip and part of the connecting capillary, the helium pressure was released gradually through a release valve. The packed bed was prepared for use by flowing high organic content mobile phase, in this case 1% acetic acid in 25%/75% water/acetonitrile (v/v), through the microchip at 15 μL/min for 15 minutes. A gradient from the high organic mobile phase to the aqueous mobile phase (1% acetic in 95%/5% water/acetonitrile) at 15 μL/min was applied over the course of 1 hour. The aqueous mobile phase was flushed at a reduced rate of 1 μL/min overnight.

The resulting 2 cm packed bed had an optimal flow rate of 35 nL/min, which was well below the HPLC system's limits. To ensure a stable pumping rate, the flow rate was set to 0.5 μL/min with a 10:1 split (1/32 in T-junction, Valco Instruments Co. Inc., Houston, TX) prior to the microchip.

5.2.5 Electronic Setup

The output of two DS345 digital function generators (Stanford Research Systems, Sunnyvale, CA) were applied to the excitation and reference electrodes in order to provide the AC excitation signal. The two function generators were set in a master-slave configuration, using the 10 MHz output of one as the time base of the other. The phase and voltage were adjusted in order to balance the function generators precisely 180° out of phase with each other, using destructive interference to provide zero background conductivity at the detection electrode. The excitation signal passed through a 3 kV, 100 pF radial disc capacitor (Panasonic-ECG, Secaucus, NJ) prior to and after the detection cell. This isolates

the excitation electronics from the DC electrophoresis running voltage. Connections to the microchip electrode pads were made with an aluminum pad connected to a 316 stainless steel compression spring (Small Parts Inc., Miami Lakes, FL), which was soldered to the end of a banana connection in a in-house machined polycarbonate (McMaster, Atlanta, GA) microchip holder mounted on an x-y-z translational stage. Signal from the detection electrode was amplified via an OPA602 operational amplifier (Texas Instruments, Dallas, TX) in a current-to-voltage circuit with a 1 MΩ feedback resistor (Multicomp, Chicago, IL), thus providing a total gain of 10^6 V/A. Surface mounted 1000 pF capacitors (Newark Electronics, Chicago, IL) added to the circuit removed any high frequency noise from the power supply or feedback loop of the operational amplifier. A grounded aluminum box provided shielding for the electronic circuit. A Model 1301 Power Supply (Global Specialties, New Haven, CT) at ±15 V provided power for the operational amplifier.

Output from the chip was further amplified and filtered with two SR810 digital lock-in amplifiers (Stanford Research Systems, Sunnyvale, CA) arranged in series. The first lock-in amplifier was referenced to the master DS345 function generator and provides the standard conductivity signal for reference purposes. Output from this lock-in was input to the second lock-in amplifier, which is referenced to the "*f*" output of a MC1000A Optical Chopper System (ThorLabs, Newton, New Jersey), and thus the modulation frequency. The first lock-in was set at a 1 ms time constant and a 24 dB/octave slope (bandwidth = 78 Hz) with AC coupling, and the second lock-in amplifier was set with a 100 ms time constant and a 24 dB/octave slope (bandwidth = 0.78 Hz) with DC coupling. Line and 2x line filters were used on both lock-in amplifiers. The sensitivity was set at 1 mV for the first lock-in during all experiments and varied for the second to maximize photothermal sensitivity.

Data collection and control of both the function generators and the lock-in amplifiers were maintained with a USB-6229 DAQ card (National Instruments, Austin, TX) and custom software written in LabVIEW (National Instruments, Austin, TX) on a personal computer. Data analysis was performed using Igor Pro (Wavemetrics, Lake Oswego, OR).

5.2.6 Optical Setup

Photothermal excitation at 266 nm was provided by a frequency doubled Verdi 532 nm laser with an attached MBD266 doubler (Coherent, Santa Clara, CA). A beam splitter prior to the doubler was used to moderate the total input to the MBD266. The maximum UV power used in these experiments was approximately 500 mW. The beam was modulated using a MC1000A Optical Chopper System with a 2-slot blade (ThorLabs, Newton, New Jersey), which provides frequencies between 1 Hz and 99 Hz. The beam was cleaned with a spatial filter consisting of a F5 singlet lens, a 100 μm pinhole (Melles Griot, Albuquerque, NM), and a F2 singlet lens. A mirror with UV-enhanced reflective metal coating was used to direct the beam up through a fused silica singlet lens to the microfluidic chip. The elliptical beam was focused to a spot size of about 20 μm x 70 μm at the microchip channel, and was oriented such that the longest dimension was parallel to the electrodes (Figure 4-2). All lenses and mirrors were fabricated of fused silica and suitable for UV light manipulation (ThorLabs, Newton, NJ). The mirrors were rated to reflect approximately 80% of the incident light at 266 nm wavelength. Positioning of the beam in relation to the microchip electrodes was observed using a PL-A741 machine vision camera (PixeLINK, Ottawa, ON). To provide additional focusing and reduce the intensity of the laser light, a F/2 fused silica

singlet lens (ThorLabs, Newton, NJ) and two neutral density filters (FNQ057 and FNQ065, Melles Griot, Albuquerque, NM) were placed before the camera.

5.3 Results and Discussion

5.3.1 Initial Laser Modulation Tests

During the laser beam modulation frequency studies described in Chapter 3, the measured conductivity response produced the expected square-like modulation pattern. However, using the electrophoretic photothermal microchip with UV wavelength laser light, the conductivity response had an irregular shape (Chapter 4). Initial theories about the irregular shape included that the analyte was being photobleached, but the irregular shape was present in both the "on" and "off" phases of the modulation. Photobleaching might have explained the abnormal shape when the laser was "on," but not when the beam was blocked, or "off." Another contributing factor to the irregular shape may have been related to the magnitude of the temperature change affecting the electrokinetic flow. Electroosmosis is sensitive to the conditions within the channel, so as the analyte traversed the detection region, the localized temperature changes at the low chopping frequencies may have disrupted the electroosmotic flow and the recorded signal, yielding abnormalities in the anticipated square-like traces.

In an attempt to better understand the source of the abnormal conductivity response, an unpacked LC photothermal microchip was connected directly to the HPLC system. The photothermal responses of 100 μM each of guanosine, fluorescein, and uracil were examined between 1 Hz and 30 Hz. Segments of the conductivity trace of guanosine are shown in Figure 5-3. These traces display the square wave-like pattern expected and demonstrated

using the 488 nm laser and pressure driven flow seen in Chapter 3. The photothermal signal of the three analytes also followed the trends observed with the visible photothermal detector in Chapter 3 (Figure 5-4). The signal showed a general decrease in strength with increasing modulation frequency, and no decrease at the lowest frequencies like that observed as a function of modulation frequency with the electrophoretic chip (Chapter 4). Figure 5-4 also shows a less than 10 % variation in the average noise for the range studied. It should be noted that these experiments were run with a laser chopper that was more stable than the one used to collect data for the visible photothermal studies. The resulting signal to noise values for the three analytes are shown in Figure 5-5. From this, the optimal modulation frequency is approximately 2.5 Hz. This behavior indicates that the irregularities observed in the electrophoretic chip were possibly related to electric field effects.

5.3.2 End-column Microchip Detector

Initial testing of photothermal detection in conjunction with liquid chromatography was done with an external, commercially available column packed with 5 μm C18 particles. All chromatographic runs were done with 100 mW laser power, 20 Hz modulation, and a sinusoidal excitation signal of 100 kHz and 5 V_{pp}. The system was run at 3 μL/min, the optimal flow rate of the column. Analytes separated under these conditions were 100 μM uracil, guanosine, thymidine, and tryptophan. With an injection loop of 1 μL, a total of 100 pmol of each analyte was injected. Uracil acted as the dead time marker. A mixture of water and methanol with 1% acetic acid was used as the mobile phase.

Isocratic separations of the four analytes were performed with a variety of mobile phase compositions. Figure 5-6 shows a chromatogram produced using 90% water and 10%

methanol (v/v) mobile phase. The separation achieved baseline resolution of thymidine and tryptophan, and near baseline resolution of uracil and guanosine. Details of the peak height, area, migration time, and theoretical plate count for each peak are reported in Table 5-1. The background noise was approximately 6.4 μV_{rms}, and signal to noise ratios were 624, 2100, 1360, and 446 for uracil, guanosine, thymidine, and tryptophan, respectively. With these signal to noise values, the limits of detection (S/N=3) were extrapolated to be 480 nM (0.48 pmol) for uracil, 140 nM (0.14 pmol) for guanosine, 220 nM (0.22 pmol) for thymidine, and 670 nM (0.67 pmol) for tryptophan.

Using the same setup and analytes, the separation was run with a gradient elution. Figure 5-7 shows a chromatogram produced using a gradient of 90% water and 10% methanol (v/v) ramped to 60% water and 40% methanol over the course of 20 minutes. The peaks of this chromatogram were significantly sharper and cleaner than those observed in the isocratic separation, and baseline resolution was achieved for every analyte. Details of the peak height, area, and migration time are reported in Table 5-2. The background noise for this separation was approximately 6.0 μV_{rms}. The resulting signal to noise ratios were 2100, 4100, 3600, and 660 for uracil, guanosine, thymidine, and tryptophan, respectively. The extrapolated limits of detection (S/N=3) were 0.14 pmol for uracil, 0.073 pmol for guanosine, 0.083 for thymidine, and 0.45 pmol for tryptophan.

5.3.3 Integrated Liquid Chromatography/Photothermal Detection Device

A second photothermal microchip was fabricated and packed with the same 5 µm C18 particles as the commercial column used in the studies above. The chip was made with a 2.5 cm long channel with a weir 0.5 cm from one end. The detector electrodes were

located on the shorter side of the weir, and the remaining 2 cm were packed with the particles. This bed had a calculated optimal velocity of 30 nL/min, but such a slow rate was well below the rated performance of the HPLC pump. As a result, a 10:1 splitter was placed between the injection valve and the microchip, and the pump was run at 500 nL/min to give a flow rate of 50 nL/min at the chip. The packed bed was too short to resolve the simple molecules tested earlier, but larger, more retained peptide molecules were separated under gradient conditions. The three analytes injected onto the chip were 29 pmol thymopentin, 12 pmol neurotensin, and 36 pmol leucine enkephalin (amounts were derived from the 1 μL injection of 20 μg/mL of each analyte after the 10:1 split).

The chromatogram in Figure 5-8 was obtained with a gradient elution of 90% water/10% acetonitrile to 60% water/40% acetonitrile (v/v) over the course of 13 minutes. Earlier runs containing uracil marked the dead time as approximately 4.3 minutes. The resulting chromatogram was baseline resolved for all analytes, but the peak shape was obviously skewed. The low flow rate (50 nL/min compared to 3 μL/min with the conventional column) resulted in a lower background of 3.8 μV_{rms}. The resulting signal to noise ratios were 190, 260, and 1700 for thymopentin, neurotensin, and leucine-enkephalin, respectively, and their extrapolated detection limits (S/N=3) were 0.46, 0.14, and 0.063 pmol. Leucine-enkephalin had a much higher signal response due to the larger molar amount injected into the microchip and presence of multiple 266 nm-absorbing aromatic amino acids in its structure that were not present in the other analytes. Mixing of the solution as it eluted past the weir into the deeper detection region likely contributed to the tailing seen in Figure 5-8. The liquid chromatography aspect of the device has room for improvement, but these experiments demonstrate the potential of an integrated device with photothermal detection.

5.4 Conclusions

Conductivity-based photothermal absorbance detection has been demonstrated to be a promising detection method for liquid chromatography. As an end-column detector for use with conventional high performance liquid chromatography, the photothermal device displayed exceptional limits of detection for small, native molecules. A packed bed of reversed phase particles was also incorporated into a photothermal device for integrated separation and detection. The short 2 cm packed bed was used to separate several native peptides and provided baseline resolution for each analyte. Although the separation power was limited due to the short length of the packed bed, the device was useful for proof-of-concept testing.

The conductivity-based photothermal absorbance detection device described here has been successfully utilized with both liquid chromatography and capillary electrophoresis. The microfabricated photothermal detector has exhibited high sensitivity for a multitude of native analytes that meets or exceeds the sensitivity of conventional 1-cm path length UV absorbance detectors. At the present time, the photothermal detection device has been well-characterized. Demonstrations with both electrophoretic and liquid chromatographic separations indicate the usefulness of photothermal detection in conjunction with two basic analysis techniques, leaving open the opportunity for its application to any number of related techniques that require sensitive detection of native analytes.

5.5 Tables and Figures

Table 5-1: Calculated peak information of the isocratic elution of four analytes using an end-column photothermal detector. Injections were 1 µL of 100 µM of each analyte. The mobile phase was 90% water/10 % methanol (v/v) flowed at 3 µL/min. The laser conditions were 100 mW and 20 Hz modulation and the excitation signal was 100 kHz and 5 V_{pp}. The chromatogram for this data is shown in Figure 5-6. The background noise was 6.34 µV_{rms}. Limits of detection were calculated at S/N=3

Analyte	Uracil	Guanosine	Thymidine	Tryptophan
Peak Height (mV)	3.96	13.3	8.64	2.83
Peak Area (mV·min)	1.45	5.3	4.36	1.64
Elution Time (min)	5.61	6.35	10.7	17.8
Theoretical Plates	1340	969	1460	3480
Signal to Noise	620	2100	1400	450
Limit of Detection (nM)	480	140	220	670
Limit of Detection (pmol)	0.48	0.14	0.22	0.67

Table 5-2: Calculated peak information of the gradient elution of four analytes using an end-column photothermal detector. Injections were 1 µL of 100 µM of each analyte. The gradient was 90% water/10% methanol to 60% water/40% methanol (v/v) over 20 minutes with a flow rate of 3 µL/min. The laser conditions were 100 mW and 20 Hz modulation and the excitation signal was 100 kHz and 5 V_{pp}. The chromatogram for this data is shown in Figure 5-7. The background noise was 5.95 μV_{rms}. Limits of detection were calculated at S/N=3

Analyte	Uracil	Guanosine	Thymidine	Tryptophan
Peak Height (mV)	12.3	24.4	21.4	3.95
Peak Area (mV·min)	2.63	6.40	5.91	1.26
Elution Time (min)	5.13	9.70	12.7	17.0
Signal to Noise (S/N)	2100	4100	3600	660
Limit of Detection (nM)	140	73	83	450
Limit of Detection (pmol)	0.14	0.073	0.083	0.45

Table 5-3: Calculated peak information of the gradient elution of three peptides using an integrated liquid chromatography chip with photothermal detection. The gradient was 90% water/10% acetonitrile to 60% water/40% methanol (v/v) over 20 minutes with a flow rate of 3 μL/min. The laser conditions were 100 mW and 20 Hz modulation and the excitation signal was 100 kHz and 5 V_{pp}. The chromatogram for this data is shown in Figure 5-8. The background noise was 3.8 μV_{rms}. Limits of detection were calculated at S/N=3

Analyte	Thymopentin	Neurotensin	Leucine Enkephalin
Amount Injected (pmol)	29	12	36
Peak Height (mV)	0.710	0.978	6.32
Peak Area (mV·min)	0.045	0.097	1.05
Elution Time (min)	14.8	15.1	15.6
Signal to Noise (S/N)	190	260	1700
Limit of Detection (nM)	460	140	63
Limit of Detection (pmol)	0.46	0.14	0.063

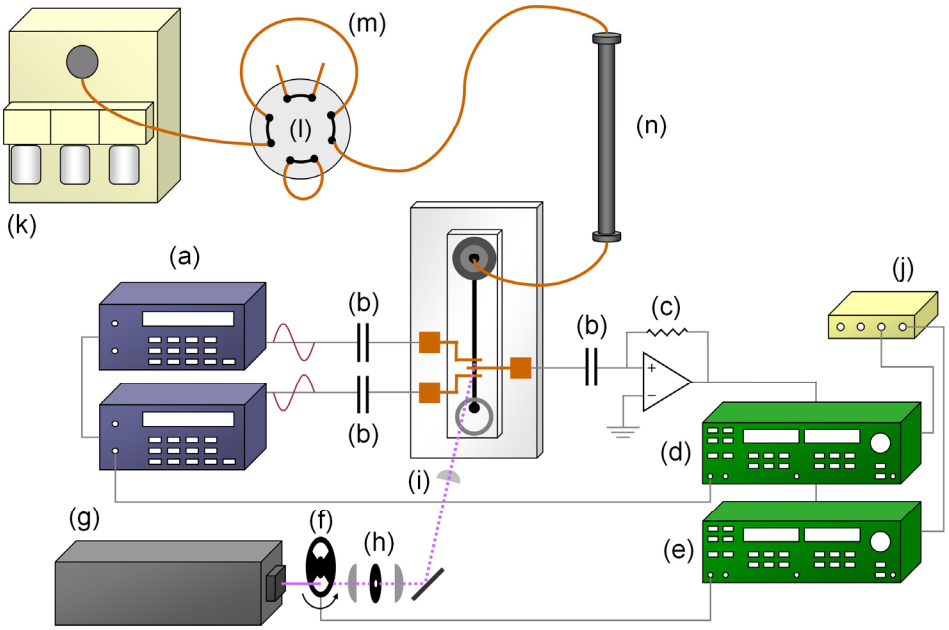

Figure 5-1: Schematic of the microchip photothermal setup, with the microchip containing the separation channels and electrodes shown at the center. Individual components are (a) two phase-locked function generators, (b) high voltage capacitors for isolation of AC components from the DC electrophoretic running voltage, (c) feedback resistor, (d) conductivity lock-in amplifier, and (e) photothermal lock-in amplifier, (f) optical chopper, (g) laser, (h) spatial filter, (i) singlet lens for beam focusing, and (j) USB DAQ. A conventional (k) HPLC pump, (l) low dead volume 8-port injection valve with (m) 1 µL sample injection loop, and (n) analytical column were used. The reference for the conductivity lock-in amplifier is supplied by one function generator, and the reference for the photothermal lock-in amplifier is supplied by the optical chopper.

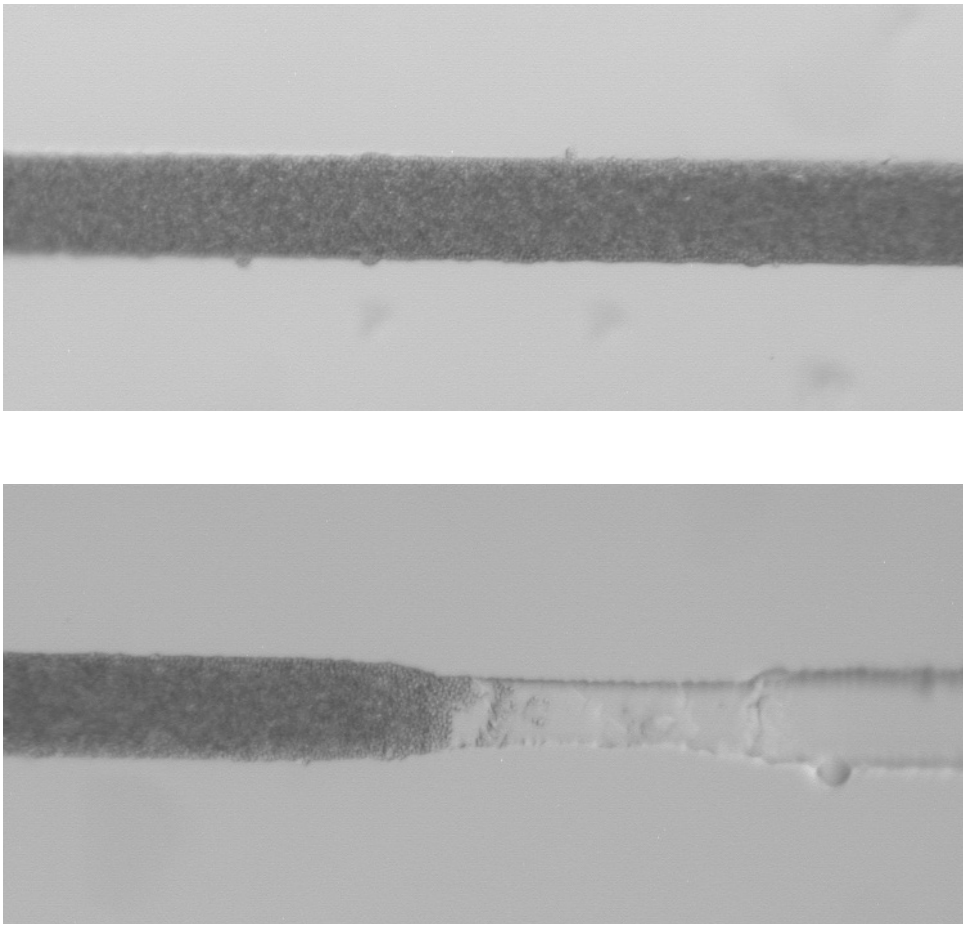

Figure 5-2: Images of the particle packed bed on the integrated liquid chromatography-photothermal detection microdevice. (top) A segment of the packed bed to demonstrate packing efficiency, and (bottom) the weir used to trap the particle bed. Channels were 30 µm deep and 125 µm wide, the weir was 8 µm deep and 70 µm wide, and the channel was packed with 5 µm particles.

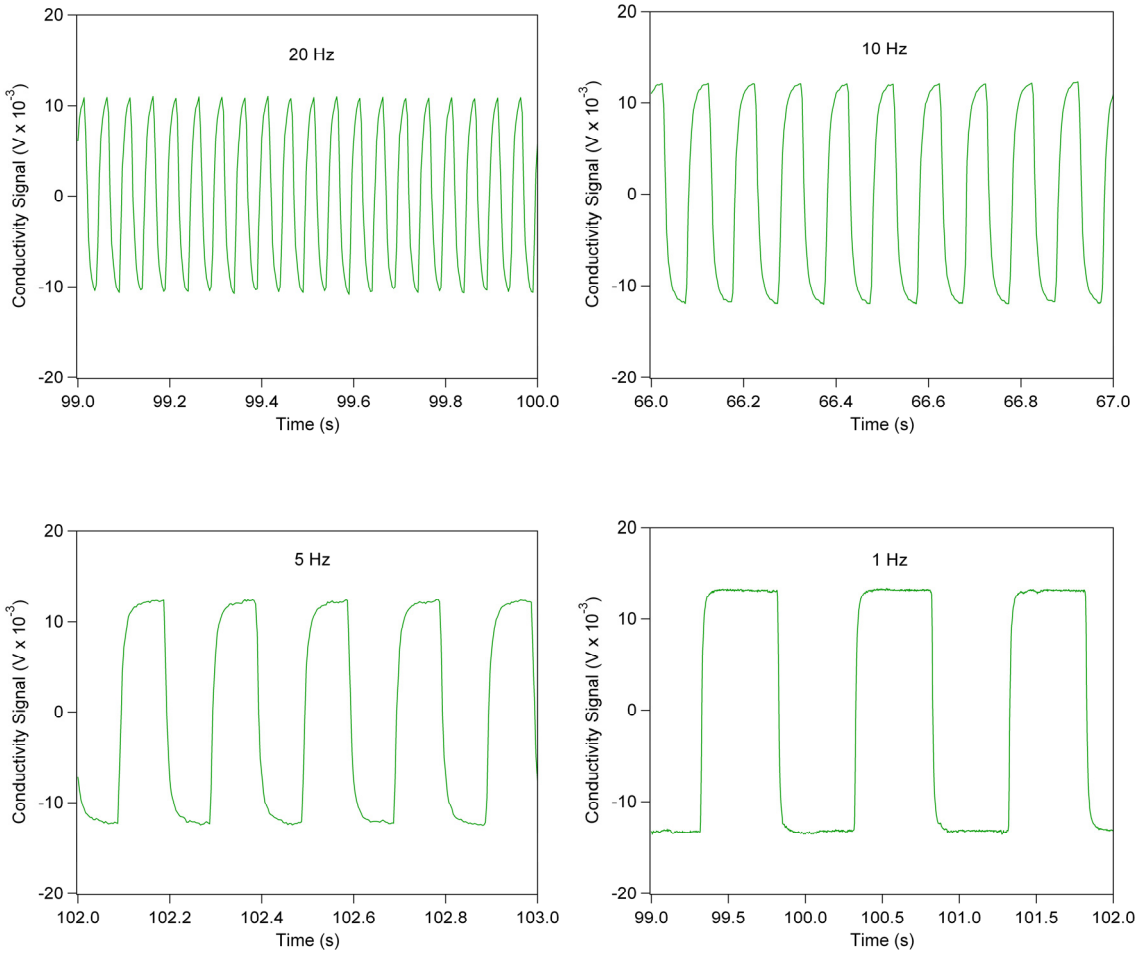

Figure 5-3: The conductivity trace for 100 µM guanosine at 20, 10, 5, and 1 Hz.

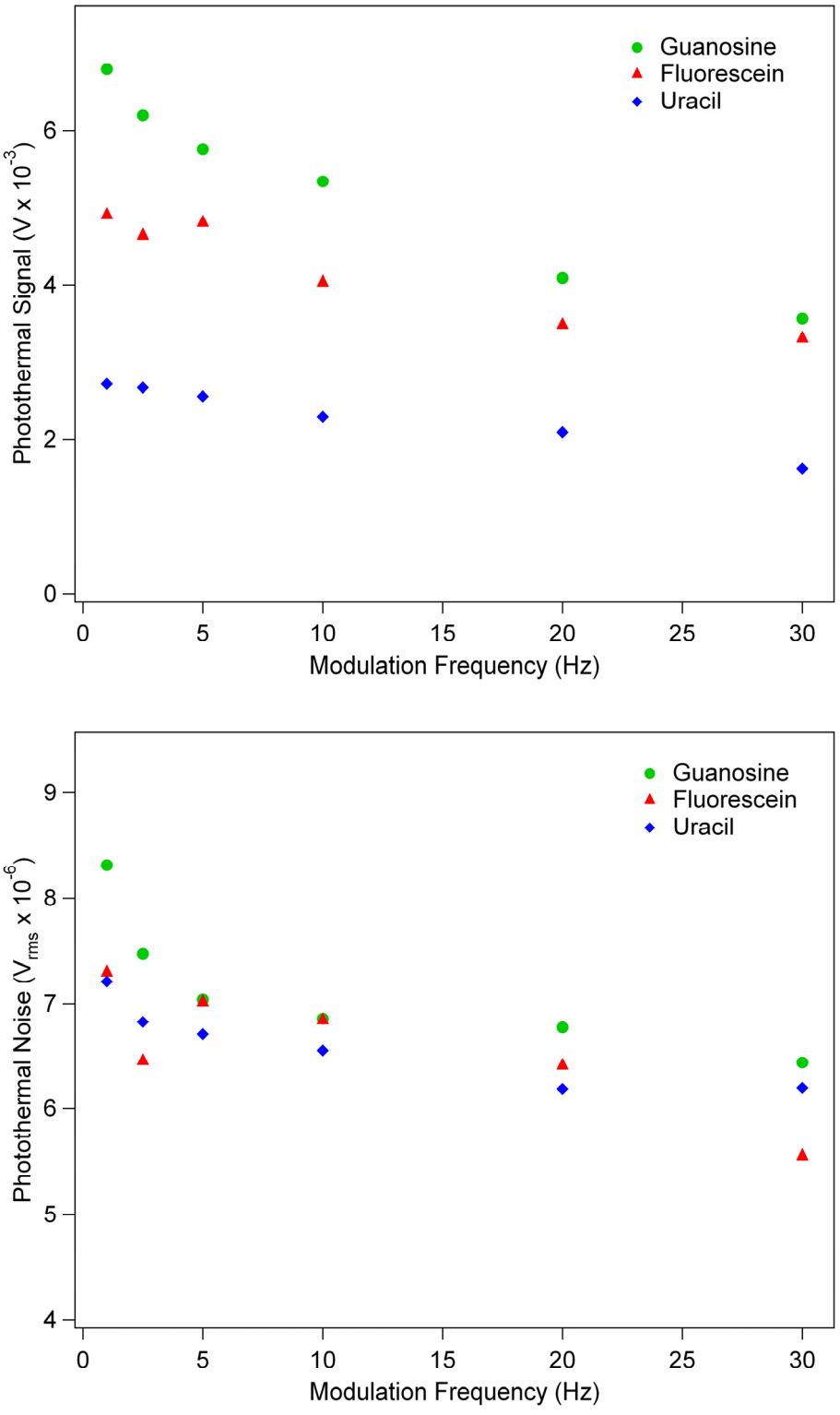

Figure 5-4: The photothermal signal of 100 µM guanosine, fluorescein, and uracil (top) and the background noise (bottom) plotted against the laser modulation frequency. The laser power was 100 mW, the excitation signal was 100 kHz and 5 V_{pp}, and the flow rate was 1 µL/min.

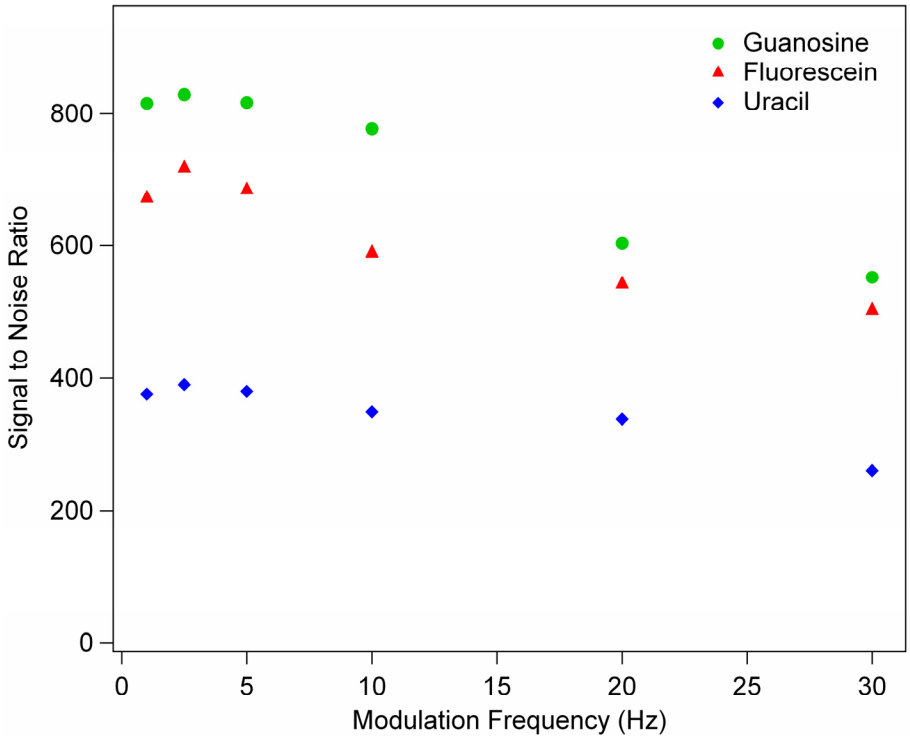

Figure 5-5: The photothermal signal to noise ratios of 100 µM guanosine, fluorescein, and uracil plotted against the laser modulation frequency. The laser power was 100 mW, the excitation signal was 100 kHz and 5 V_{pp}, and the flow rate was 1 µL/min.

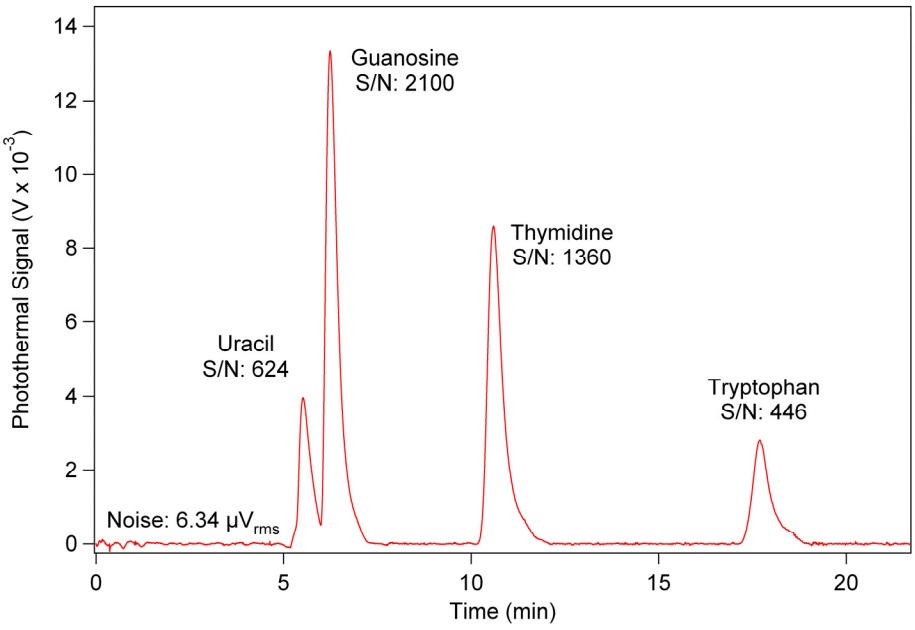

Figure 5-6: Isocratic elution of 1 µL of 100 µM uracil guanosine, thymidine, and tryptophan. The mobile phase was 90% water/10 % methanol (v/v) flowed 3 µL/min. The laser conditions were 100 mW and 20 Hz modulation, excitation signal was 100 kHz and 5 V_{pp}.

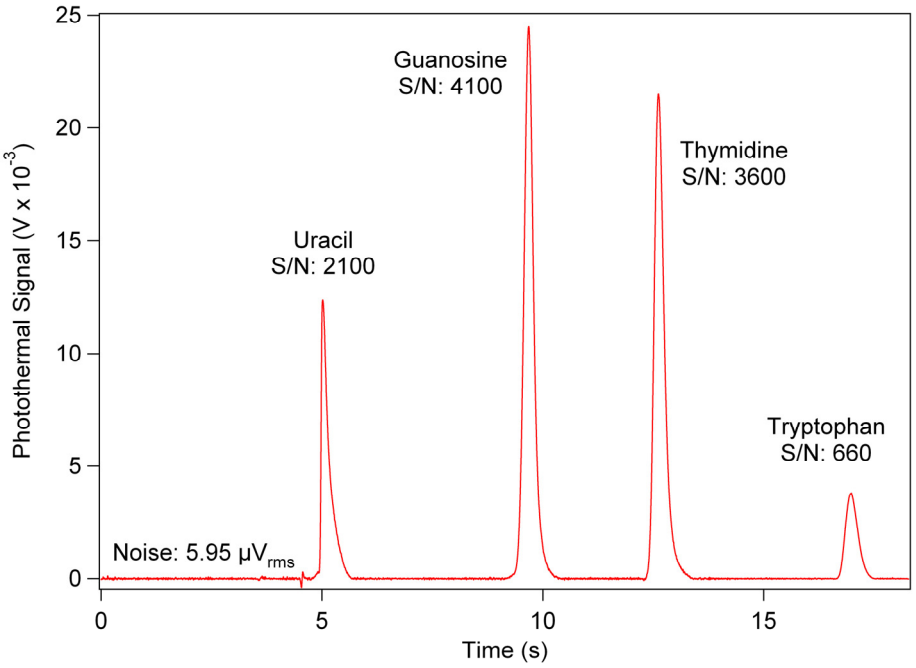

Figure 5-7: Gradient elution of 1 µL of 100 µM uracil guanosine, thymidine, and tryptophan. The gradient was 90% water/10% methanol to 60% water/40% methanol (v/v) over 20 minutes with a flow rate of 3 µL/min. The laser conditions were 100 mW and 20 Hz modulation and the excitation signal was 100 kHz and 5 V_{pp}.

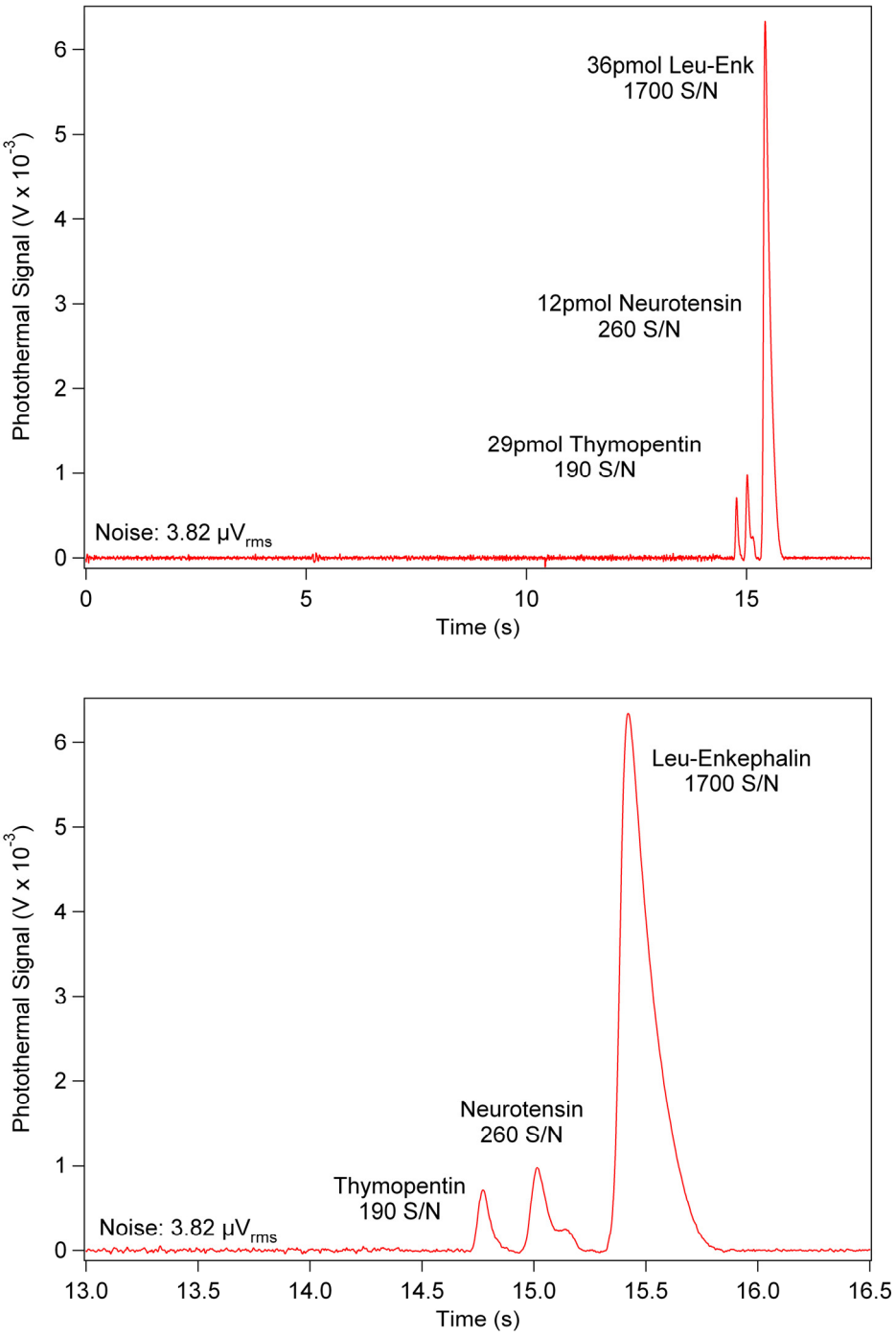

Figure 5-8: Gradient elution of 29 pmol thymopentin, 12 pmol neurotensin, and 36 pmol leucine enkephalin. The gradient was 90% water/10% acetonitrile to 60% water/40% methanol (v/v) over 20 minutes with a flow rate of 3 μL/min. The laser conditions were 100 mW and 20 Hz modulation and the excitation signal was 100 kHz and 5 V_{pp}. Top: full elution time, bottom: expansion of the peaks.

5.6 References

(1) Harris, C. M. *Analytical Chemistry* **2003**, 64A-69A.

(2) Jacobson, S. C.; Hergenroder, R.; Koutny, L. B.; Warmack, R. J.; Ramsey, J. M. *Analytical Chemistry* **1994**, *66*, 1107-1113.

(3) Oleschuk, R. D.; Shultz-Lockyear, L. L.; Ning, Y.; Harrison, D. J. *Analytical Chemistry* **2000**, *72*, 585-590.

(4) deMello, A. *Lab on a Chip* **2002**, *2*, 48N–54N.

(5) Manz, A.; Miyahara, Y.; Miura, J.; Watanabe, Y.; Miyagi, H.; Sato, K. *Sensors and Actuators B* **1990**, *1*, 249-255.

(6) Jacobson, S. C.; Hergenriider, R.; Koutny, L. B.; Ramsey, J. M. *Analytical Chemistry* **1994**, *66*, 2369-2373.

(7) Kutter, J. P.; Jacobson, S. C.; Matsubara, N.; Ramsey, J. M. *Analytical Chemistry* **1998**, *70*, 3291-3297.

(8) Murrihy, J. P.; Breadmore, M. C.; Tan, A.; McEnery, M.; Alderman, J.; O'Mathuna, C.; O'Neill, A. P.; O'Brien, P.; Advoldvic, N.; Haddad, P. R.; Glennon, J. D. *Journal of Chromatography A* **2001**, *924*, 233–238.

(9) Wang, P.-C.; Gao, J.; Lee, C. S. *Journal of Chromatography A* **2002**, *942*, 115-122.

(10) Constantin, S.; Freitag, R.; Solignac, D.; Sayah, A.; Gijs, M. A. M. *Sensors and Actuators B* **2001**, *78*, 267-272.

(11) He, B.; Tait, N.; Regnier, F. *Analytical Chemistry* **1998**, *70*, 3790-3797.

(12) He, B.; Ji, J.; Regnier, F. E. *Journal of Chromatography A* **1999**, *853*, 257–262.

(13) Slentz, B. E.; Penner, N. A.; Lugowska, E.; Regnier, F. *Electrophoresis* **2001**, *22*, 3736-3743.

(14) Slentz, B. E.; Penner, N. A.; Regnier, F. E. *Journal of Chromatography A* **2002**, *948*, 225-233.

(15) Svec, F.; Peters, E. C.; Sykora, D.; Yu, C.; Frechet, J. M. J. *Journal of High Resolution Chromatography* **1999**, *23*, 3-18.

(16) LaCourse, W. R. *Analytical Chemistry* **2002**, *74*, 2813-2832.

(17) Ishida, A.; Yoshikawa, T.; Natsume, M.; Kamidate, T. *Journal of Chromatography A* **2006**, *1132*, 90-98.

(18) Ngola, S. M.; Fintschenko, Y.; Choi, W.-Y.; Shepodd, T. J. *Analytical Chemistry* **2001**, *73*, 849-856.

(19) Throckmorton, D. J.; Shepodd, T. J.; Singh, A. K. *Analytical Chemistry* **2002**, *74*, 784-789.

(20) Liu, J.; Chen, C.-F.; Tsao, C.-W.; Chang, C.-C.; Chu, C.-C.; DeVoe, D. L. *Analytical Chemistry* **2009**, *81*, 2545-2554.

(21) Desmet, G.; Baron, G. V. *Journal of Chromatography A* **1999**, *855*, 57.

(22) Desmet, G.; Baron, G. V. *Analytical Chemistry* **2000**, *72*, 2160-2165.

(23) Desmet, G.; Vervoort, N.; Clicq, D.; Baron, G. V. *Journal of Chromatography A* **2001**, *924*, 111.

(24) Vervoort, N.; Clicq, D.; Baron, G. V.; Desmet, G. *Journal of Chromatography A* **2003**, *987*, 39-48.

(25) Fekete, V.; Clicq, D.; Malsche, W. D.; Gardeniers, H.; Desmet, G. *Journal of Chromatography A* **2007**, *1149*, 2-11.

(26) Fekete, V.; Clicq, D.; Malsche, W. D.; Gardeniers, H.; Desmet, G. *Journal of Chromatography A* **2008**, *1189*, 2-9.

(27) Yin, H.; Killeen, K.; Brennen, R.; Sobek, D.; Werlich, M.; Goor, T. v. d. *Analytical Chemistry* **2005**, *77*, 527-533.

(28) Reichmuth, D. S.; Shepodd, T. J.; Kirby, B. J. *Analytical Chemistry* **2005**, *77*, 2997-3000.

(29) Lazar, I. M.; Trisiripisal, P.; Sarvaiya, H. A. *Analytical Chemistry* **2006**, *78*, 5513-5524.

(30) Yin, H.; Killeen, K. *Journal of Separation Science* **2007**, *30*, 1427-1434.

(31) Ramsey, R. S.; Ramsey, J. M. *Analytical Chemistry* **1997**, *69*, 1174-1178.

(32) Mellors, J. S.; Gorbounov, V.; Ramsey, R. S.; Ramsey, J. M. *Analytical Chemistry* **2008**, *80*, 6881–6887.